



# **PLUME CHARACTERIZATION OF BUSEK 600W HALL THRUSTER**

## **THESIS**

Duc Minh Bui, 2d Lieutenant, USAF

AFIT/GA/ENY/12-M05

**DEPARTMENT OF THE AIR FORCE  
AIR UNIVERSITY**

**AIR FORCE INSTITUTE OF TECHNOLOGY**

---

---

**Wright-Patterson Air Force Base, Ohio**

APPROVED FOR PUBLIC RELEASE; DISTRIBUTION UNLIMITED

AFIT/GA/ENY/12-M05

The views expressed in this thesis are those of the author and do not reflect the official policy or position of the United States Air Force, Department of Defense, or the United States Government. This material is declared a work of the U.S. Government and is not subject to copyright protection in the United States.

AFIT/GA/ENY/12-M05

**PLUME CHARACTERIZATION OF BUSEK 600W HALL THRUSTER**

**THESIS**

Presented to the Faculty

Department of Aeronautics and Astronautics

Graduate School of Engineering and Management

Air Force Institute of Technology

Air University

Air Education and Training Command

In Partial Fulfillment of the Requirements for the  
Degree of Master of Science in Aeronautical Engineering/Space Systems Engineering

Duc Minh Bui, BS

2d Lieutenant, USAF

March 2012

APPROVED FOR PUBLIC RELEASE; DISTRIBUTION UNLIMITED

AFIT/GA/ENY/12-M05

**PLUME CHARACTERIZATION OF BUSEK 600W HALL THRUSTER**

Duc Minh Bui, BS

2d Lieutenant, USAF

Approved:

\_\_\_\_\_  
Richard E. Huffman, LtCol, USAF (Chairman)

\_\_\_\_\_  
Date

\_\_\_\_\_  
Carl R. Hartsfield, LtCol, USAF (Member)

\_\_\_\_\_  
Date

\_\_\_\_\_  
Dr. William A. Hargus Jr. (Member)

\_\_\_\_\_  
Date

## **Abstract**

The BHT-600W thruster has a high potential to place on various commercial and military satellites as a main propulsion system for orbit maintenance and orbit maneuvering. Therefore, the thruster's performance characteristics and parameters were evaluated for various operating conditions. These parameters include thrust, power consumption, mass flow rate, and efficiencies. Various plume properties were measured and characterized for the thruster to include exhaust beam profile and ion species distribution. The faraday probe was used to examine the thruster plume current density while the ion species fractions were determined by the ExB probe. The inverted pendulum thrust stand was also utilized to determine the thrust performance of the thruster. This research determined optimal performance for this thruster was lower but closed to values stated by Busek Co. The measured values were  $34.8 \pm 1.3$  mN of thrust,  $1,267 \pm 39$  s specific impulse, and had a measured propulsive efficiency of  $36.2 \pm 2.4\%$ . Last, beam efficiency from Faraday probe measurements yielded  $52.1 \pm 0.27\%$ . Charge exchanges were observed to appear around  $40^\circ$  divergence angles. Higher charge ion species were found to dominate with increasing discharge voltage. Lastly, there were minimal effects of magnet currents on thruster's performance. The results from the research will hopefully be of use in future developments and will contribute to operational applications. This research could potentially be used to improve or confirm numerical models, help to develop future designs, and improve comparison of experimentation with on-orbit plume simulations.

## **Acknowledgments**

The author would also like to acknowledge the support of AFRL/RZS (Mr. Michael Huggins and Dr. William Hargus) for the support of this research. Any opinions, findings and conclusions or recommendations expressed in this paper are those of the authors and do not necessarily reflect the views of Air Force Research Laboratory.

## Table of Contents

	Page
Abstract .....	iv
Acknowledgments.....	v
Table of Contents .....	vi
List of Figures .....	ix
List of Tables .....	xiv
Nomenclature .....	xv
I. Introduction .....	1
I.1 Application .....	1
I.2 Motivation .....	2
I.3 History of Electric Propulsion .....	5
I.4 Problem Statement.....	6
I.5 Objectives .....	9
II. Literature Review .....	10
II.1 Overview .....	10
II.2 Mission Analysis .....	11
II.3 Hall Thruster Operation.....	15
II.4 Performance Parameters .....	20
II.5 Diagnostic Tools.....	25
A. <i>Inverted Pendulum</i> .....	26
B. <i>Faraday Probe</i> .....	29
C. <i>ExB Probe (Wein filter)</i> .....	31
III. Methodology .....	35

III.1	Vacuum Chamber .....	35
III.2	Support Equipment .....	39
	<i>A. Translation Stages</i> .....	39
	<i>B. Beam Profiler</i> .....	40
	<i>C. Propellant Feed</i> .....	42
	<i>D. Power Processing Unit and Control System</i> .....	43
III.3	Thruster .....	44
III.4	Diagnostic Equipment .....	45
	<i>A. Inverted Pendulum</i> .....	45
	<i>B. Faraday Probe</i> .....	50
	<i>C. ExB Probe</i> .....	53
III.5	Error Analysis .....	56
IV.	Results and Analysis .....	57
IV.2	Thruster Performance .....	57
	<i>A. Voltage-Current Curve</i> .....	58
	<i>B. Both Magnets Effects on V-I Curve</i> .....	63
IV.3	Thrust Measurement .....	71
	<i>A. BHT-200W</i> .....	71
	<i>B. BHT-600W's Performance</i> .....	72
	<i>C. Both Magnet Coils Effects on Thruster's Performance</i> .....	78
	<i>D. Inner Magnet Effects on Thruster's Performance</i> .....	82
	<i>E. Outer Magnet Effects on Thruster's Performance</i> .....	86



IV.4	Beam Current Density .....	90
	<i>A. Both Magnets Effects on Plume's Shape</i> .....	97
	<i>B. Inner Magnet Effects on Plume's Shape</i> .....	101
	<i>C. Outer Magnet Effects on Plume's Shape</i> .....	104
IV.5	Ion Species.....	108
	<i>A. Effect of Divergence Angles</i> .....	114
	<i>B. Magnet Effects on Exhaust Species</i> .....	117
	<i>C. Outer Magnets Effects on Exhaust Species</i> .....	120
	<i>D. Inner Magnets Effects on Exhaust Species</i> .....	123
V.	Conclusion and Recommendation .....	126
	<i>V.1 Challenges and Implications</i> .....	126
	<i>V.2 Thrust Stand Measurements</i> .....	127
	<i>V.3 Faraday Probe Measurements</i> .....	128
	<i>V.4 ExB Probe Measurements</i> .....	129
	Appendix A. Additional Diagnostic Tools .....	131
	Appendix B. Additional Faraday measurements .....	139
	Appendix C. Additional ExB measurements .....	148
	Bibliography .....	155

## List of Figures

	Page
Figure 1: Relationship of payload mass fraction and specific impulse .....	14
Figure 2: Payload mass fraction versus exhaust velocity. ....	14
Figure 3: Thrust durations for various electric thrusters.....	15
Figure 4: Cross-section schematic of a typical Hall Thruster. ....	16
Figure 5: Inverted pendulum free body diagram .....	27
Figure 6: Anode specific impulse for various discharge voltages for BHT-600W. ....	28
Figure 7: Schematic for Faraday probe. Adapted from Farnell [45, 52] .....	30
Figure 8: Typical current density distribution for the exhaust plume.....	31
Figure 9: Typical schematic for ExB probe. ....	32
Figure 10: Typical ExB probe sweep.....	33
Figure 11: SPASS lab layout. Taken from Harpe [36]. ....	36
Figure 12: Pressure gauges used to monitor vacuum chamber for all pumping stages. ...	38
Figure 13: VacuumPlus software interface used for monitoring chamber pressure. ....	38
Figure 14: Thruster mounted on a box frame, attached to the translation stage. ....	40
Figure 15: Beam profile system for mounting the Faraday and ExB probe. ....	41
Figure 16: Propellant feed system.....	42
Figure 17: BPU-600 host simulator software used to control the thruster. ....	43
Figure 18: BHTC-1500 mounted on BHT-600.....	45
Figure 19: Inverted pendulum set up. Taken from Temkin [46]. ....	46
Figure 20: Uncovered Busek T8 inverted pendulum. ....	47

Figure 21: LVDT readout controller for thrust stand.....	48
Figure 22: LabView interface for thrust measurement. ....	49
Figure 23: Faraday probe.....	50
Figure 24: LabView interface for Faraday and ExB measurements.....	51
Figure 25: Schematic for Faraday probe setup. ....	52
Figure 26: Uncovered ExB probe. ....	53
Figure 27: ExB probe electrical diagram. Taken from Farnell [45]. ....	54
Figure 28: Mounting of ExB probe for measurements. ....	55
Figure 29: V-I curve for BHT-600W.....	59
Figure 30: Ball plume shape from low discharge current mode. ....	60
Figure 31: Plume shape of the current limit mode.....	61
Figure 32: Jet plume shape found in voltage control mode. ....	61
Figure 33: Discharge current fluctuation from thruster's instability. ....	62
Figure 34: Outer or wider cone instability at higher discharge voltage.....	63
Figure 35: Discharge current effects from inner and outer magnet currents. ....	65
Figure 36: Discharge current responses to magnets connected in series or to independent power supplies.....	66
Figure 37: Inner magnet currents effect on discharge current. ....	69
Figure 38: Outer magnet currents effect on discharge current. ....	70
Figure 39: Thrust measured at various discharge power and mass flow rates.....	74
Figure 40: Isp at various discharge power and mass flow rates. ....	75
Figure 41: Propulsive efficiency at various discharge power and mass flow rates .....	76

Figure 42: Thermal drift effect on thrust measurement. ....	77
Figure 43: Operating points tested for magnet coils effects on thruster performance. ....	78
Figure 44: Magnets effect on thrust for various $V_d$ and mass flow rates. ....	80
Figure 45: Inner magnet effect on efficiency for various operating conditions. ....	81
Figure 46: Inner magnet effect on Thrust for various operating conditions. ....	83
Figure 47: Inner magnet effect on efficiency for various operating conditions. ....	85
Figure 48: Outer magnet effect on thrust for various operating conditions. ....	87
Figure 49: Outer magnet effect on efficiency for various operating conditions. ....	89
Figure 50: Faraday sweep for nominal condition. ....	91
Figure 51: Faraday sweep at 40cm radial distance. ....	92
Figure 52: Faraday probe position effect on peak current density. ....	93
Figure 53: Beam efficiency at 40cm radial distance. ....	95
Figure 54: Beam efficiency relationship to probe radial distance from the thruster. ....	96
Figure 55: Operating points tested for magnet coils effects on plume shape. ....	97
Figure 56: Magnets effects on peak current density. ....	98
Figure 57: Magnets effects on FWHM. ....	99
Figure 58: Magnets effects on beam efficiency. ....	100
Figure 59: Inner magnets effects on peak current density. ....	102
Figure 60: Inner magnets effects on FWHM. ....	102
Figure 61: Inner magnets effects on beam efficiency. ....	103
Figure 62: Outer magnets effects on peak current density. ....	105
Figure 63: Outer magnets effects on FWHM. ....	106

Figure 64: Outer magnets effects on beam efficiency. ....	107
Figure 65: ExB swept for nominal condition.....	109
Figure 66: ExB sweep for different discharge voltages.....	111
Figure 67: Xe species fractions for various operating conditions.....	112
Figure 68: : Xe species fractions for various divergence angles. ....	115
Figure 69: ExB trace for high divergence angles.....	117
Figure 70: Operating points tested for magnet coils effects on xenon species.....	118
Figure 71: Magnet current effects on xenon species production. ....	119
Figure 72: Operating points tested for outer magnet coils effects on xenon species.....	121
Figure 73: Outer magnets current effects on xenon species production. ....	122
Figure 74: Operating points tested for inner magnet coil effects on xenon species. ....	123
Figure 75: Operating points tested for inner magnet coils effects on xenon species.....	124
Figure 76: Typical single Langmuir Probe. ....	131
Figure 77: Langmuir probe theoretical result. ....	132
Figure 78: Typical RPA.....	135
Figure 79: Faraday sweep at 50cm radial distance. ....	139
Figure 80: Faraday sweep at 60cm radial distance. ....	140
Figure 81: Faraday sweep at 70cm radial distance. ....	140
Figure 82: Beam efficiency at 50cm radial distance.....	141
Figure 83: Beam efficiency at 60cm radial distance.....	142
Figure 84: Beam efficiency at 70cm radial distance.....	142
Figure 85: Magnets effects on peak current density. ....	143

Figure 86: Magnets effects on FWHM. ....	144
Figure 87: Magnets effects on peak current density. ....	144
Figure 88: Magnets effects on FWHM. ....	145
Figure 89: Inner magnets effects on peak current density. ....	146
Figure 90: Inner magnets effects on FWHM. ....	146
Figure 91: Inner magnets effects on peak current density. ....	147
Figure 92: Inner magnets effects on FWHM. ....	147
Figure 93: ExB swept for $V_d=100V$ , $I_d=2.28A$ , mass flow = 2.60mg/sec. ....	148
Figure 94: ExB swept for $V_d = 400V$ , $I_d = 1.598A$ , mass flow = 2.079mg/sec. ....	149
Figure 95: ExB swept for $V_d = 100V$ , $I_d = 1.58A$ , mass flow = 2.079mg/sec. ....	149
Figure 96: ExB swept for $V_d = 250V$ , $I_d = 2.47A$ , mass flow = 3.092mg/sec. ....	150
Figure 97: ExB swept for $V_d = 100V$ , $I_d = 3.0A$ , mass flow = 3.092mg/sec. ....	150
Figure 98: Xe species fractions for various operating conditions.....	151
Figure 99: Both magnets current effects on Xe fraction for mass flow = 2.6mg/s.....	152
Figure 100: Outer magnets current effects on Xe fraction for mass flow = 2.6mg/s. ....	153
Figure 101: Inner magnets current effects on Xe fraction for mass flow = 2.6mg/s. ....	154

## List of Tables

	Page
Table 1: Typical performance for space thrusters [34]. .....	10
Table 2: Typical performance for electric thrusters [34]. .....	11
Table 3: BHT-200W nominal performance parameters. ....	72
Table 4: BHT-600W nominal performance parameters. ....	73

## Nomenclature

$\theta(r)$  = average half – angle beam divergence

$\Omega_i$  = beam current fraction

$\zeta_i$  = ion species fraction

$\vec{B}$  = local magnetic field

$e^-$  = electron

$\vec{E}$  = electric field

$\vec{F}_m$  = force density

$g_0$  = Gravity at sea level ,  $9.81 \frac{m}{s^2}$

$I_b$  = total beam current

$I_{sp}$  = Specific Impulse

$\vec{j}$  = Hall current

$j_B$  = ion current density

$\dot{m}$  = propellant mass flow rate

$\dot{m}_i$  = ion mass flow rate

$m_i$  = initial mass

$m_f$  = final mass

$m_{payload}$  = payload mass

$m_{power\ plant}$  = power plant mass

$m_{propellant}$  = propellant mass

$m_{structure}$  = structure mass



$\eta_a$  = *anode efficiency*

$\eta_b$  = *beam current efficiency*

$\eta_c$  = *cathode efficiency*

$\eta_m$  = *mass efficiency*

$\eta_0$  = *electrical utilization efficiency*

$\eta_T$  = *efficiency for converting electric power to jet power*

$\eta_T$  = *overall efficiency*

$\eta_v$  = *beam voltage efficiency*

$P_e$  = *electrical power*

$P_{jet}$  = *jet power*

$q_i$  = *charge of ion*

$T$  = *Thrust*

$V_e$  = *effective exhaust velocity*

$\Delta V_{probe}$  = *ExB probe applied voltages*

$\vec{v}$  = *particle velocity*

$X_e$  = *Xenon atom*

# **PLUME CHARACTERIZATION OF BUSEK 600W HALL THRUSTER**

## **I. Introduction**

The focus of this research is to characterize a Busek 600 Watt Hall thruster (BHT-600). The impacts of different input power and propellant mass flow rates effect on its performance and exhaust plume properties were investigated. This experiment quantified thruster performance parameters such as thrust, specific impulse (Isp), and overall efficiency. Additionally, plume properties, including the beam current density, divergence angle profile, and ion species were examined. These results can potentially be used in aiding the development and modeling of new space systems.

### **I.1 Application**

Electric propulsion is a technology that has not been investigated as much compared to conventional cold gas or chemical engines [42]. It was not until the 1960s that there was a significant investment in research and development for space propulsion technology, which included Hall thrusters [15]. Electric propulsion is becoming more popular because it is cheaper to produce and is more reliable than conventional forms of propulsion, as demonstrated by Hall thruster for Earth orbits [15, 16]. Researchers have shown that Hall thrusters can outperform conventional chemical thrusters in many areas, such as station keeping and on-orbit maneuvers [15, 16]. This technology has attracted the interest of commercial, military, and science communities as a means for cheaper, lighter, and more efficient propulsion. There have been more than 238 Hall thrusters

operating on 48 different spacecraft since the 1960s [31]. Designers and planners continue to look to this technology for use in future spacecraft [42, 43].

Typically, Hall thrusters provide thrust in space and are used for orbit maintenance, maneuvering, and even minor orbit insertion. To keep a spacecraft in a desired orbit, operators must correct for losses and drifts periodically. A satellite's mission life ranges from 1 to 20 years or even more in some cases, and orbit maintenance for the satellite usually requires a small thrust increment with high accuracy. Therefore, fuel efficiency during orbit maintenance is a major design consideration for many propulsion system designers. Electric propulsion system such as Hall thrusters can meet the demands of these designers and can even outperform conventional chemical thrusters.

## **I.2 Motivation**

Studies have shown that electrical propulsion systems such as a Hall thruster provide substantial cost saving in payload [44]. Payload weight is an expensive commodity in space. The reduced weights of a Hall thruster allows for a smaller launch vehicle than a chemical thruster performing the same mission. This is possible because a Hall thruster has a higher specific impulse ( $I_{sp}$ ) than chemical thrusters. Hall thrusters also outperform Ion thrusters in certain missions. Hofer states , "...studies of low earth orbit constellation missions by Oleson have shown that the use of 1600s Hall thrusters or 2500s Ion thrusters for beginning-of-life orbit transfer and end-of-life de-orbit decreased the required number of launch vehicles from fourteen for an all-chemical spacecraft to eleven (p.20)." Additionally, Hofer claims that for geosynchronous earth orbit communication satellite missions can provide up to a 13% increase in payload for station

keeping, and from 20% to 45% for orbit transfers [15]. Therefore it is critical to determine the BHT-600W Hall thruster's Isp to analyze mass savings.

Hall thrusters have high Isps that range from 1,000–2,000s, and low thrusts of around 0.01–100mN. High Isp is desirable because it reduces the system mass. However, a Hall thruster's low thrust leads to a low thrust-to-weight ratio. This limits the Hall thruster's use to missions such as orbit maintenance and maneuvering. It is important to characterize BHT-600W's exact thrust profile because it determines the thruster's operating limits and conditions. Higher thrust would enable Hall thrusters to perform other missions, such as orbit raising, that are usually reserved for chemical engines in a practical timeframe. Empirically, a Hall thruster is able to produce higher thrust levels if its size and power are increased.

Like any other electric propulsion system, a Hall thruster requires a large and complex power system that is capable of producing high power levels to operate, and this usually leads to extra mass. The thrust from a Hall thruster is a function of input power and propellant mass flow rate. Power generated on a spacecraft is usually limited to an external source, the sun, or is recovered from onboard storage in battery systems. Depending on the mission, the propulsion system's power consumption usually has lower priority than the spacecraft's mission payload. As stated in *Space Mission Analysis and Design* [34], a typical propulsion and attitude control component consumes about 1%–10% of the total operating power. A low power margin means that the thruster cannot operate at nominal condition or that the mission payload must power down for maneuvers. Therefore, it is important to analyze the thruster's performance profiles for

various input powers below and above the nominal condition. Propellant mass flow rate is also critical to consider because it influences the spacecraft's design. Since Hall thrusters have a higher payload mass fraction than chemical thrusters, this enables the spacecraft to reduce mass and/or carry more payload or propellant. More propellant would increase the thruster's maneuver capability as well as its mission lifetime. Therefore, it is critical to determine the operating envelope for BHT-600W because this could mean that the Hall thruster would be used in a lower power operating mode.

In addition to power and propellant consumption, one has to consider the effect of thruster exhaust on the spacecraft itself. The exhaust plume from a Hall thruster contains high-velocity ions that are neutralized by flow from a cathode. These particles can adversely impact the spacecraft if they found their way back to the source. Ions can change the overall charge state of the spacecraft, short circuit electronics, erode protective coatings, impinge on sensors, increase thermal loads, cause deformation, and cause other damage. Previous studies have shown that the contaminant materials found in the exhaust plume are usually generated from thruster instabilities such as sputtering and anode degradation [5, 13, 14]. A spacecraft can encounter the exhausted material during each orbit period. To address these potential problems, the characteristics of the exhaust plume need to be examined so new solutions can be developed and incorporated into new models and designs.

Propulsion system designers are attracted to Hall thrusters because of their high specific impulse, but this electric propulsion system has not been as extensively studied as chemical thrusters. However, Hall thrusters can be beneficial in many ways, and there

is a need to explore and develop enhancements for this technology. This study will focus on quantifying thrust, specific impulse, efficiencies, and plume characteristics to gain more insights into the BHT-600 W Hall thruster.

### **I.3 History of Electric Propulsion**

A Hall thruster is a type of electrical propulsion system. Choueiri claims that electrical propulsion, along with modern rocketry, was envisioned as early as the 1900s by Konstantin Tsiolkovsky [40]. In the same decade, Robert Goddard informally expressed the concept of electric propulsion in his study and attempted to analyze it but failed. In 1920, Yuri Kondratyuk looked into the concept and envisioned propulsion through electrical discharge with fine propellant particles. This led to the development of a new system called the colloid thruster later on. In 1929, electric propulsion received recognition from Hermann Oberth, who many consider the father of rocketry. He dedicated a whole chapter to the technology in his work, discussing its potential for space flight.

For about two decades after, electric propulsion emerged slowly through various academic discussions and papers. There was no significant development but only concepts. Research in electric propulsion technology came to a standstill because it required a massive power source and a large vacuum facility. There was not any technology at the time to produce enough power to operate these devices in space. Due to such results, along with low thrust production, electric propulsion received little interest from industry and government when compared to chemical thrusters. The only major

contribution was from Valentin Glushko when he developed a prototype of the first electrothermal thruster [40].

Electric propulsion development was revitalized in the late 1950s. New technologies enabled the government and independent companies to develop small scale models for laboratory experiments. Various technologies were looked at, such as arc jets, ion beam, and electrostatic designs [40]. Development accelerated further in the '60s when the government and industry started to incorporate electric propulsion into their space vehicles. Several models were developed for space qualification as a result. This was due mainly to advances in power systems, equipment, and testing facility. The first successful space test occurred in 1964 and others followed suit later on [40]. Slowly, electric propulsion made its way into space, mainly supporting missions requiring low thrust such as orbit maintenance.

#### **I.4 Problem Statement**

The Busek's 600 Watt Hall thruster is ideally suited for a small to medium size satellite that has power greater than 1kW and does not need high thrust. This thruster was advertised to produce 42 mN of thrust and 1650s specific impulse, using propellant mass flow rate of 2.6 mg/s, yielding a propulsive efficiency of 55.0%. It has a discharge input power of 600 W, a discharge voltage of 300 V, and a discharge current of 2.05 A. It is optimized for operating "over a range of 300–600 W and produces 15–45 mN of thrust with a specific impulse of 1100–1700 sec" [33]. This specification only describes the thruster's overall performance and nothing more. Initial analysis on the BHT-HD-600 Hall thruster by AFRL showed that the thruster performance was actually lower at

nominal condition than advertised [2]. Therefore, evaluation of the thruster is needed to fully characterize its performance and operating envelope.

An initial problem for this research is a lack of extensive study for BHT-600W Hall thruster. However, the thruster has been used in many previous experiments by universities and institutions, notably the Air Force Research Laboratory (AFRL) [1-5, 8, 10]. The AFRL performed near-field and far-field measurements of the BHT-600W at few operating conditions around the nominal point [2]. This experiment found several factors that were unaccounted for. Therefore, further study and experiments are needed. These results are helpful to this research as references for independent comparison. Even with some work already done on this thruster, more experimentation is needed to analyze the thruster's full performance over a wider operating envelope.

Another issue was to determine the operating envelope to test the BHT-600W Hall thruster over. Each spacecraft mission has different operating limits due to constraints, including propellant, power, and operating time. There are certain ranges where the thruster becomes inoperative due to mission constraints or thruster instabilities. This is important because the operator may be interested in its throttling capability. Experiments on all those conditions to determine the operating envelope would be infeasible and a waste of resources. Therefore, a design of experiments was developed to determine which parameters should be focused on for this study. It was decided that would be best to provide data for nominal condition, high and low operating boundaries, and any conditions that were found to deviate from the norm.



Another problem, not considered in this research, is thermal analysis. A major contribution to failure on many spacecraft is heating. The standard way to remove heat is to radiate it into space through black body radiation. In addition to other spacecraft components, a propulsion system produces some amount of heat also. Heating from the propulsion system not only affects the spacecraft, it also affects the performance of the thruster itself. Previous research has shown that changing parameters such as mass flow would proportionally change the thruster's temperature, leading to changes in thruster performance and lifetime [5, 13, 14]. Temperature fluctuation can cause material properties to change, such as resistance, conductivity, and magnetic properties, that can change the magnetic field strength and ultimately change the thruster's performance [14, 36]. In addition, erosion and contaminants produced by high temperature can cause instabilities and adversely affect performance [14].

Another issue this research neglected is the operating time of the thruster. Spacecraft usually operate for a long period of time, ranging from one to twenty years. The onboard propulsion system will operate through a variety of conditions and will suffer degraded performance in many ways, such as erosion that leading to decreased efficiency [36]. Designers usually examine the conditions associated with the beginning of life and end of life as their parameters. Due to time constraints, this study only examines the thruster performance for a few short days and we recommend that further study for longer experiment duration be accomplished when time permits.

## **I.5 Objectives**

The purpose of this research is to determine fundamental parameters of an electric thruster: thrust, specific impulse, power consumption, overall efficiency, and plume profile. Thrust produced was measured by an inverted pendulum while the plume properties were determined by a Faraday probe and ExB probe. The objectives of this research are as follows:

- a) Use BHT 200W as a baseline. Additionally, compare to previous work done on BHT 600W by AFRL and other research institutions
- b) Develop performance curves at different operating conditions: thrust, voltage-current, current density, divergence angle, and ion species
- c) Determine efficiencies of the thruster
- d) Find out the thruster performance envelope and condition. Additionally, examine its throttling capability.

The results from the research will hopefully be of use in future developments and contribute to operational applications. This research could potentially be used to improve or confirm numerical models, help to develop future designs, and improve comparison of experimentation with on-orbit plume simulations.

## II. Literature Review

### II.1 Overview

The Hall Thruster is a type of electric propulsion technology, which utilizes electricity to increase the propellant exhaust velocity [31]. Its operation is based on the principles of both electric and magnetic fields. The interaction between electric and magnetic fields on the electrons produce Hall current effects within the ionization chamber, hence the name Hall Thruster. This propulsion technology focuses on producing thrust with extremely high exhaust velocity and low mass flow. A Hall thruster has low thrust to weight ratio but high in specific impulse (Isp) when compared with conventional chemical thrusters, which leads to an increase in payload mass fraction. Table 1 compares the performance characteristics of different types of space thrusters. Typically, thrusters producing a high thrust to weight ratio have short thrust duration and lower Isp. Similarly, Table 2 compares different types of electric thrusters. These thrusters produce low thrust but compensate with higher Isp.

Table 1: Typical performance for space thrusters [34].

Type	Isp(s)	Thrust/Weight	Thrust Duration
Chemical	100-600	1-100	Minutes
Nuclear (thermal)	500-1500	0.1-10	Hours
Electrothermal	100-1500	$10^{-1}$ - $10^{-3}$	Months- Years
Electromagnetic	1000-15,000	$10^{-2}$ - $10^{-6}$	Months- Years
Electrostatic	1500-100,000+	$< 10^{-4}$	Months- Years

Table 2: Typical performance for electric thrusters [34].

Type	Isp (s)	Thrust (mN)
Resistojet	200-300	100-500
Colloid	< 1,000	.001-1
ArcJet	500-1,000	500-1,000
Pulse Plasma	500-2,000	.01-10
Hall	1,000-2,500	0.01-2,500
Ion Engine	2,500-10,000	.01-100

## II.2 Mission Analysis

Hall thruster's performance can be affected by many parameters such as thrust, specific impulse, power, efficiency, and propellant mass. The formulation starts with the most important parameter, thrust. As with all rockets, thrust is calculated from the following

$$T = \dot{m}U_e \quad (1)$$

where  $T = Thrust$

$\dot{m} = propellant\ mass\ flow\ rate$

$U_e = effective\ exhaust\ velocity$

The effective exhaust velocity includes all unbalanced pressure forces between exit pressure and ambient pressure. It also includes any non-uniform velocity distribution across the exit cross sectional area [15]. Specific impulse, Isp, is determined from the following relationship

$$Isp = \frac{U_e}{g_0} = \frac{T}{\dot{m}g_0}, (sec) \quad (2)$$

where  $g_0$  is the gravity constant at sea level, 9.807 m/s. As shown in Equation 1, thrust can be increased by either raising the effective velocity or mass flow rate. Electric thrusters focus on producing thrust by increased velocity with minimal mass flow.

Propellant mass is one of the most important attributes to a spacecraft's operating lifetime because it relates directly to the mission  $\Delta V$  and spacecraft initial and final masses. This relationship is given by the ideal rocket equation originally derived by Tsiolkovsky[32], given by Equation 3 [31]:

$$\Delta V = Isp \ g_0 \ln \frac{m_i}{m_f} = U_e \ln \frac{m_i}{m_f} \quad (3)$$

where  $m_i$  and  $m_f$  are the spacecraft initial and final mass. For electric propulsion, the final mass is defined as

$$m_f = m_{payload} + m_{structure} + m_{power\ plant} \quad (4)$$

Since an external power source is needed to operate, electrical power input  $P_e$  and specific power  $\alpha$  are included in the analysis.

$$\alpha = \frac{P_e}{m_{power}} \quad (5)$$

$$P_e = \alpha * m_{power} \quad (6)$$

$$m_{power} = \frac{1}{\alpha} \frac{T U_e}{\eta_T} \quad (7)$$

where  $\eta_T = \text{efficiency for converting electric power to jet power}$

One drawback of electrical propulsion is called the payload penalty, which is the mass and space needed for an external power source. For a case assuming constant thrust and exhaust velocity, the burn time, or thrusting time, is given by the following [32]

$$\tau = \frac{m_{propellant}}{\dot{m}} = \Delta V \frac{m_i}{T} \quad (8)$$

With Equation 3-8, it can be shown that the payload mass fraction can be calculated from the following [32]

$$\frac{m_{payload}}{m_i} = e^{\frac{-\Delta V^*}{V_e^*}} - \frac{1}{2} \left( 1 - e^{\frac{-\Delta V^*}{V_e^*}} \right) V_e^{*2} \quad (9)$$

with

$$V_0 = \sqrt{\alpha \tau \eta_T} \quad (10)$$

$$\Delta V^* = \frac{\Delta V}{V_0} \quad (11)$$

$$V_e^* = \frac{U_e}{U_0} \quad (12)$$

Hall thrusters are attractive due to high specific impulse (Isp). Higher Isp is advantageous because it allows for higher payload mass fractions over conventional chemical rockets. This enables the spacecraft to reduce weight, requiring a smaller launch vehicle, carry more payload or propellant, or add more capability to the overall system. One of the objectives for all electric propulsion design is to maximize payload ratio. Equation 9 shows that for a given  $\Delta V$  requirement, one must need to maximize exhaust velocity and efficiency. The effects of this equation were plotted in Figure 1 for various thruster types. Figure 1 illustrates the relationship between payload mass fraction and Isp. Increasing the Isp would generally produce a higher payload mass fraction. However, there is an Isp that is associated with a maximum payload fraction. This relationship is illustrated in Figure 2. The plot shows that the peak payload mass fraction depends on the  $\Delta V$  and Isp. It is desirable to obtain the highest payload mass fraction, but technology limitations prevent some thrusters from reaching such theoretical points. The limitations include chemical reaction and material properties that would only allow some thrusters to operate within certain ranges of Isp.

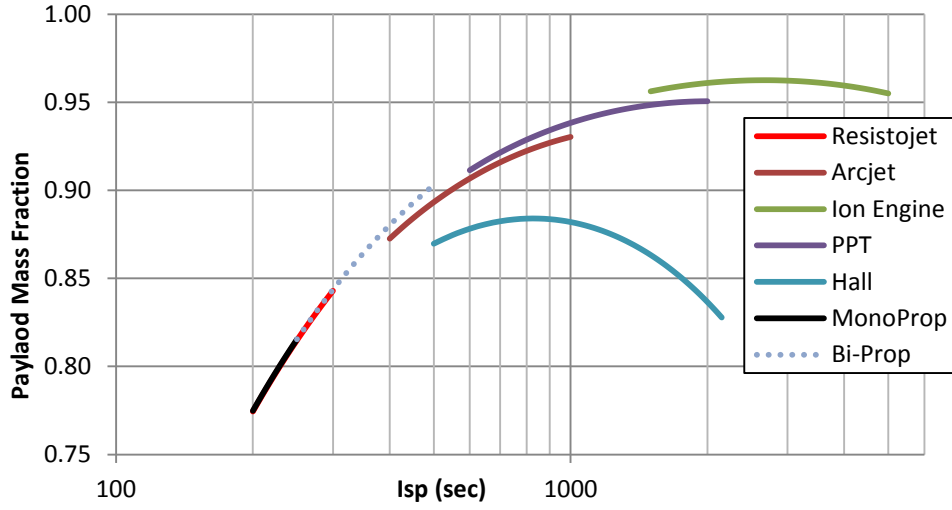


Figure 1: Relationship of payload mass fraction and specific impulse

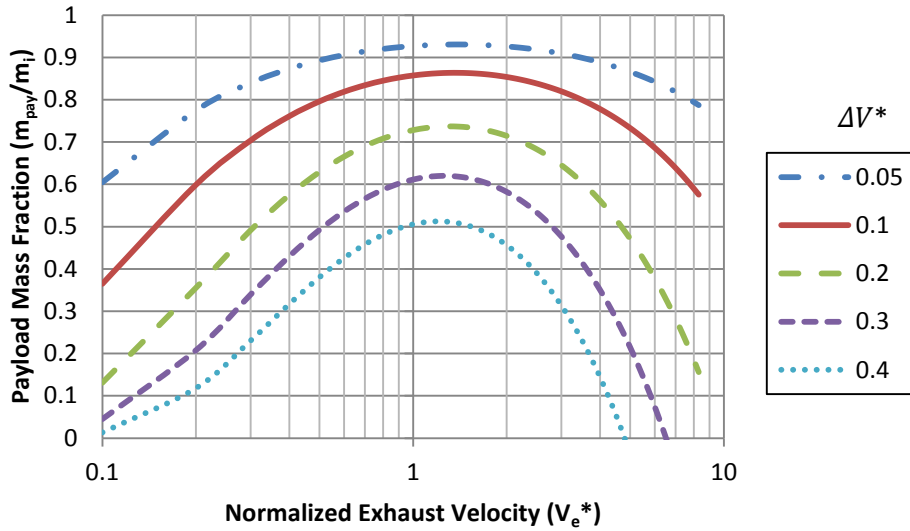


Figure 2: Payload mass fraction versus exhaust velocity.

The disadvantage of a Hall thruster is that it has low thrust. The burn time or thrust duration can be much longer than those of chemical rockets, as given by Equation 8. The thrust duration for different thrusters is plotted in Figure 3. The plot shows that chemical thrusters can produce a required  $\Delta V$  within seconds or minutes, but it would take

a Hall thruster weeks or even years to perform an equivalent task. For example, it is not practical for a Hall thruster to continuously thrusting for 110,000 days to reach  $\Delta V = 50$  m/s. Therefore, Hall thrusters are usually selected for missions that require low delta V, such as station keeping or orbit maintenance.

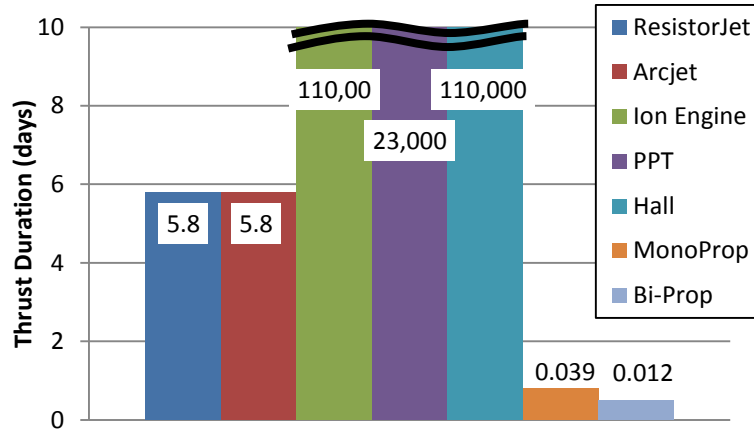


Figure 3: Thrust durations for various electric thrusters.

### II.3 Hall Thruster Operation

Electric propulsion thrusters are usually categorized into three classifications: electrostatic, electromagnetic, electrothermal. These classifications are associated with how the working fluid is accelerated out of the exhaust channel [16]. Electrothermal works like a conventional chemical rocket. It relies on gas thermodynamics to produce the required exhaust velocity, not electric or magnetic fields. The difference is that it uses electricity to heat up the working fluid. Electromagnetic systems depend on the magnetic and electric fields in principle. It uses the interaction of electromagnetic fields with the plasma to accelerate the working fluid to the required exhaust velocity.



Similarly, an electrostatic system uses the electric field to accelerate the plasma to produce thrust.

Hall Thrusters use both electrostatic and electromagnetic principles to operate. However, not all authors agree on how to classify Hall thrusters either as electrostatic or electromagnetic system [16, 32, 34]. The thruster uses the electromagnetic force to accelerate the electrons which then ionize the propellant. The buildup of electrons produces an electrostatic force within the discharge chamber. This electrostatic force accelerates the ions out and produces thrust. Hall devices usually consist of the anode, cathode, plasma channel, and magnetic coils. The schematic and geometry of a generic Hall thruster can be seen from Figure 4. It shows the crossed electric and magnetic field, that produce the Hall effects.

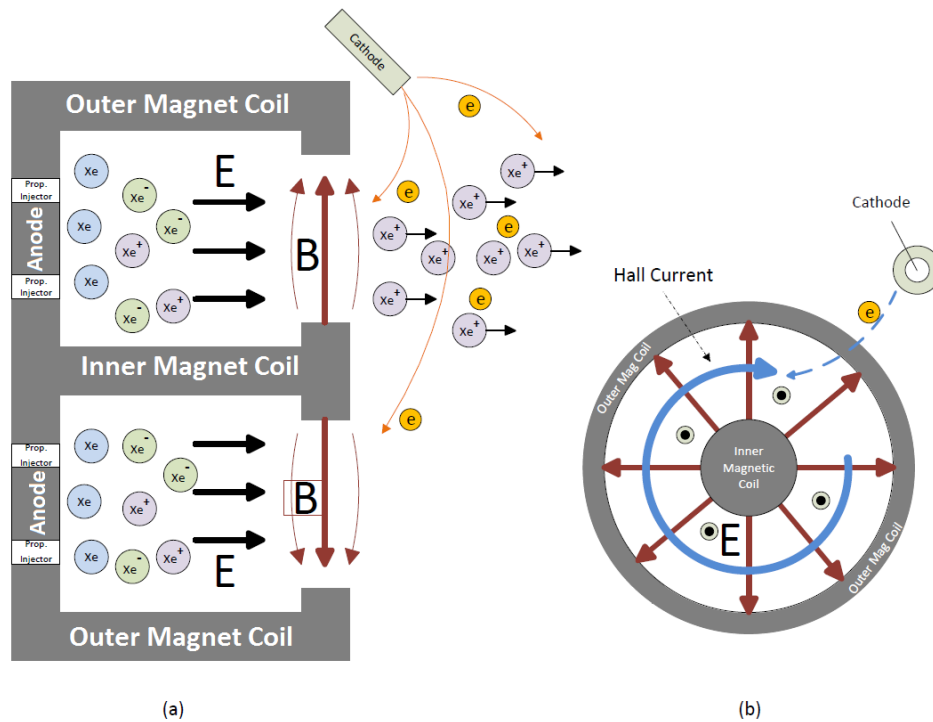


Figure 4: Cross-section schematic of a typical Hall Thruster.

The anode acts as the positive electrode and is located at the base of the discharge channel, where majority of the neutral propellant is injected. The rest of the propellant is injected through the cathode, which acts as the negative electrode and is located just downstream and outside of the plume. It produces electrons to initiate the ionization process and in addition, neutralizes the positive ions in the exhaust. This prevents charge build up on the spacecraft, and prevents the ions from accelerating back to the spacecraft, which would produce zero net force. The discharge channel wall is typically covered in Boron Nitride (BN) or Borosil (BN-SiO<sub>2</sub>) to protect the thruster from ionic and electronic bombardment [15]. These materials are chosen because they produce low erosion rates, secondary electron emission, and reduce sputtering. The magnetic circuits' placement and shape are strategically chosen because they greatly influence the performance, efficiency, and life of the thruster [31]. The circuits are configured in a way to produce a magnetic and electric field that will interact with the electrons to produce Hall current and consequently ionize the neutral propellant. It also serves as support structure for other thruster components [15].

Almost anything that can be ionized has the potential for use as a propellant in a Hall thruster. However, many have technical challenges to overcome and only few are feasible from an operational standpoint. The most proven and widely used propellant is Xenon. Previous research examined other potential propellants as well, such as Krypton, Iodine, Mercury, Bismuth, and reactive liquid metals [2, 35]. Xenon is popular because it is a noble gas that has relatively low ionization energy, is storable, and has high

molecular weight. High molecular weight usually means high exhaust velocity and ultimately high thrust [35].

Hall thruster operation starts with the cathode emitting electrons. Due to electrostatic forces, these electrons will start to migrate toward the positively charged anode through an axial electric field along the channel length. However, the radial magnetic field  $\vec{B}$  will change the electron's direction and velocity once it enters the thruster chamber. Instead, the electrons will start gyrating or spiraling around the discharge channel in an azimuthal motion [32]. This motion is described by Equation 13 and also illustrated in Figure 4b.

$$\vec{U}_e = \frac{\vec{E} \times \vec{B}}{B^2} \quad (13)$$

The phenomenon where an electron changes its motion due to an interaction between magnetic and electric fields is called the Hall Effect. This motion of electrons would induce a current called a Hall current, hence the name Hall thruster. A force produced by the Hall current interacts with the radial magnetic field given by equation below [32].

$$\vec{F}_m = \vec{j} \times \vec{B} \quad (14)$$

where  $\vec{F}_m$  is the force density that is perpendicular to the local Hall current density  $\vec{j}$  and local magnetic field  $\vec{B}$ . This force produced by electrons is relatively small compare to the ions due their low mass. Unlike electrons, positive ions are too heavy and slow to be perturbed by the magnetic field to a noticeable degree. However, such perturbation can influence the thruster design as well. The depth of discharge channel is usually sized by

ion's gyration radius so the magnetic field effect on it can be neglected [36]. This ensures that the ion accelerated out of discharge channel is not greatly diverged.

The electrostatic force still acts on the electron, causing drift toward the anode, where it collides with the propellant. The collisions between the electrons and neutral propellants produce plasma. This process is called ionization. Equation 15 illustrates this process for Xenon [14]. The ionization process can also produce higher charge ions if there is enough energy.



As the electrons drift toward the anode, the azimuthal motion severely restricts their axial motion. This increases electron residence time in the chamber and lead to increased potential collision with the neutral propellants upstream within the chamber. These collisions generate plasma in the discharge chamber, where the negative electrons are absorbed by the anode to complete the circuit. As for the positive ions, they are accelerated through the electric field to produce thrust. Thrust production is described by Lorentz Force [36].

$$\vec{F}_i = q_i (\vec{E} + \vec{v} \times \vec{B}) \quad (16)$$

where  $q_i$  = the charge of moving particle (ion for this case)

$\vec{E}$  = applied electric field

$\vec{v}$  = particle velocity

$\vec{B}$  = magnetic field strength

A Hall thruster produces most of its thrust from the electric field component, called the electrostatic force. The force produced by the ions interacting with the magnetic field is

relatively small compared to the total thrust being produced; therefore, it can be neglected. It is small because the ion mass is too large to be greatly affected by the magnetic field. The ion velocity exiting the thruster is usually around 15km/s or higher [22]. Described by Equation 1, the ion thrust is the product of its ion mass flow and velocity. As the ion plume exits the thruster, it is immediately neutralized by electron production from the cathode. This is required to make the plume neutral again, preventing charge buildup and reduced net thrust on the spacecraft.

#### **II.4 Performance Parameters**

As previously discussed, performance parameters such as thrust and efficiencies are important and are used to define system performance. The primary parameters of interest are thrust, specific impulse, power, and total efficiency. Thrust is the most important parameter for an engine because it is the force that propels a system toward a desire direction and affects the spacecraft's orbit. It is given by Equation 17 and can be directly measured using an inverted pendulum [31].

$$T = \dot{m}U_e \quad (17)$$

Equation 17 also determines the effective exhaust velocity of the thruster. The effective exhaust velocity of the thruster can be obtained by measuring thrust and mass flow rate. This velocity includes all unbalanced pressure forces between exit pressure and ambient pressure. It also includes any non-uniform velocity distribution across the exit cross sectional area [15]. However, thrusters are usually characterized by specific impulse ( $I_{sp}$ ).  $I_{sp}$  is the ratio of thrust being produced to propellant weight flow rate. This is an

important parameter for a thruster because it remains independent from the input mass flow and the thrust produced.

$$Isp = \frac{U_e}{g_0} = \frac{T}{\dot{m}g_0} \quad (18)$$

The thruster's overall efficiency is the ratio of power produced by the thruster to its input power. The power produced by the thruster is called a jet power,  $P_{jet}$ . Jet power can be calculated from measured thrust and propellant mass flow rate as given by Equation 19. This analysis only considers kinetic thrust power of the beam because it is the only force that would give motion to the thruster. Other sources, such as heat and pressure, are considered losses and will drive the efficiency of the system.

$$P_{jet} = \frac{T^2}{2\dot{m}_p} \quad (19)$$

The thruster efficiency can be determined from Equation 20. Electrical powers,  $P_{elec}$ , are known inputs. They are the total power that a thruster draws from a source to operate. This can be determined from the power supply of each thruster component. The total electrical power is a sum of all those components. For Hall thruster, total power input is given by Equation 21.

$$\eta_T = \frac{P_{jet}}{P_{elec}} = \frac{T^2}{2\dot{m}_p P_{elec}} \quad (20)$$

$$P_{elec} = P_d + P_k + P_{mag} \quad (21)$$

where  $P_d = \text{discharge power}$

$P_k = \text{cathode keeper power}$

$P_{mag} = \text{power to generate magnetic field}$

Equations 17–21 show that the total efficiency can be determined from thrust, mass flow rate, and input power alone. However, they do not tell us much about the voltages, mass flow, and current interaction within the thruster and its plume exhaust. Other parameters such as beam current, discharge voltage, and mass flow are needed to characterize the thruster. The total efficiency could also be expressed by combining different component efficiencies: beam current, voltage, mass, and electrical utilization efficiency. Another method for determining the total efficiency is given by Equation 22 [31]. This equation also include a  $\gamma^2$  term which corrects for the beam divergence and presence of multiply-charged ion species.

$$\eta_T = \gamma^2 \eta_b \eta_v \eta_m \eta_0 \quad (22)$$

$$\eta_b = \frac{I_b}{I_d} \quad (23)$$

$$\eta_v = \frac{V_b}{V_d} \quad (24)$$

$$\eta_m = \frac{\dot{m}_i}{\dot{m}_a + \dot{m}_c} \quad (25)$$

$$\dot{m}_i = \frac{M}{q} I_d \eta_b \quad (26)$$

$$\eta_0 = \frac{P_d}{P_{elec}} = \frac{P_d}{P_d + P_k + P_{mag}} \quad (27)$$

where  $\eta_b = \text{beam current efficiency}$   
 $\eta_v = \text{beam voltage efficiency}$   
 $\eta_m = \text{mass efficiency}$   
 $\dot{m}_i = \text{ion mass flow rate}$   
 $\eta_0 = \text{electrical utilization efficiency}$

Furthermore, the anode efficiency of the thruster can be expressed as

$$\eta_a = \frac{T^2}{2\dot{m}_a P_d} = \frac{\eta_T}{\eta_0 \eta_c} \quad (28)$$

Where  $\eta_c$  defined as “cathode efficiency”

$$\eta_c = \frac{\dot{m}_a}{\dot{m}_p} = \frac{\dot{m}_a}{\dot{m}_a + \dot{m}_c} \quad (29)$$

This efficiency is important because it separates the cathode and magnetic losses contribution so that one can look only at the plasma production and acceleration interaction [31].

The discharge beam current efficiency  $\eta_b$  is given by the beam current and discharge current. The beam current is generated mainly from the ion flow exiting the thruster. This quantity can be measured by an electrostatic probe such as the Faraday probe. Similarly, the discharge voltage efficiency  $\eta_v$  is a ratio of beam voltage to discharge voltage. It can also be determined from an electrostatic probe such as the retarding potential analyzer (RPA) or Langmuir Probe. The other efficiencies are the mass and electrical utilization. Total mass efficiency  $\eta_m$  is expressed as the ratio of ion mass flow out from the plume to total mass flow into the thruster, where  $\dot{m}_a$  and  $\dot{m}_c$  are the mass flow coming into the anode and cathode, respectively. The ion mass flow rate leaving the anode is given by Equation 26. For a Xenon propellant,

$$\frac{M}{q} = 1.36125 \times 10^{-6}$$

The mass flow rates into the anode and cathodes are determined and set by the user. They are known values because they are controlled by a regulator. The last component is electrical utilization efficiency  $\eta_0$ ; this is the ratio of discharge power and input electrical



power into the thruster. Discharge power is the power the anodes use to operate the thruster. Each power components are determined by the power supply and could be measured by an amp or voltage meter.

The overall efficiency needs to include a correction factor due to multiply charged ion and beam divergence. These factors are produced by non-uniformity in the plasma source, ion current density profile, electric fields, curved ion acceleration from interaction with magnetic field, and ionization inefficiency [31]. In the earlier analysis, these effects were assumed to be small and were neglected for simplification. This correction is given by ( $\gamma$ ). This factor allows for a more accurate description of the thruster performance. It is simply the product of the divergence  $F_t$  and multiply charged species factor ( $\alpha$ ) and is given by Equation 14 [35].

$$\gamma = \alpha F_t \quad (30)$$

$$F_t = \frac{\int_0^r 2\pi r J(r) \cos \theta(r) dr}{I_b} \quad (31)$$

where

$\theta(r)$  = average half – angle beam divergence, a function of the radius

$J(r)$  = ion current density, a function of the radius

$r$  = beam radius

The multiply-charged species ( $\alpha$ ) correction is applied due to propellant being ionized to a higher charged state. Assuming that the beam contains only singly and doubly charged ions, then the correction factor is given by [31]

$$\alpha = \frac{I^+ + \frac{1}{\sqrt{2}} I^{++}}{I^+ + I^{++}} \quad (32)$$

where  $I^+$  and  $I^{++}$  are the singly and doubly charged ion number densities, respectively. The multiply charged species fractions are determined from ExB probe measurement, which provides a current corresponding to each ion species.

The total efficiency for Hall thruster can be expressed in two forms: the ratio of jet power and electrical input power, and the product of different component efficiencies. These are important because they provide an insight into the thruster performance as a function of various parameters and how they affect the overall thruster operation. Data from this experiment will more fully characterize the performance of BHT-600W. These data can be used to model or confirm predictions for Hall thruster or similar thrusters. Additionally, this could potentially be used for future space mission analysis and design. Obtaining such data requires some direct measurement and some calculation. This experiment will employ various methods and probes to obtain such parameters for this analysis.

## **II.5 Diagnostic Tools**

Electric propulsion test and evaluation techniques are quite sophisticated due to the complexity of the system and interaction between the various parameters that affect performance. The main issue is to simulate the space environment inside of the atmosphere for testing and evaluation. For example, thermal flux can change the material and affect the system performance. Environment ions and electronics may produce artificial neutralization that could produce inaccurate reading. Facility or wall surfaces may produce contamination as well. There are an abundance of factors that have the potential to adversely affect the experiment and have to be considered in more detail. It

is a challenge to address how these interactions can adversely affect the system and potentially skew the results. Various tools and techniques were developed to analyze the plume of an electric propulsion system. Some of the most popular methods are the thrust stand, Faraday probe, Langmuir probe, infrared imager, microwave interferometer, high speed imaging, retarding potential analyzer, ExB probe, laser, mass spectrometer, and emission spectroscopy. These techniques have been used to quantify plume properties such as plasma density, particulate temperature, plume potential, magnetic and electric field, current density, energy distribution, and species fractions.

#### *A. Inverted Pendulum*

The inverted pendulum is an unstable system. A small perturbation such as a small thrust from a Hall thruster would greatly affect the system responses. This unstable configuration causes the inverted pendulum to have a high sensitivity or high precision in the measurement. However, unstable systems are prone to produce high error sources. An inverted pendulum is highly sensitive to external forces such as vibration, thermal drift, tare forces, and thermal deflections [25, 30].

Figure 5 illustrates the schematic and various forces acting on the thruster. The free body diagram shows the system consists of three main components: the platform, pendulum arm, and flexure point. The platform is for support. The pendulum arm supports the thruster and provides length to create moments. The flexure point is needed to produce a restoring moment where thrust can be determined.

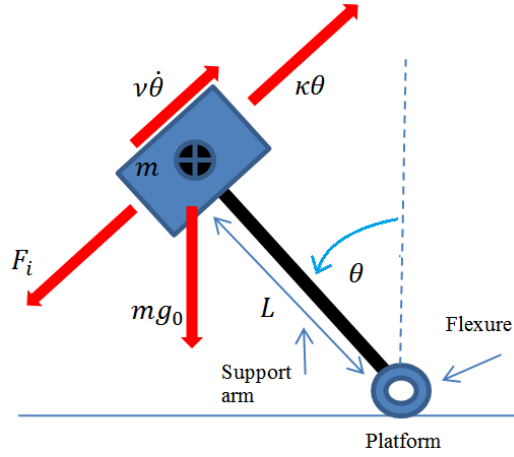


Figure 5: Inverted pendulum free body diagram

The physics governing the inverted pendulum are given by Newton's law of motion [26]

$$I\ddot{\theta} = L \sum F_i \quad (33)$$

where  $I = \text{mass moment of inertia about a point}$

$\theta = \text{angular displacement}$

$L = \text{pivot arm length}$

$F_i = \text{forces due to damping, gravity, thruster, and resistance}$

Assuming small displacement angle and rearranging variables, the equation of motion is

$$\ddot{\theta} + 2\beta\dot{\theta} + \omega_n^2\theta = \frac{L F_{ext}}{I} \quad (34)$$

$$\beta = \frac{vL^2}{I} \quad (35)$$

$$\omega_n^2 = \frac{Lg_0}{I} \left( \frac{kL}{g_0} - m \right) \quad (36)$$

where  $v$  and  $\omega_n$  are the system damping coefficient and natural frequency, respectively.

The restoring force coefficient is given by  $k$  and  $m$  is the body mass. Solving the

equation of motion, the thrust produced from the thruster is determined by the pendulum measured angular displacement ( $\theta$ ) [26]. Equation 43 gives a linear relationship between thrust and angular displacement.

$$T = g_0 \left( \frac{kL}{g_0} - m \right) \theta \quad (37)$$

Thrust produced by a Hall thruster is usually constant over time while operating under a single condition. Therefore, thrust is measured for various operating conditions. This is done by either adjusting the anode potential or mass flow rate. The mass flow rate is usually kept constant while varying the voltages. Combining measured thrusts with Equation 2, specific impulse of the thruster can be plotted for various anode voltages. A typical plot of such performance parameters for Hall thruster is illustrated in Figure 6. The specific impulse rises as the anode voltage increases. This trend is expected in a Hall thruster because a higher anode potential would produce a higher ion exit velocity, leading to higher thrust and specific impulse.

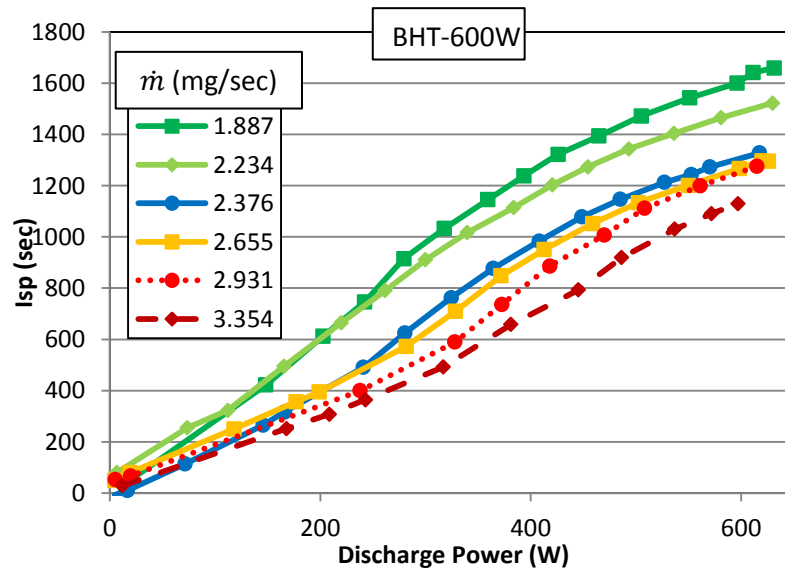


Figure 6: Anode specific impulse for various discharge voltages for BHT-600W.

### *B. Faraday Probe*

A Faraday probe will be used for far-field measurement. It is an intrusive method. Faraday probe works by collecting ions in the plume with its uniform collector plate. The probe entrance consists of a guard ring that is negatively biased to repel electrons from entering the collector while allowing positive ions to pass through. At the other end of the probe is a collector plate that has a positive bias; this allows lower energy ions to repel away from the plate while allowing higher energy ions to be collected. Low energy ions are produced by charge exchange, and can significantly skew results [24]. Ions absorbed by the collector induce some amount of current and provide the ion beam current density [24].

There are many types of Faraday probe that can reduce errors from their measurements. Some of the popular probes include nude probe, coupled, magnetically filtered, and nested. These variants were created to reduce charge exchange, electron bombardment, background pressure effects, plume divergence, secondary electron emission, and facility effects [23]. These factors make it difficult to conduct an accurate measurement of the beam current. The schematic for a generic Faraday probe is illustrated in Figure 10. The aperture has a biased voltage and opening that only allows ions to enter and collide with the collector plate. The collision will induce a current through a resistor and produce a voltage drop. This drop in voltage, along with a known resistor, allows calculation of the ion current density at a single point in the plume.

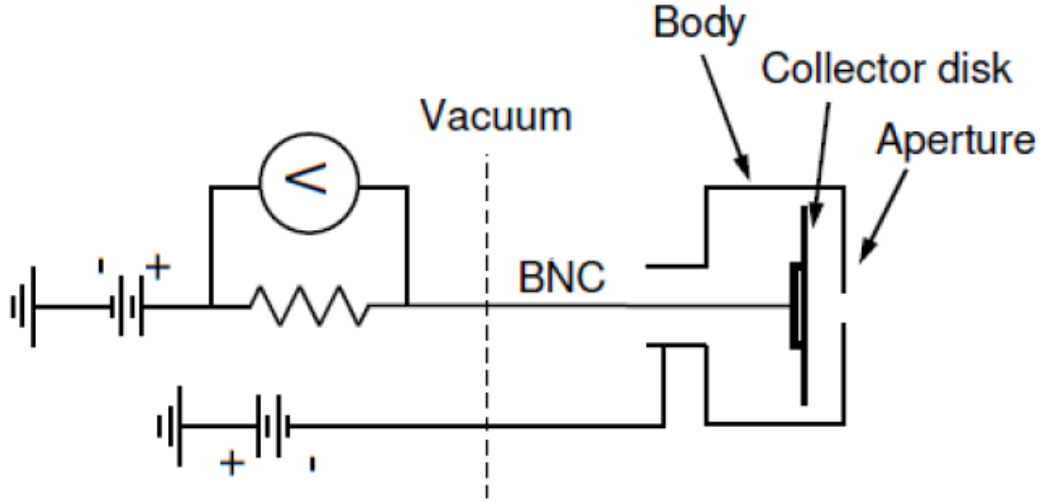


Figure 7: Schematic for Faraday probe. Adapted from Farnell [45, 52]

The Faraday probe measures local beam current density. The current density is defined as the measured current divided by the aperture area [19]. The probe was designed to provide the local plasma beam current density  $j_B$  derived from Ohm's law as given by Equation 38 [36].

$$j_B = \frac{V}{R \cdot A_{aperture}} \quad (38)$$

$R$  and  $V$  are the collector plate resistance and associated dropped in voltage, respectively. However, the probe yields only a single measurement for each point in the plume. Therefore, the current density measurement is needed for different angular positions [19]. The total beam current density distribution  $I_b$  has to be numerically integrated over an entire beam sweep radius. It is given by Equation 39.

$$I_b = \iint j_b dS \quad (39)$$

A correction must be applied due to beam divergence  $F_t$ . It is given by the following:

$$F_t = \frac{\iint j_b \cos \theta dS}{I_b} \quad (40)$$

The current density distribution is highest at the thruster center line and approaches zero for higher divergence angle. Typical results for Faraday probe measurement is shown in Figure 8. The plot shows the relationship between the beam current density and probe locations relative to the centerline for different mass flow rate. It shows both left and right divergence angles from the centerline so the symmetry could be evaluated.

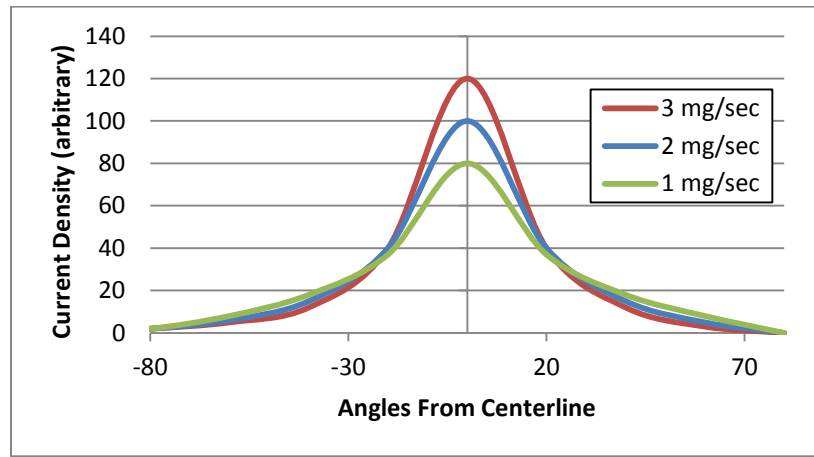


Figure 8: Typical current density distribution for the exhaust plume.

### C. ExB Probe (Wein filter)

The ExB probe, or Wein Filter, acts as a velocity filter because it allows only ions with certain velocity to pass through the probe. The probe consists of three main components: entrance collimator, ExB filter, drift and collector section[37]. Figure 9 illustrates the probe schematic. The entrance collimator allows a narrow beam to enter the probe. Its function is to repel the electrons and allow ions to pass. The electric and magnetic fields are perpendicular to each other. The fields are also oriented normal to the direction of the beam so a force is applied to the incoming ions.



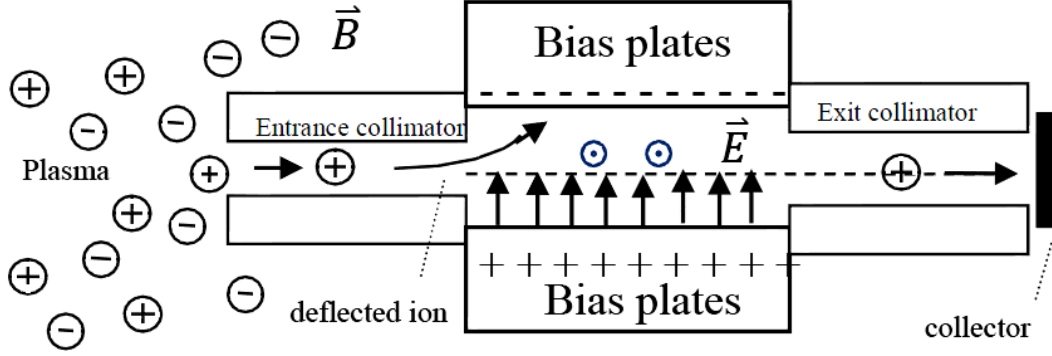


Figure 9: Typical schematic for ExB probe.

ExB probe operation is based the principle of Lorentz Force, as given by Equation 41 [22].

$$\vec{F}_i = q_i (\vec{E} + \vec{v} \times \vec{B}) \quad (41)$$

The ExB filter allows ions with a specific velocity that transverse the ExB section to pass un-deflected, through the exit collimator, and then collide with the collector to produce a current. The electric and magnetic fields are balanced so that no net force is acting on these particles as they pass through the filter section. The magnetic field is produced by a permanent magnet and cannot be adjusted. Therefore, only the electric field strength is adjusted by varying the probe potential,  $\Delta V_{probe}$ . This relationship is given by Equation 42 [20, 21].

$$\Delta V_{probe} = B \cdot d \sqrt{\frac{2eZ\Delta V_i}{m_{Xe}}} \quad (42)$$

where  $\Delta V_i$  is the accelerating voltage of the ion.

By adjusting the electric field, the ions entering the probe with zero net force will impact the collector plate and yield a current. This is done by sweeping the probe voltage over a range of interest that produces a corresponding current. The voltage distribution

can be related back to the energy or velocity of the singly and multiply charge ion, producing the ion species fractions given by the following relationships [15, 20, 21]:

$$\Omega_i = \frac{n_i q_i^{3/2}}{\sum n_i q_i^{3/2}} = \frac{I_i}{\sum I_i} \quad i = 1, 2, 3 \quad (43)$$

$$\zeta_i = \frac{n_i}{\sum n_i} = \frac{\Omega_i / q_i^{3/2}}{\sum \Omega_i / q_i^{3/2}} \quad i = 1, 2, 3 \quad (44)$$

where  $\Omega_i$  is the beam current fraction and  $\zeta_i$  is the ion species fraction.

A typical result from ExB probe is illustrated in Figure 10. The plot shows the relationship between the beam current and sweep probe voltages. There are distinct peaks for certain probe voltages. These peaks represent relative species concentration within the plume. They are the ions that were allowed to pass the ExB filter section and collided with the collector to yield a peak in the measured current. For a Hall thruster that uses Xenon, there are usually three distinct peak correlate to presence of  $Xe^{+1}$ ,  $Xe^{+2}$ , and  $Xe^{+3}$ .

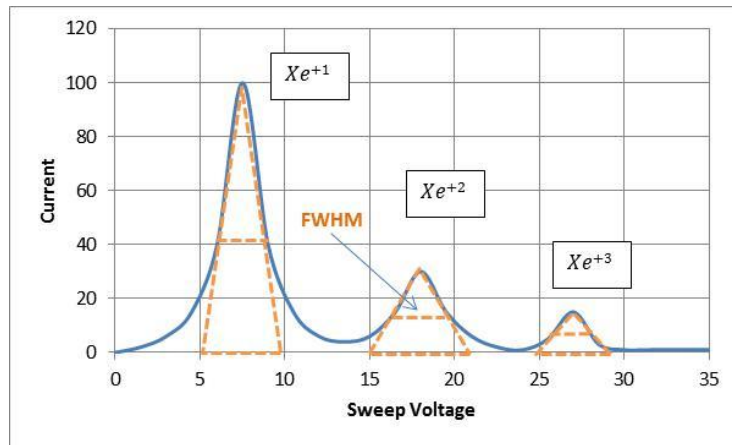


Figure 10: Typical ExB probe sweep.

The current fraction can be determined from triangle fitting of the peaks, because the area of the triangle is assumed to be the current for corresponding species [21]. The triangles are given by intersecting lines between the peak and the point of half-maximum (FWHM). This simple model has shown that using a triangle to approximate the velocity distribution is adequate to capture the broadening effect in species fraction calculation [21]. The species fraction is related to current fraction as given by Equation 44. It is an important factor in determining the thruster overall efficiency, because ion species fraction is an important variable in determining the multiply-charged ions correction factor ( $\alpha$ ).

Additional diagnostic tools are presented in Appendix A. However, this experiment will only use the inverted pendulum, Faraday probe, and ExB probe to examine the exhaust plume properties. The inverted pendulum used for direct measurement of thrust. The Faraday probe will be used to evaluate divergence angle and the beam current density profile. The ExB probe will be used to determine the ion charge state or species fractions.

### **III. Methodology**

The research experiment was conducted at the Air Force Institute of Technology's (AFIT) Space Propulsion Analysis and System Simulation (SPASS) Laboratory. This facility houses the largest vacuum chamber at AFIT as well as all the required instruments for this research [36]. It has an abundant heritage because many previous research projects were conducted here. The procedures and instructions for operating the equipment were well developed. They help ensure repeatability in the experiment and reduce sources of error.

#### **III.1 Vacuum Chamber**

The laboratory contains a vacuum chamber that was manufactured and installed by PHPK Technologies, located in Columbus, Ohio. The vacuum chamber is about 2.6 meters long and 2.0 meters wide, with eight 0.23 meters windows for observation within the chamber. It also contains 14 additional ports for various connections to the chamber such as pipes, wirings, valves, pass-through, and fittings. This vacuum chamber was observed to have the capability to pump down to  $10^{-8}$  torr with an empty tank. The primary function for this vacuum chamber is to research electric propulsion thrusters at AFIT. This chamber is very reliable and was used extensively by previous students to conduct similar research. The vacuum chamber at AFIT can be seen in Figure 11. All the supporting equipment are connected and placed near the chamber for easy control and access.

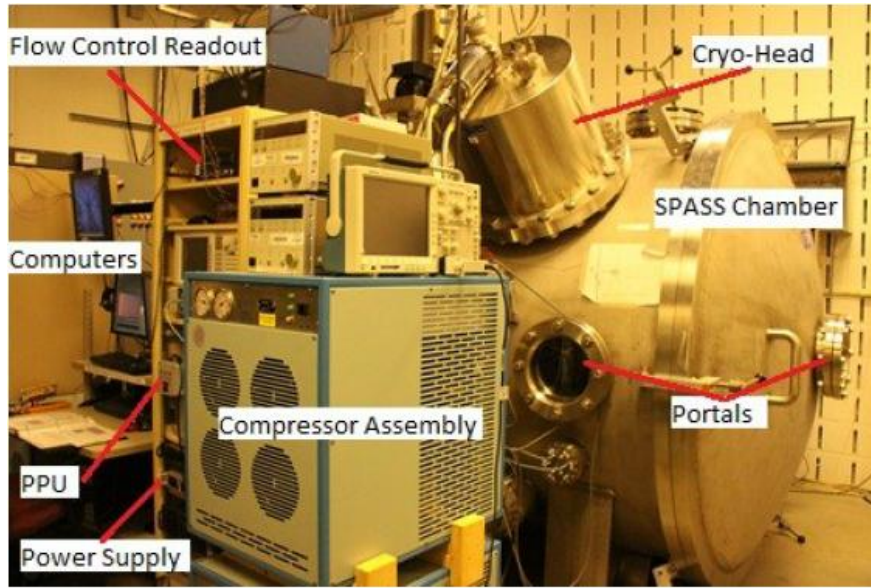


Figure 11: SPASS lab layout. Taken from Harpe [36].

The vacuum chamber is able to achieve  $10^{-8}$  torr through the use of a two staged pump system; roughing pumps for higher pressures and cryogenic pumps for lower pressures. The first stage of the pump down procedure is rough pumping, where most of the atmospheric air is mechanically pumped out of the chamber by an Adixen 2063C2 (It is a rotary vane vacuum pump produced by Alcatel Vacuum Technology). It was observed that the roughing pump reduces the chamber pressure down to a crossover pressure of about 50 millitorr in about two hours. At this point, the roughing pump stage shuts down and the cryogenic pumps start to activate the second stage of pump down sequence.

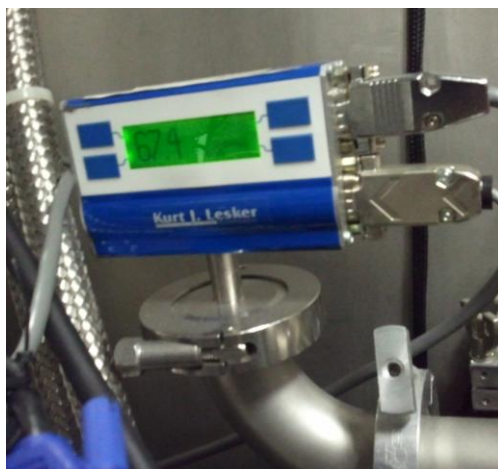
For pressures lower than 50 millitorr, the vacuum chamber operates on five helium cooled cryogenic heads; one CVI Torr Master TM250 and four CVI Torr Master TM500. The cryogenic pumps were produced and installed by PHPK Technologies of Columbus, Ohio. The cryogenic pumps are able to reduce the chamber pressure down to  $10^{-8}$  torr by

attracting atomic particles to cooled cryogenic heads. The cryogenic heads are cooled down to around 16-20 Kelvin by liquid helium, and are individually connected to CVI CBST 6.0 scroll compressor. Each of the CVI Torr Master TM500 cryo-pumps has a capability of pumping 4,000 liters per second of Xenon gas [36, 46]. However, the capability of a TM250 is about half that of a TM500 [46]. All five cryo-pumps are able to maintain the vacuum chamber pressure around  $10^{-5}$  torr when BHT-600 run at full capacity. The cryogenic pumps connections and features can be seen from Figure 11.

Throughout the experiments, the chamber was monitored by two independent pressure gauge systems: Lesker 300 Series Convection vacuum gauge and Extorr Residual Gas Analyzer (RGA) XT100. The two pressure gauges are illustrated in Figure 12. The Lesker 300 Series measures pressure by convection, while Extorr XT100 RGA has three integrated pressure gauges: Pirani gauge, hot cathode ion gauge, and quadrupole gauge [47]. Lesker 300 Series Convection gauge was used for measuring higher pressure because it has a range of  $10^{-4}$  to 1,000 torr [48], and is used mainly for monitoring roughing pump phase. The RGA XT100 was used for lower pressure measurement. It has the ability to measure pressure down to  $10^{-11}$  torr [47]. The signals from the gas analyzer are controlled by the communication and control unit, which is connected to a computer. The interface between the pressure systems and the computer is accomplished through Extorr's software called Vacuum Plus. The program is used to monitor the overall pressure as well as partial pressure of the constituent species. This interface is useful to the user because it can be used to identify leaks and species that dominate within the chamber. The user interface from Vacuum Plus can be seen from Figure 13.



(a) Extorr's gauge for low pressure range.



(b) Lesker's gauge for high pressure

Figure 12: Pressure gauges used to monitor vacuum chamber for all pumping stages.

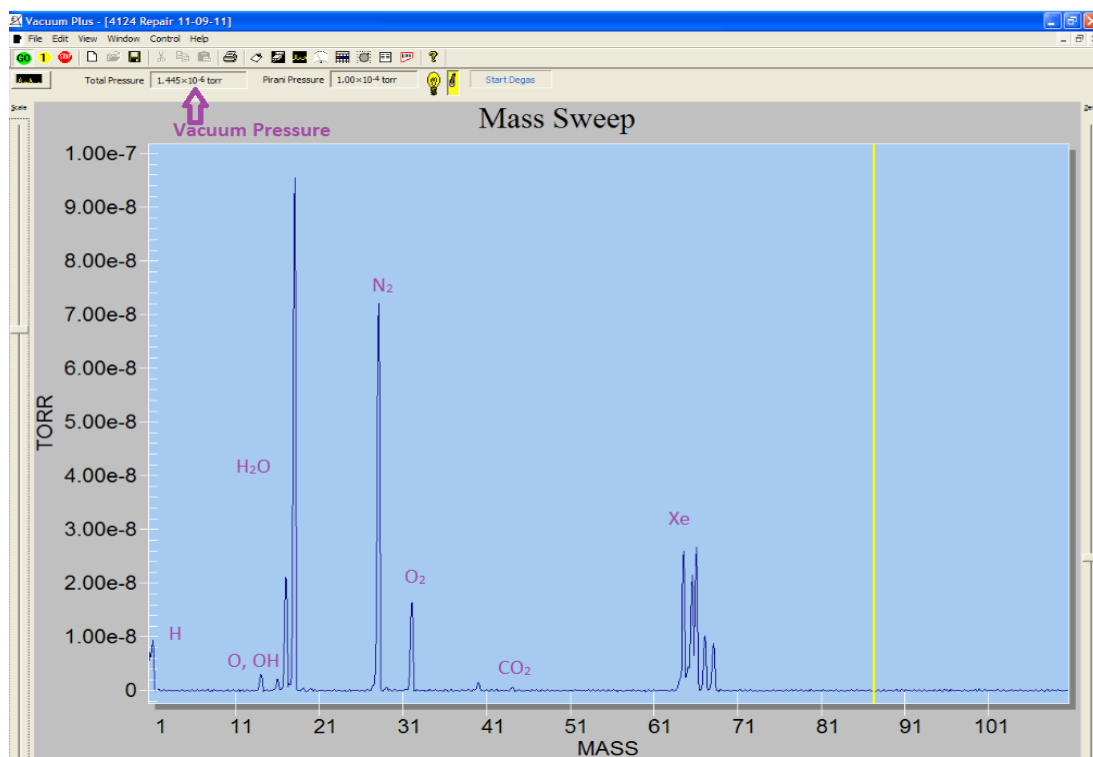


Figure 13: VacuumPlus software interface used for monitoring chamber pressure.

## III.2 Support Equipment

The chamber is capable of supporting various instruments including the thrust stand, Faraday probe, and ExB probe used in this experiment. The thruster and diagnostic instruments are mounted on various support systems so that data can be taken from various locations. The vacuum chamber is equipped with translational stages for the thruster, beam profiler for diagnostic probes, and various other instrumentation such as propellant feeds, power processing unit (PPU), and thruster control system.

### *A. Translation Stages*

The translation stage system is used to adjust the position of the thruster for Faraday and ExB probe measurements. This support equipment enables probe measurements at various distances from the thruster. This greatly reduces the error source in setting up the experimentation. Additionally, this system eliminates the need to shut down the chamber to adjust the thruster's position.

The translation stage system was developed and built by Aerotech. This system has the capability to move the thruster in three independent axes with sub-millimeter precision [46]. Due to the tank's physical dimensions, the system was limited to translating about 600 mm in the x-axis, 600 mm in the y-axis, and 600 mm in the z-axis [36]. The translation stage system was connected to Aerotech's A3200 Npaq controller box, which provides an interface between the computer and the stages. The user is able to control the system through a program called Nview HMI. This program has the option to execute in manual mode or automatic mode. This research only used the manual mode to operate the translation stages. Figure 14 illustrates the thruster mounted to a box frame,



which was connected to the translation system. This box frame was constructed from 80/20<sup>TM</sup> aluminum struts.

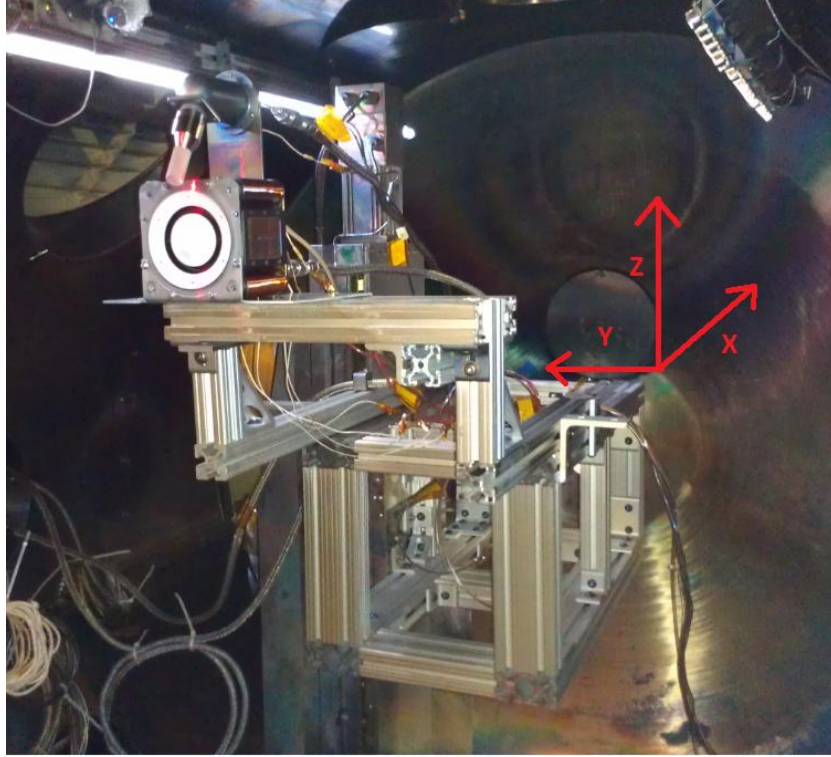


Figure 14: Thruster mounted on a box frame, attached to the translation stage.

### *B. Beam Profiler*

The beam profiler system is used to mount the Electrostatic Analyzer (ESA), the Faraday, and the ExB probes to measure the plume exhaust. This system was developed by Colorado State University. The main part of the system consists of two linear translation stages, which are illustrated in Figure 15. The two stages are capable of translating 100cm in r-axis and 100cm in z-axis. The probe mounting plate has the additional ability to provide the rotational stage, theta. The theta axis has a range of motion from 0-180 degrees. The system was mechanically translated by three step

motors. The motors use a water chiller unit, a Thermo Scientific NESLAB ThermoFlex 900, to dissipate the heat. The cooling unit is capable of maintaining temperatures as low as 5.0 degrees Celsius [53].

Other parts of the beam profiler system include power supplies and connections for the diagnostic probes, which will be discussed in more detail later on in the Diagnostic section. The connection between the translation stages and the computer is through a MC 224 Trio controller. The user interfaces with the system through a Labview program written by Colorado State University specifically for AFIT. The overall setup of the profiler enable the user to perform five different measurement techniques; Move and Measurement vs Time, Move and Probe scan, Linear scans, Radial scans, and Radial scans with Rotations. This research's only interest is in performing constant radial scan of the plume exhaust. Additionally, this experiment will only mount the Faraday and ExB probe onto the beam profiler system.

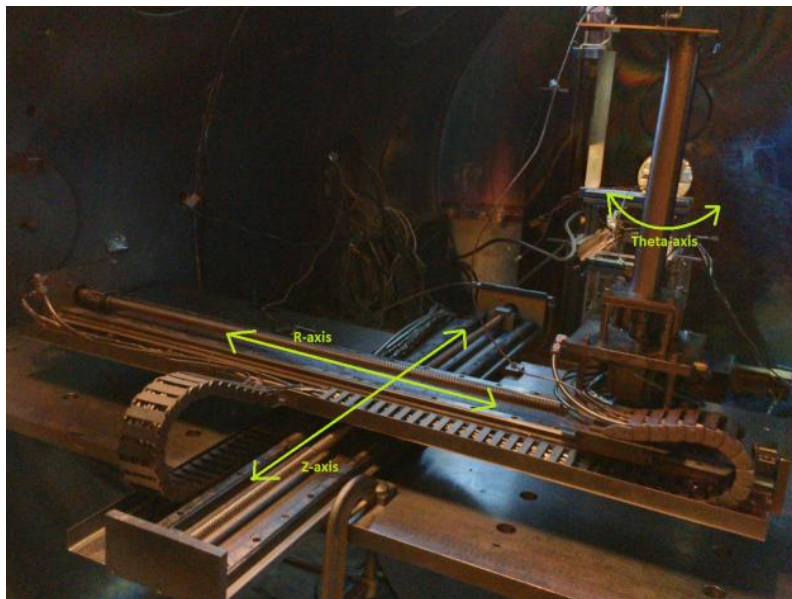


Figure 15: Beam profile system for mounting the Faraday and ExB probe.

### *C. Propellant Feed*

The facility is equipped to provide the chamber with Xenon and Krypton propellant. This experiment only used Xenon as the propellant. The Xenon gas was stored in a pressurized tank as indicated in Figure 16. The tank contains a regulator valve that reduces the inlet pressure from 100 psi to an outlet pressure of 20 psi. A propellant line then connects from the regulator valve to two MKS model 180A mass flow controllers. A controller connected to the cathode is limited from 0-10 SCCM, while the other, connected to the anode, will flow 0-50 SCCM. Both controllers are accurate within 0.01% of their maximum capacity [36]. The propellant then connects from the mass flow controller to the thruster and cathode within the chamber. The interface to the mass flow controller is through a MKS Type 247C 4-channel readout. The mass flow rate for the cathode was kept constant at 0.146 mg/s throughout the whole experiment.

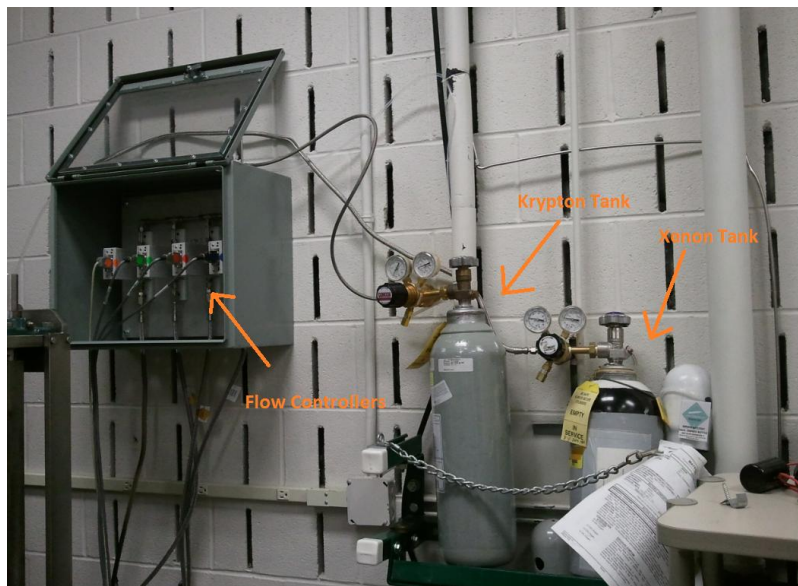


Figure 16: Propellant feed system.

#### D. Power Processing Unit and Control System

The BPU-600 Power Processing Unit (PPU) provides power to both the thruster and cathode. It receives power from a Sorensen DCS55-55E power supply that can be adjusted from 0-55V and 0-55A. The user interface from the PPU to the computer is through the BPU-600 Host Simulator software. This is LabView software provided by Busek. Figure 17 is an example of this interface. As seen in Figure 17, the user controls the thruster by selecting discharge voltage, magnet currents, and cathode currents. It was observed that the PPU produced a discharge voltage higher than the actual voltage supplied to the thruster and cathode. The difference was mainly due to losses in the electrical lines from the PPU, to the thruster within the chamber. The voltages that thruster and cathode received are about 0.1% different from the PPU.

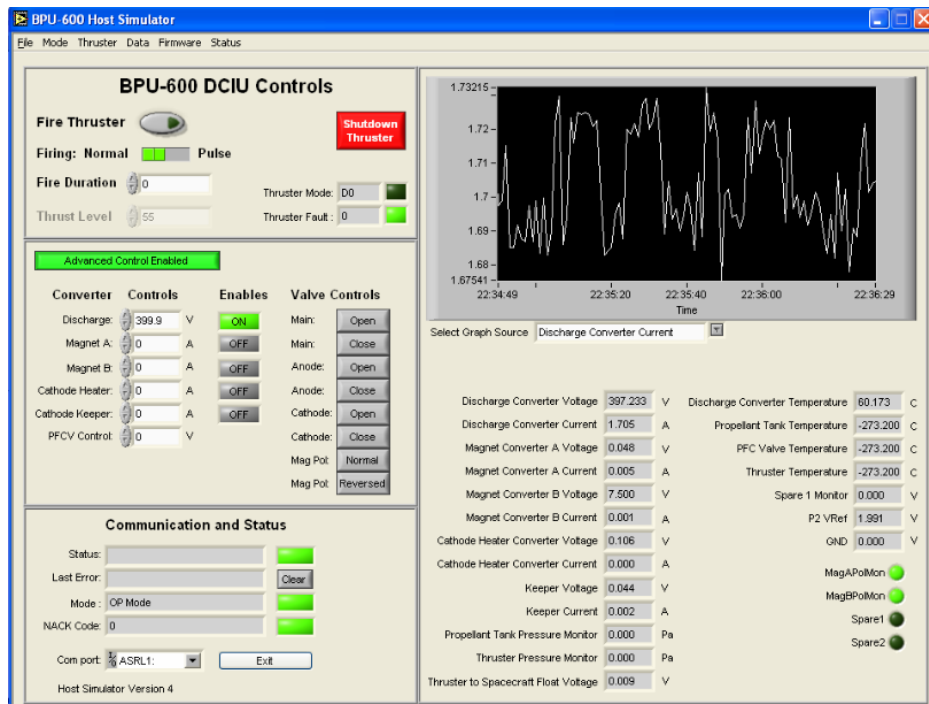


Figure 17: BPU-600 host simulator software used to control the thruster.

### III.3 Thruster

This experiment looked at the BHT-200W and BHT-600W thrusters. Both thrusters were produced by Busek. The BHT-200W thruster is similar to the BHT-600W but with lower power. It was used only as a baseline for this research because it has extensive heritage. The tests performed on the BHT-200W were at nominal conditions and used to validate the experiment equipment and methods.

A BHT-600W Hall thruster is the main interest of this experiment. It was specifically made by Busek for AFIT. This thruster was advertised to produce 42 mN of thrust, 1650s specific impulse, propellant mass flow rate of 2.6 mg/s, and propulsive efficiency of 55.0%. It has a discharge input power of 600 W, a discharge voltage of 300 V, and a discharge current of 2.05 A. It is optimized for operating “over a range of 300–600 W and produce 15–45 mN of thrust with a specific impulse of 1100–1700 sec” [33]. This Hall thruster contains two independent magnetic circuits which can be powered separately or connected in series. In addition, its special design features yield a steep axial magnetic field that is near zero close to the anode [49].

Similar to the BHT-200W, the BHT-600W was configured with a BHC-1500 hollow cathode. The hollow cathode also has abundant heritage, as it was demonstrated on orbit and used extensively by previous researchers. BHC-1500 is a barium impregnated hollow cathode. It was secured to the BHT-600W in a standard configuration with a mounting bracket provided by the manufacturer, as shown in Figure 18.

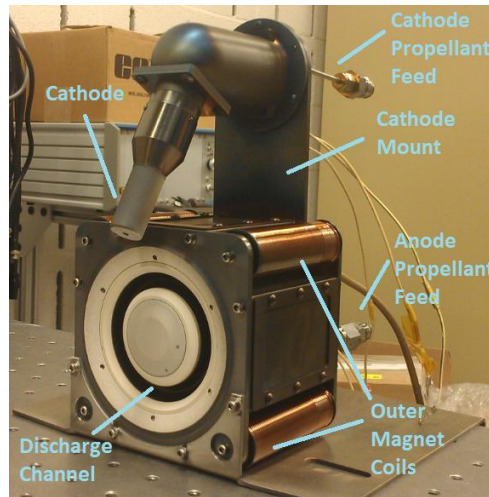


Figure 18: BHTC-1500 mounted on BHT-600.

### III.4 Diagnostic Equipment

This experiment used the inverted pendulum, the Faraday probe, and the ExB probe to examine the exhaust plume properties. The inverted pendulum was used for direct measurement of thrust. The Faraday probe was used to evaluate divergence angle and the beam current density profile. The ExB probe was used to determine the ion charge state or species fractions. These techniques are proven diagnostic tools in electric propulsion and should greatly reduce error sources. Additionally, these methods are relatively simple and inexpensive.

#### A. *Inverted Pendulum*

The BHT-600W's thrust profile for various discharge voltages and mass flow rates were measured using an inverted pendulum. The theory of operation behind this instrument was described in Diagnostic Tools in Chapter 2. Thrust was directly measured by using Busek's T8 inverted pendulum thrust stand. The main components of the thrust



stand are a linear variable differential transformer (LVDT), damper coil, 8 flexures, inclinometer, spring, damper coil, propellant feeds, and pendulum plate. The main part of this equipment is the LVDT used to determine linear displacement due to thrust [35]. The measurements are in volts and can be converted back into thrust using calibration curve. The thrust stand can be seen in Figure 19. The thruster was bolted securely to the stand that was placed on top of a steel plate for various tests.

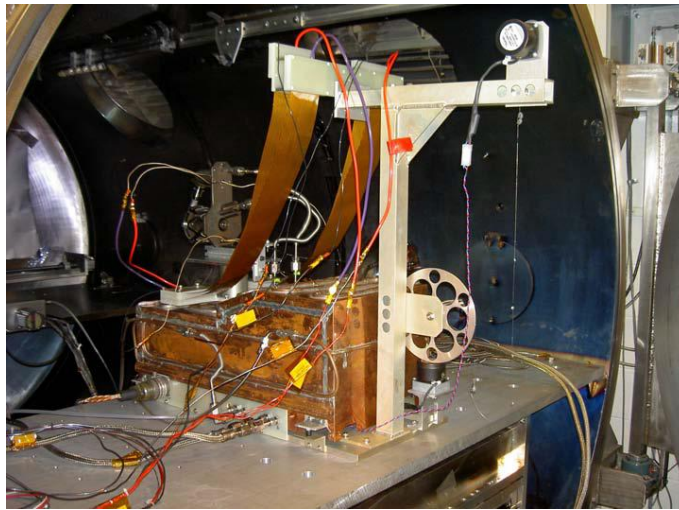


Figure 19: Inverted pendulum set up. Taken from Temkin [46].

The thrust stand system uses water along with a thermal jacket for cooling. Previous research showed that there is a need to compensate for thermal drift because it can influence the results [25]. The cooling water and thermal jacket serve to keep the temperature within a reasonable range to minimize impact to the measurement. The thermal jacket also helps prevent radiated heat and plasma interaction with the thruster. Figure 19 also illustrates the way the thermal jacket is secured onto the thrust stand. The cooling unit used for this research is NESLAB ThermoFlex 900 water chiller. It was placed outside the chamber and connected to the thermal jacket via plastic pipes. The

temperature was adjusted to 5 degree Celsius for this research. The water chiller is capable to keep the temperature stability within  $\pm 0.01$  degrees Celsius of the desired value [53].

The thrust stand was placed on a steel plate that was bolted to the chamber wall. This helps to reduce vibration transfer to the thrust stand that may distort the measurements. The thruster was mounted to the thrust stand by bolting it to a pedestal that rests on eight flexures. The flexures produce stiffness in the system and can be adjusted for various thrust level by changing their thickness. The springs created oscillation motion while the damper coil dissipated the motion energy and kept the system stable. They can also be changed to accommodate different thrusters. For this research, flexures and springs with thickness of 0.030in and 0.025in were used, respectively. The propellant feeds connect to the thruster in a spring like fashion, as shown in Figure 20. This configuration increased the overall spring stiffness of the inverted pendulum system.

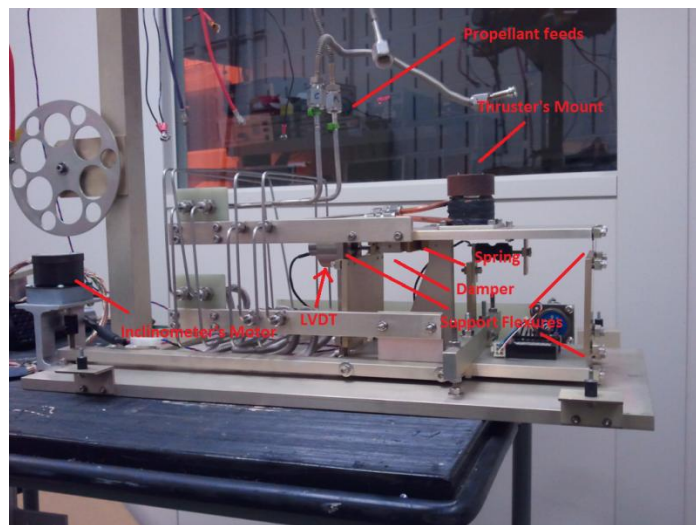


Figure 20: Uncovered Busek T8 inverted pendulum.



The signals out from the LVDT are in analog voltage. They were connected to Schaevitz MP2000 LVDT readout controller, which can be seen in Figure 21. The readout controller also enables the user to adjust the stand inclination to zero, which minimizes the effect of gravity on the system. It was observed that the inclination drifted slightly during each test and had to be manually adjusted to zero before proceeding. The readout controller also let the user control the damper magnitude. Previous research had shown that the damping circuit had little or no effect on the thrust stand; therefore, it is not used frequently throughout the experiment [46]. The damping circuit was turned on only for the large oscillations during thruster start up and shutdown. This reduced the time it took to perform calibration and measurement.



Figure 21: LVDT readout controller for thrust stand.

The interface between the readout controller and the computer was achieved through a LabView program developed by Busek. The program GUI is illustrated in Figure 22. The voltage signal from the readout controller was recorded by the program at

1,000Hz rate to produce repeatability. As seen in Figure 22, there are significant noise levels in the LVDT voltage readout. Therefore, an average of each reading was taken over 20 sec intervals.

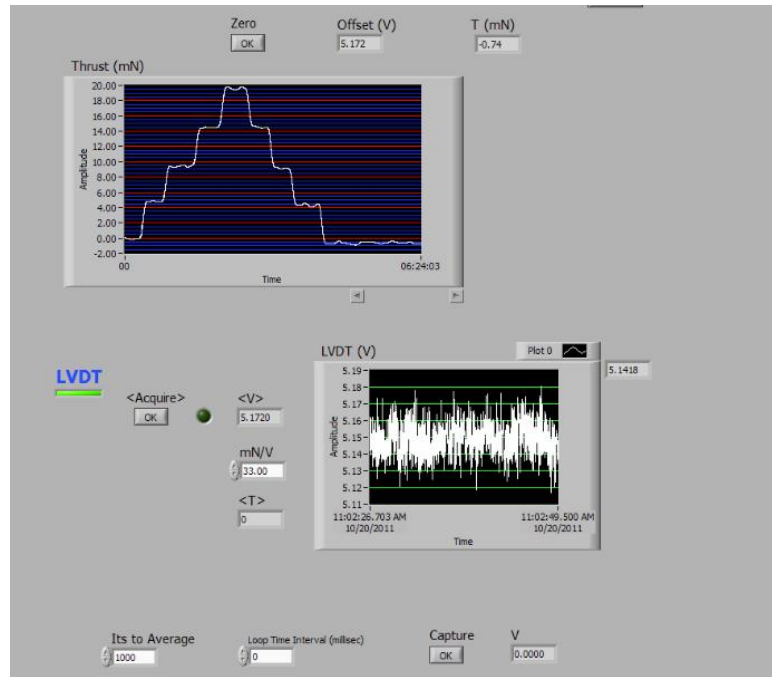


Figure 22: LabView interface for thrust measurement.

The thrust stand was calibrated by hanging a series of weights from pulleys that transferred vertical motion into translational motion to the LVDT. There were four 1.45 gram weights that were added incrementally by a motor that can be controlled by a switch on the readout controller box. The four weights yielded a calibration range of 0–55 mN. By applying increments of known weights, the LVDT will produce voltages associated to each applied force. The relationship between the known applied force and the associated voltages produce a calibration curve for thrust calculation. The same calibration process was applied before and after each test to ensure accurate measurement and minimize the effect of thermal drift.

### *B. Faraday Probe*

Ion current densities were measured by a guarded Faraday probe. The theory of operation behind this instrument was described in Diagnostic Tools in Chapter 2. The Faraday probe was developed and produced for AFIT by Colorado State University. The probe consists mainly of an aperture, collector disk, and body. The aperture has a diameter of 0.03in or 0.0762cm, which equates to an aperture area of  $0.00457 \text{ cm}^2$ . Figure 23 shows the physical features of the Faraday probe, as well as its attachment to the beam profiler system. As discussed earlier, the beam profiler system was used to mount various probes for exhaust plume measurements.

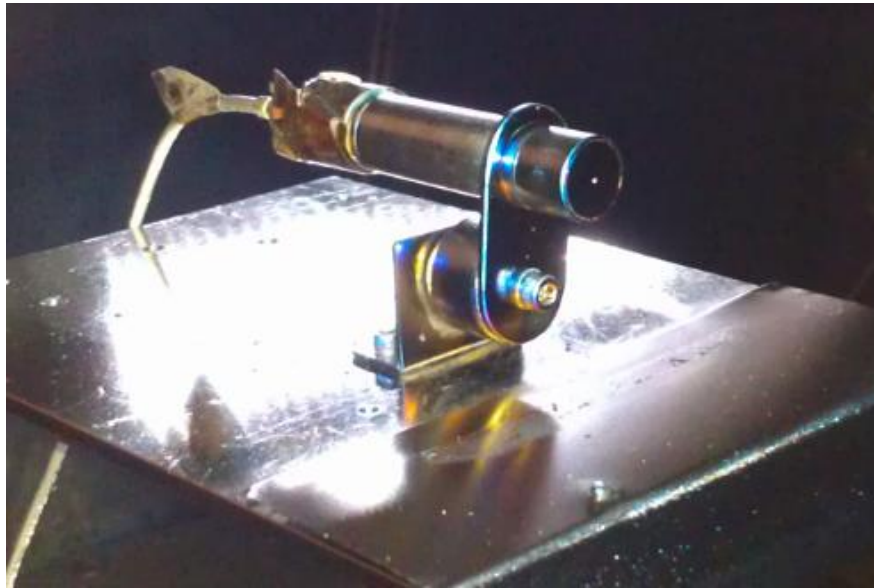


Figure 23: Faraday probe.

The increase in current due to ion bombardment of the aperture was measured by the increase in voltage at a resistor that was placed in an electrical lead between the collector disk and ground. The voltage drop in the system was measured by using an Agilent 34970A data acquisition unit and the resistor was 4.66 MOhm. Additionally, the

same collector lead was biased to +30V from ground by using a Keithley 6517A electrometer/high-resistance meter. The bias helps repel any low energy charge exchange ions that exist within the vacuum chamber. Similarly, the probe body was biased to -30V of ground by using Agilent 6018A power supply. This would prevent any electrons in the exhaust beam from reaching the collector plate. The voltage signals from the Agilent 34970A data acquisition unit were connected to and processed by the beam profiler system. As discussed earlier, a LabView program designed by Colorado State University was used to perform constant radial scans of the exhaust beam. The interface to operate the Faraday probe can be seen in Figure 24. There are various parameters the user can adjust to satisfy the experiment requirements.

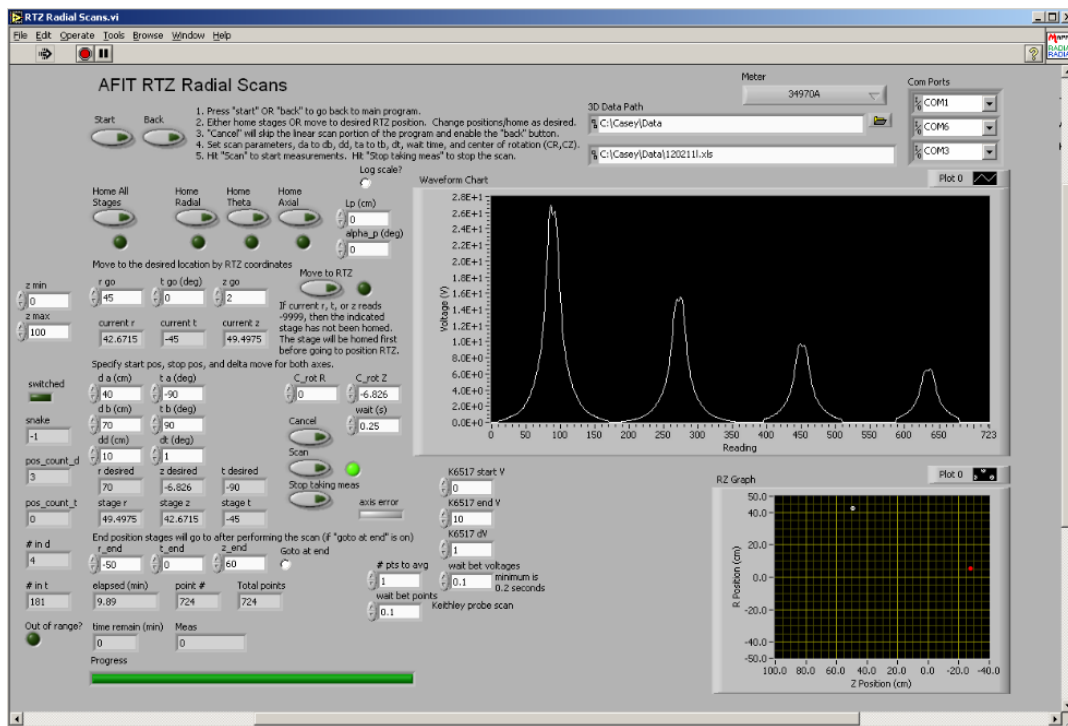


Figure 24: LabView interface for Faraday and ExB measurements.

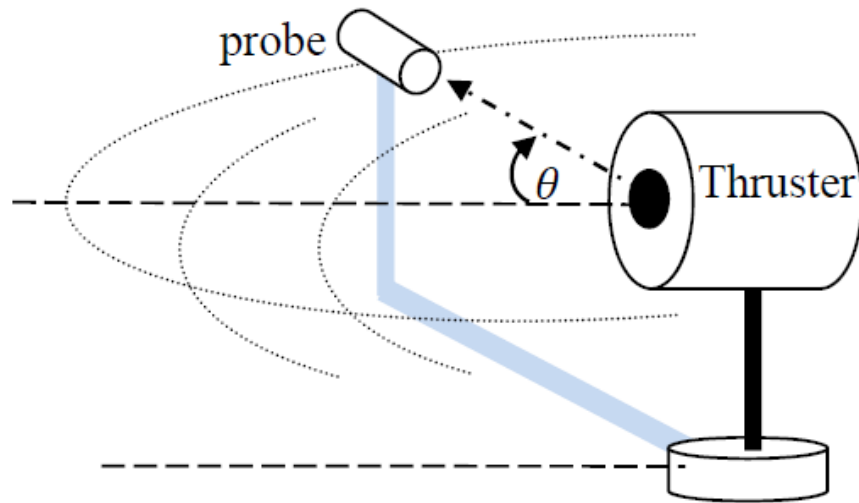


Figure 25: Schematic for Faraday probe setup.

The schematic set up for the Faraday probe is illustrated in Figure 25. The thruster was mounted on Aerotech translation stage and the probe was secured to the beam profiler system. The probe was placed at 40-70cm axial distance from the thruster exit plane. The probe must be positioned at least 40cm from the thruster exit due to the beam profiler system limitation and the power supply's ability to apply the bias voltage. Additionally, being too close to the thruster could potentially overload the Agilent power supply [41]. For each radial location, the probe was set to sweep from  $-90^\circ$  to  $+90^\circ$  from the thruster centerline at  $1.0^\circ$  increments with a dwell time of 5 seconds per angle. Again, due to the tank and beam profiler system physical limitations, the maximum arc the probe travels was different for each radius, and were never able to reach  $\pm 90^\circ$ . The probe was leveled with the thruster exit and remained constant throughout the sweep. A DeWalt laser was used to align the probe aperture with the thruster exit plane. A standard ruler was used to measure the radius from the probe aperture to the thruster exit plane.

### C. ExB Probe

Ion species fraction was measured by the ExB probe. The theory of operation behind this instrument was described in Diagnostic Tools in Chapter 2. The ExB probe was developed and produced for AFIT by Colorado State University. As illustrated in Figure 26, the probe consists mainly of the entrance collimator, body housing, ExB section, drift tube, and the collector plate [50]. The entrance collimator used in this research has 0.015" diameter orifices, which yielded an acceptance angle of  $\pm 0.30^\circ$  [50]. This is critical in measuring the incoming ion because it allows the ions to travel through the filter and drift section toward the collector without colliding with the instrument wall. The collector plate was located downstream of the drift tube, which was made from tungsten [35]. Its function was to measure current for various applied voltage potentials from any ions that were not greatly affected by the ExB section. The ExB section was where the electric and magnetic fields were applied to separate different ion species. The magnetic field was produced by permanent magnet and has constant magnitude of 0.7 Tesla while the electric field was generated by voltage potentials between two plates.

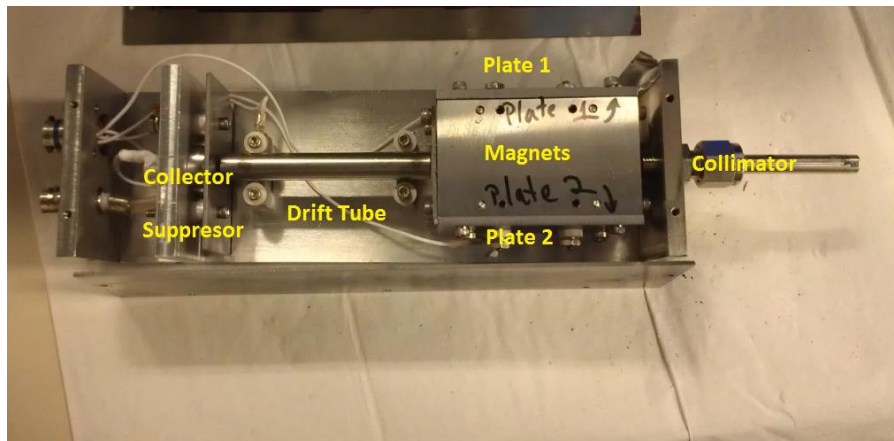


Figure 26: Uncovered ExB probe.

The electrical diagram for ExB probe can be seen in Figure 27. First, the plasma enters the entrance collimator. The collimator was grounded to discharge the filtered ions colliding with the wall, which only allows ions with a straight path to pass into the next section. In the ExB region, a Keithley 6517A electrometer was used to set the voltages on the power supply which gave the voltage potential on the plates to generate electric field. The same power unit was also used to read the current from the collector plate. The induced currents were generated from ions collided with the collector plate. In front of the collector plate was the suppressor, which was biased to -30V by Agilent 6018A power supply to reject electrons that passed the entrance collimator or were generated from secondary electron emission. Similar to Faraday probe, the signals from the Keithley 6517A electrometer were connected to, and processed by, the beam profiler system. The same LabView program designed for the Faraday probe was also used for ExB probe. There, the user was able to adjust various settings for the experiment.

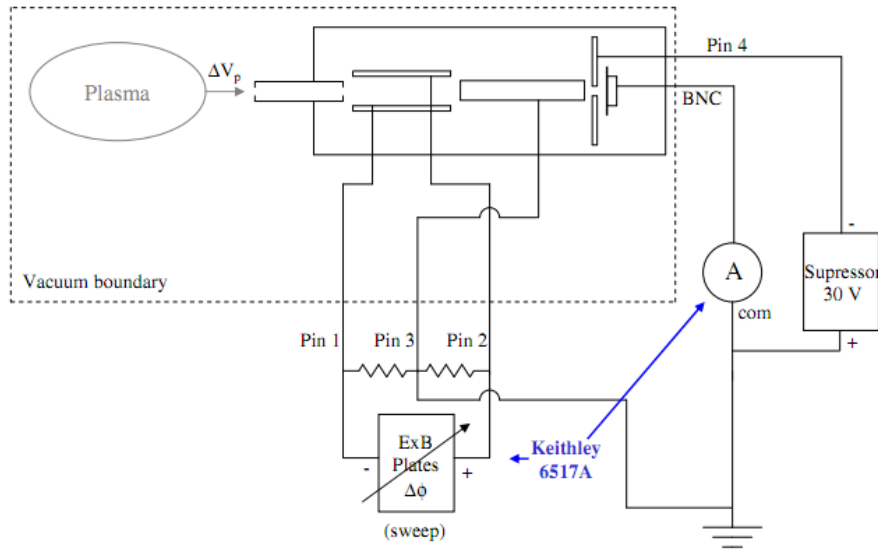


Figure 27: ExB probe electrical diagram. Taken from Farnell [45].



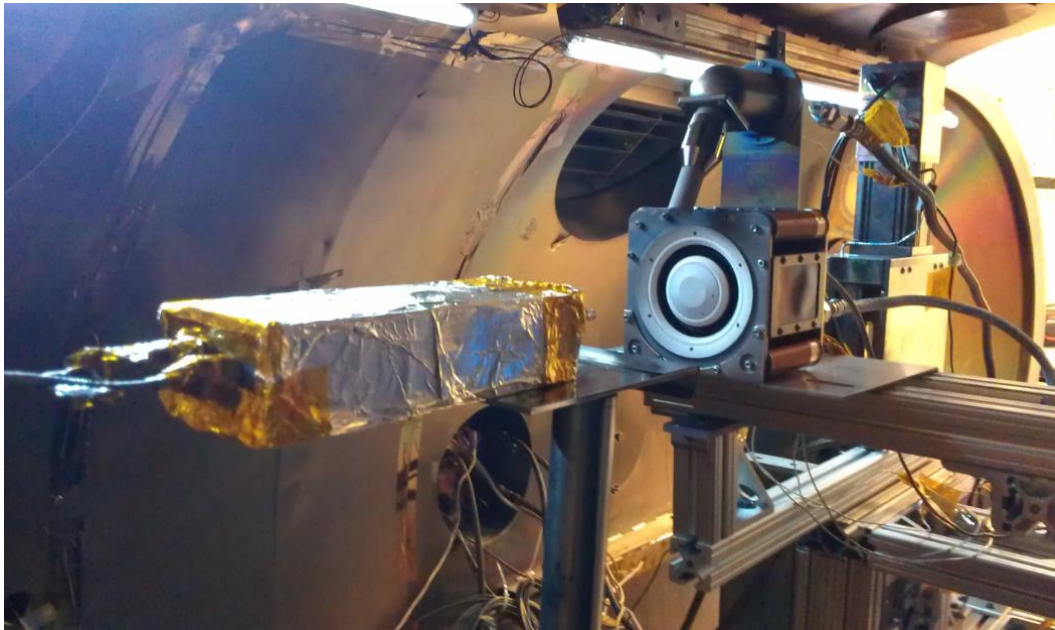


Figure 28: Mounting of ExB probe for measurements.

The ExB probe was mounted on a support system in the same method as the Faraday probe, as illustrated in Figure 28. The probe entrance was positioned 60cm axially away from the thruster exit plane. A ruler was used to measure the radius from the probe entrance collimator to the thruster exit plane. The difficulty of using an ExB probe was in its alignment with the plume. The acceptable angles for this probe need to be very accurate, usually limited to 0.50 degree [22, 50]. Therefore, a DeWalt laser was used to align the probe with the thruster exit plane. The voltage potential that generates the electric field was swept from 0 to +50V in 0.1V increments, which included most multiply-charged species. Each data point was generated from an average of 3 samples. The data from the ExB probe was used to provide ion species concentration within the plume.



### III.5 Error Analysis

Error analysis for this experiment could be a very complex process because there are potentially thousands of sources contribute to the errors. The thruster's performance and characteristics were calculated from several variables described by different equations. These relationships depend upon several measurements; therefore, it was hard to estimate the possible errors in computing the results. Due to time constraint and complexity, this research used a simple method based on the Pythagorean Theorem. The total uncertainty of measurements was calculated from the following.

$$\sigma_{total} = \sqrt{\sum \sigma_i^2} \cong \sqrt{\sigma_{equip}^2} \quad (45)$$

Assuming a desired 96% confidence gives:

$$\sigma_{equip} = 1.96 \frac{Dev}{\sqrt{N}} \quad (46)$$

Where  $N$  is the number of samples and  $Dev$  is standard deviation of corresponding measurements. The symbol  $\sigma_i$  represents error components contributed from different measured sources such as calibration, thermal drift, dimension measurements, data processing, etc. This research simplified the method by assuming these systematic errors to be small comparing to equipment errors and therefore neglected. Other sources of error that may contribute to inaccurate results are human errors in reading the data and randomness in the system.

## **IV. Results and Analysis**

The experimental set up from the previous chapter has been used to determine BHT-600W performance for various operating conditions. The measured data from different instruments enabled the calculation of Voltage-Current curve, thrust, propulsive and beam efficiencies, plume current density, and ion species fractions. The effects on these characteristics are presented as a function of anode discharge voltages, mass flow rates, and inner and outer magnet currents.

### **IV.2 Thruster Performance**

This research determined that the BHT-600W nominal performance was lower than, but close to the advertised values from Busek Co. It was concluded that the thruster's nominal performance actually occurred at propellant flow rate of 2.888 mg/s, discharge voltage of 300V, discharge current of 2.0A, and both magnet currents at 1.75A. At this condition, the measured thrust was  $34.8 \pm 1.3$  mN, specific impulse was  $1,134 \pm 39$  sec, with beam efficiency of  $52.1 \pm 0.27\%$  and overall efficiency of  $34.8 \pm 2.4\%$ . The thruster's performance changed with different discharge voltages, mass flow rates, and magnet currents, which will be discussed further in this chapter.

The initial results showed the thruster's maximum discharge power at 622W. Any increase in power beyond that point resulted in thruster shutdown. However, the manufacture claimed that BHT-600W could operate up to 800W. The safety limit placed in the BPU-600 Host simulator software and the thruster design initially was assumed to be responsible for the shutdown beyond 625W. Therefore, the design of experiment for this research revolved around the nominal condition and maximum discharge power.

Because of this, all measurements were taken at operating condition from 0-625W. Only at the end of the research it was discovered that the problem was from the power unit for the PPU of the thruster. There was not enough power supplied to the thruster causing it to shutdown at 622W and higher.

#### *A. Voltage-Current Curve*

One of the objectives for this research was to determine the BHT-600W operating envelope. The most direct method was to examine its Voltage-Current curve (V-I curve). The curve revealed the location of different preferred operating modes of the thruster such as current limit and voltage control mode. It relates discharge current behaviors as a function of anode discharge voltages and mass flow rates. The V-I curve for BHT-600W is illustrated in Figure 29. For this experiment, discharge currents were measured at five different mass flow rates while varying discharge voltage from 60V to 400V. Five mass flow rates were chosen, ranging from a minimum of 2.079 mg/s to a maximum of 3.092mg/s. The higher propellant flow rate of 3.092 mg/s was chosen because it was the highest flow rate the thruster was able to maintain in voltage control mode before transiting to current limit mode. The lower propellant flow rate of 2.079 mg/s was chosen because it was the point that yielded discharge power of 625W. As discussed previously, any discharge powers higher than 625W caused the thruster to shut down. It was also a condition that corresponds to the maximum discharge voltage of 400V, which was limited by BPU-600 software. Due to the software limit and different operating modes of the thruster, this research was able to only investigate discharge voltages from 60V to 400V. Additionally, the manufacturer advised that the thruster was not designed to

operate higher than 400V. Any discharge voltages higher than 400V would potentially cause damage to the thruster. A lower discharge voltage of 60V was chosen because it is a region where the thruster starts to transition from voltage control mode to low current and current limited mode.

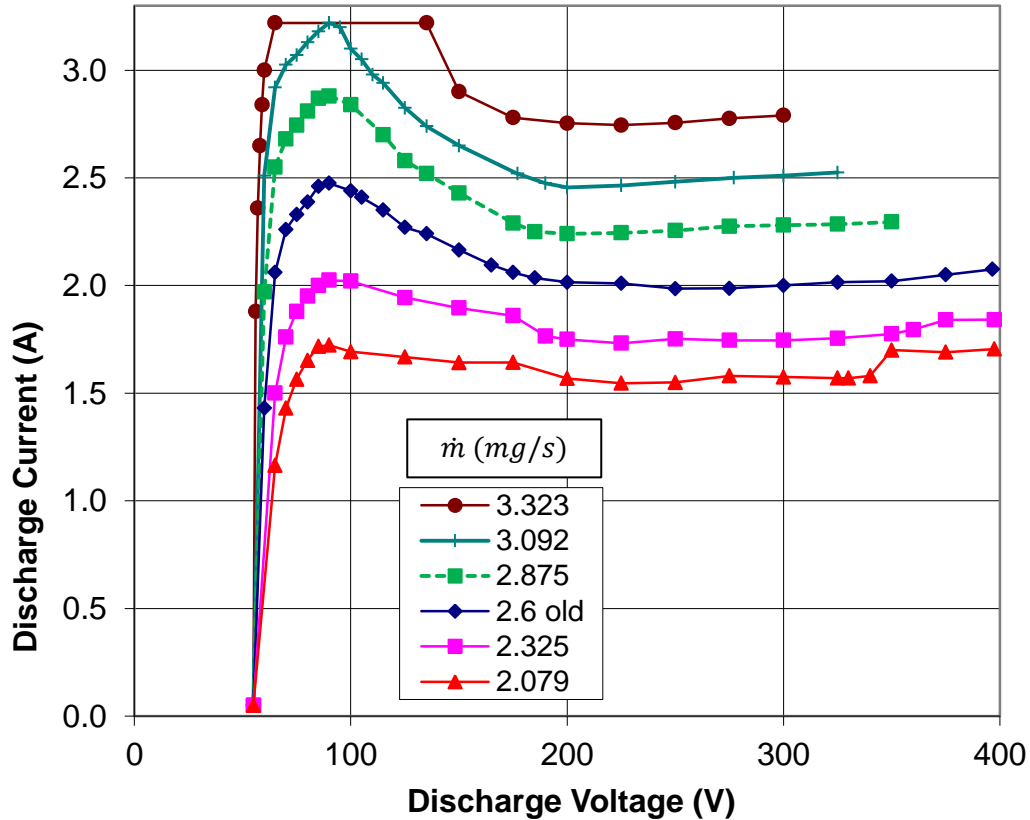


Figure 29: V-I curve for BHT-600W

The V-I curve showed discharge current as a function of discharge voltages for various propellant flow rates. Regions to the left within the V-I curve are the conditions where the discharge current drastically dropped to near zero or low discharge current mode. These conditions had lower discharge voltages, which most likely caused a reduction in ionization process due to reduction in discharge potential. This phenomenon

also drastically reduce thruster performance measures such as thrust to zero, which was confirmed with thrust measurements discussed in latter section. The exhaust plume at these conditions seems to produce a ball type plume, as typically can be found in Hall thrusters [46]. This characteristic is illustrated in Figure 30. The purple glow is characteristic of xenon propellant.

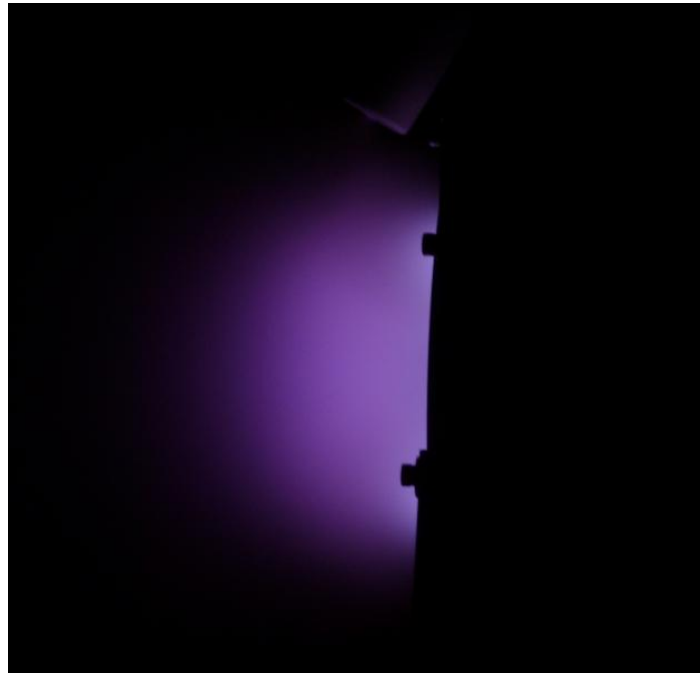


Figure 30: Ball plume shape from low discharge current mode.

The top region in V-I curve-represent operating conditions where the thruster entered current limit mode. It dominates at high propellant flow rates and low discharge voltages. The current limit mode for BHT-600W holds a maximum discharge current of 3.22A. Thrust measured from this mode was much lower than voltage control mode, and therefore was not investigated further in this research. The shape of the plume in current limit mode is illustrated by Figure 31. At discharge voltages from 100V up, is the voltage control mode regime. This is the region where the thruster should operate, because it

produced the most thrust, specific impulse, and highest efficiency. The shape of the beam exhaust in this region was a typical jet plume, which can be seen in Figure 32. The jet was more prominent at higher discharge voltages and less so at lower. One can see the strong central cone resulting from the circular geometry of the thruster.

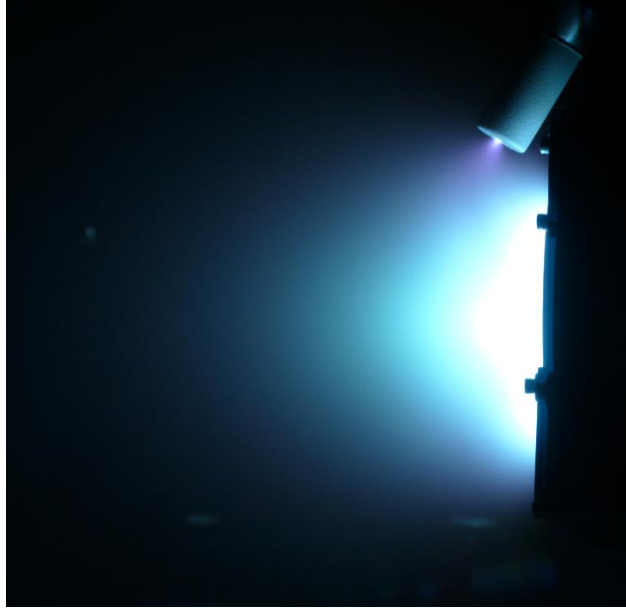


Figure 31: Plume shape of the current limit mode.



Figure 32: Jet plume shape found in voltage control mode.

For lower propellant flow rates, discharge current remained fairly constant for discharge voltages from 80V to 400V. However, as propellant flow rate increased, the discharge currents seemed to increase with decreasing discharge voltages. The V-I curve showed a linear relationship between discharge current and discharge voltages at higher mass flow rates. This was most likely due to lower discharge voltage causing an increase in resident time for the ions. Higher number of ions within the discharge chamber means more paths for electrons to travel, yielding an increase in discharge current. Another phenomenon observed was that discharge currents changed sharply around discharge voltage of 175V and 350V for lower mass flow rates at 2.325 mg/s and 2.079 mg/s. Observation revealed these conditions produced high fluctuation in the discharge current. We hypothesize this is due to thruster instability. Figure 33 shows this fluctuation. At the same mass flow rates, high fluctuation in discharge current was also detected for discharge voltage of 400V. The exhaust beam also had an intense and sharp center cone, however, the beam seemed to fluctuate between nominal jet shape and a more focused, wider cone. The differences are best illustrated and compared in Figure 34.

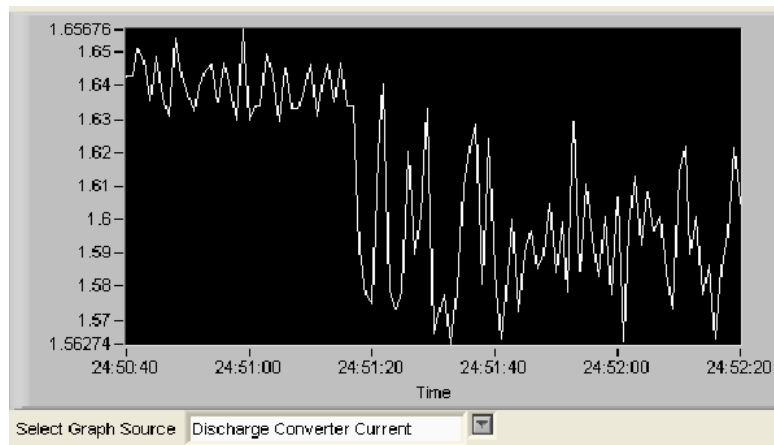


Figure 33: Discharge current fluctuation from thruster's instability.

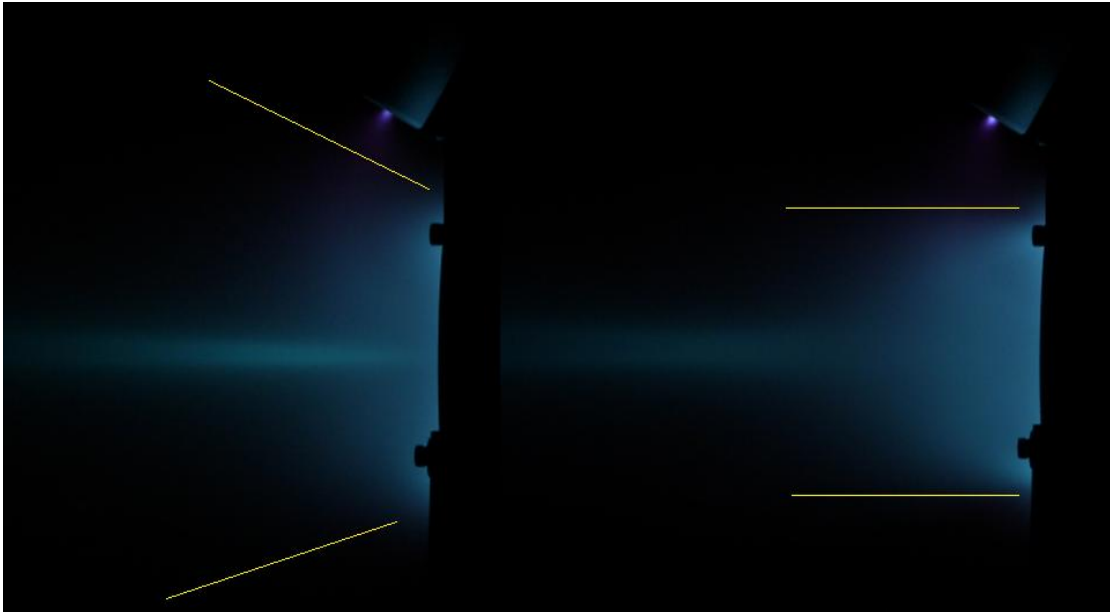


Figure 34: Outer or wider cone instability at higher discharge voltage.

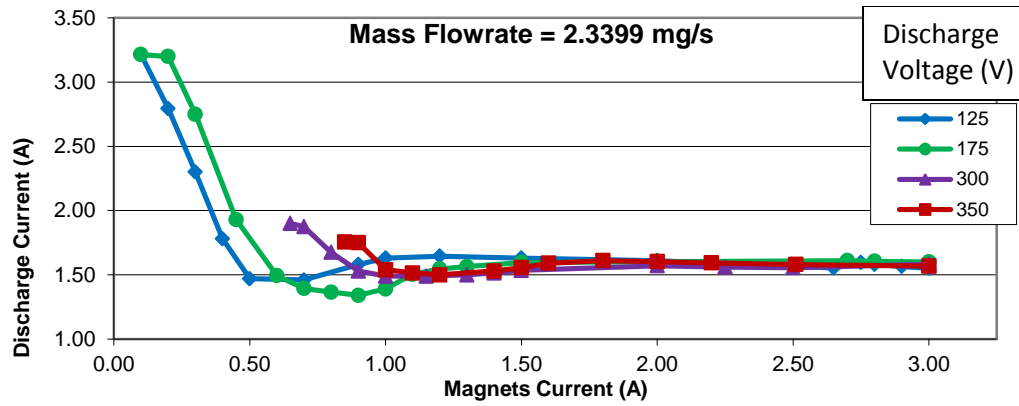
#### *B. Both Magnets Effects on V-I Curve*

The BHT-600W thruster is different from BHT-200W because it has two independently powered electromagnet coils; the outer and inner coils. The four outer coils are wired in series while the inner core is a single coil. This design generates magnetic fields with a sharp drop near the anode [49]. This research examined various magnet setting effects on the thruster performance such as connecting the inner and outer magnets in series or each with their own independent power source. The inner and outer magnets currents were varied from 0-3.0A for different propellant flow rates and discharge voltages. This research only looked at maximum magnet currents of 3.0A because applying higher amperages might burn the magnet coils and cause damage to the thruster.

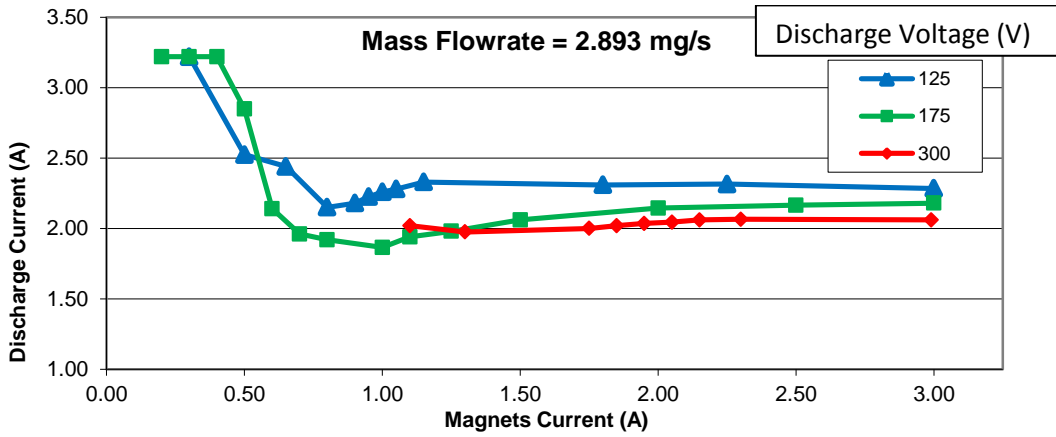


The experiment determined that discharge current was dependent on both inner and outer magnetic fields. Testing shows at high magnet currents, discharge current remained fairly constant. However, as the magnet currents decreased, discharge current decreased to a nominal point and then started to make a transition into current limit mode. The results are plotted in Figure 35 for various propellant flow rates and discharge voltages.

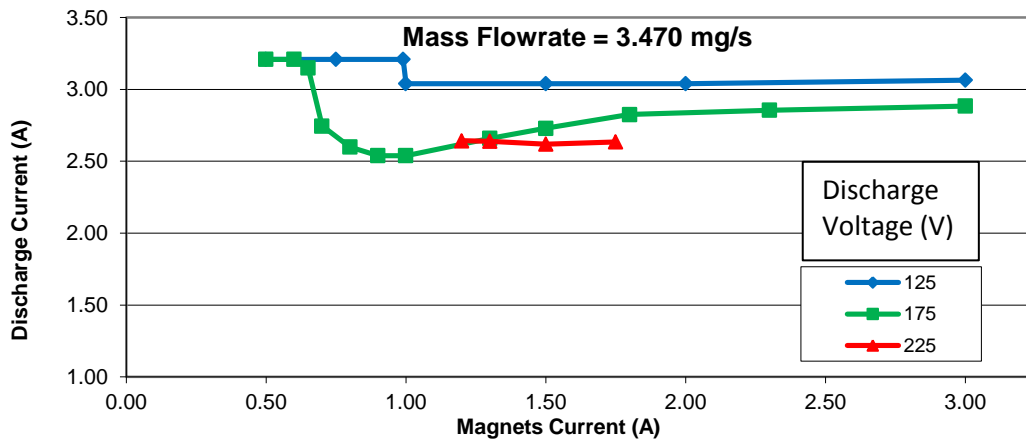
The plots below further confirmed results from the V-I curve analysis. At low mass flow rates (plot a), the discharge current remained almost the same for different discharge voltages. At high mass flow rates (plot c), the discharge currents were lower for high discharge voltage. The dip in discharge currents around 1.0A – 1.75A was the nominal point of the magnet current setting because that point corresponds to minimal discharge power. Plot (a) shows the nominal point shifted from lower to higher magnet current as discharge voltages increased. A similar trend was observed for higher mass flow rates with high discharge voltage, presented in plot (b) and (c). However, at low discharge voltage and high mass flow rates regions, the thruster can easily make a transition into current limit mode more abruptly, without any indication, as illustrated by the blue line in plot (c). The discharge voltages of 225V in plot (c) seem to operate only from 1.2A to 1.75A because of missing data points rather than thruster design. It is reasonable to assume that same line (red) in plot (c) would follow the same trend in plot (b) if there were more data points.



(a)



(b)



(c)

Figure 35: Discharge current effects from inner and outer magnet currents.

It must be noted that the analysis above was for the inner and outer magnets connected to independent power supplies. Each of the magnet coils' powers were supplied by separate Hewlett Packard 6033A system power supplies. Attempts were made to keep both magnets' currents closely matched. Therefore, this research also looked at the thruster performance when both inner and outer magnets were connected in series. The analysis concluded that the thruster performed the same with either both magnets connected in series or with their respective independent power supplies. The results are shown in Figure 36.

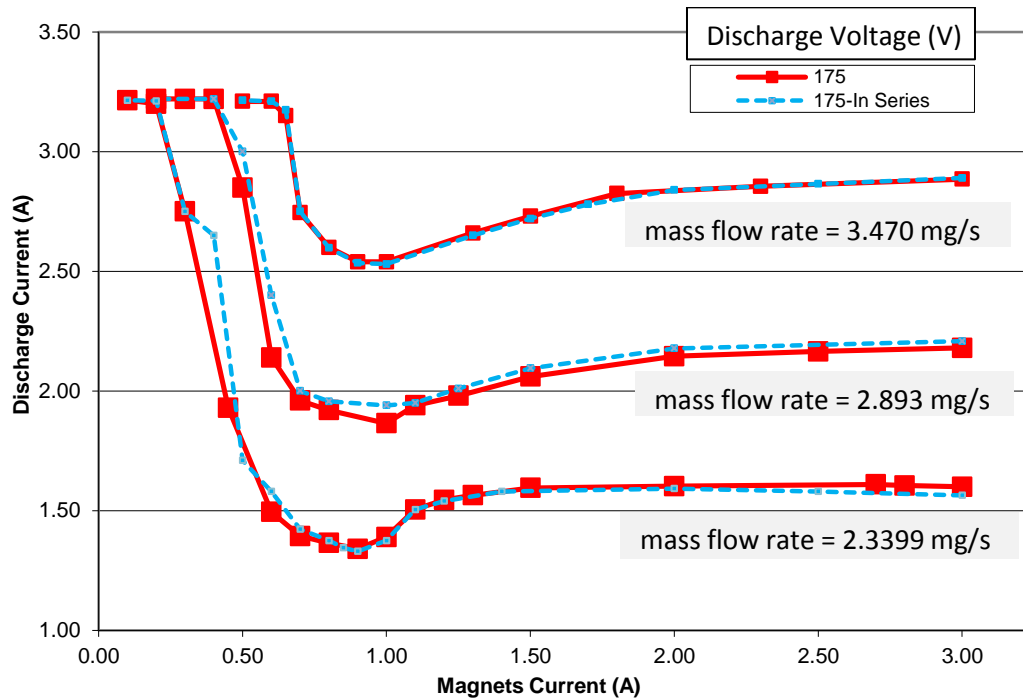


Figure 36: Discharge current responses to magnets connected in series or to independent power supplies.

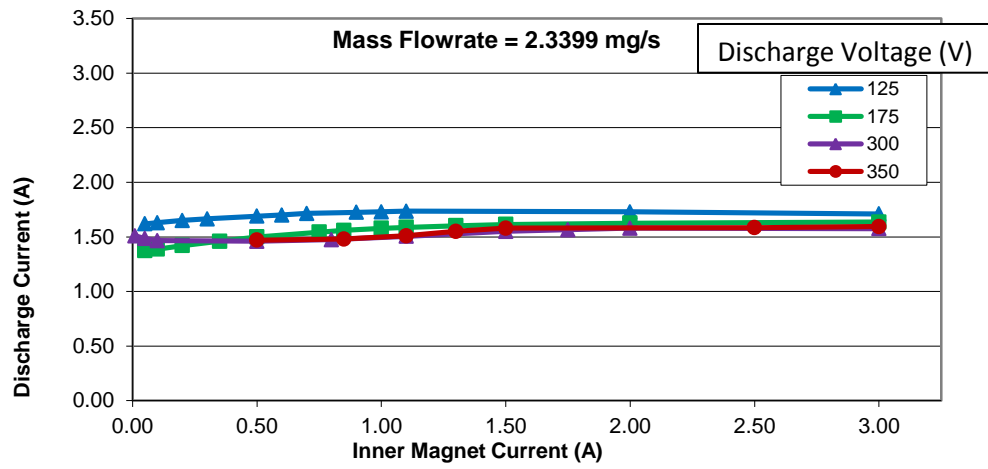
The figure above plots discharge current as a function of magnets current for three different mass flow rate operating at discharge voltage of 175V. The plot shows discharge currents are practically the same. It does not matter how the magnets are wired together, as long as proper amperage is applied to the thruster, its performance should be the same. Few differences in the plot were observed. It was assumed the sources of differences were most likely instrumentation and thermal effects on magnet coils.

The next experiment examined the behavior of the thruster when varying one magnet coil while keeping the other constant. This information can be useful for situation where the end-user lost the ability to control one of the magnet currents. This part evaluated the effects on discharge current for various *inner* magnet coil settings while keeping *outer* magnet current constant at 1.75A. The experiment also looked at performance for various discharge voltages at three different mass flow rates. The results from inner magnet current setting changes are shown in Figure 37.

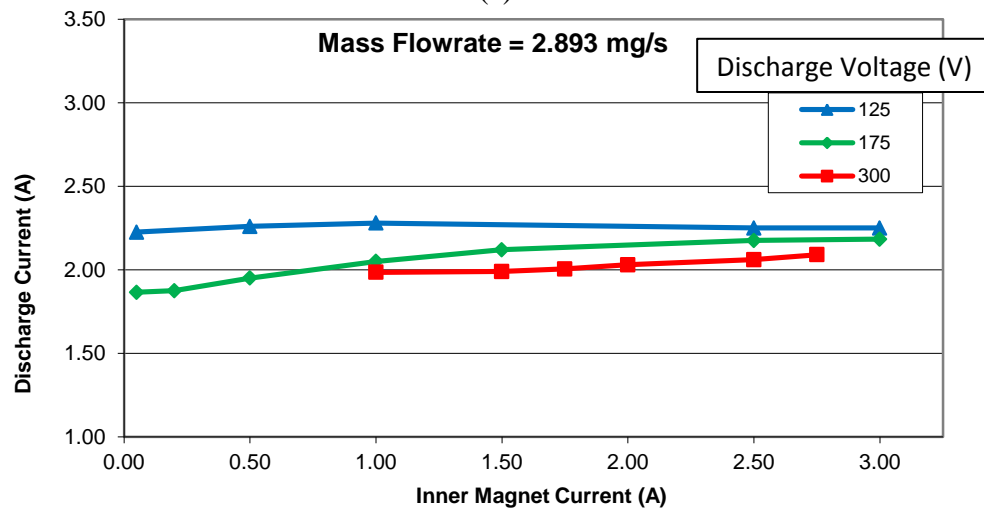
All the plots in Figure 37 showed the effects of *inner* magnet coil on discharge current are minimal. The most noticeable was in plot (a). At low mass flow rates, the discharge current remained constant for various *inner* magnet settings at three discharge voltages. It was observed that at discharge voltage of 175V (green line), the *inner* magnet coil settings had the most effect on discharge current. The discharge current increased for *inner* magnet currents from 0A-1.75A, but remains constant for *inner* magnet currents higher than 1.75A. However, the changes remained minimal. Plot (b) also indicated that adjusting *inner* magnet current has no effect on discharge current for all three discharge voltages. The V-I curve showed that conditions at high mass flow rate

and low discharge voltages were prone to make transition into current limit mode. Not surprisingly, the results from plot (c) validated such finding (blue line). The thruster entered current limit mode as the inner magnet decreased to 1.0A.

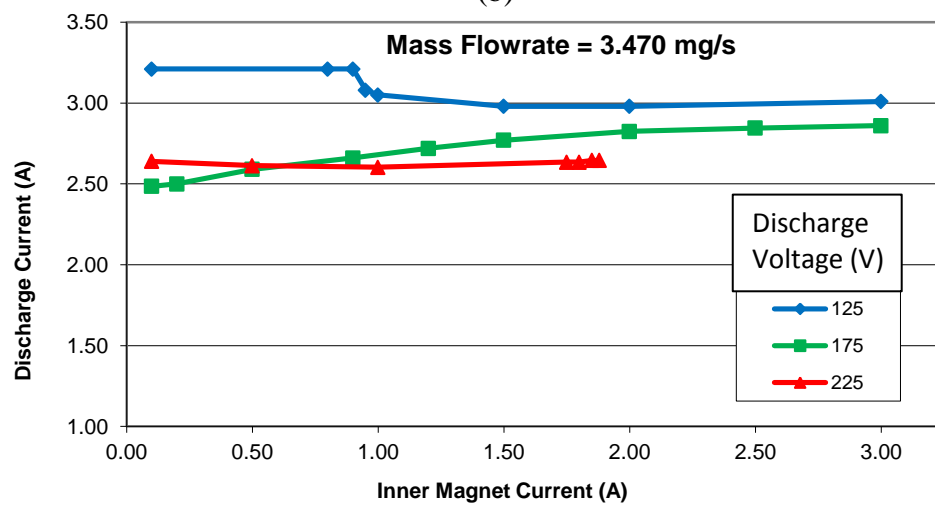
The next study assessed the behaviors of the thruster by varying *outer* magnet coil current while kept the *inner* magnet coil at 1.75A. As before, the experiment examined the performance for various discharge voltages at three different mass flow rates. The results from outer magnet current settings are shown in Figure 38. The thruster performance was almost identical to the previous situation, where varying the *inner* magnet coil while keeping the *outer* coils constant at 1.75A. As shown in plot (a), at low mass flow rates, the *outer* magnet settings had almost no effect on discharge current for various discharge voltages. A similar trend was observed for higher mass flow rates as illustrated in plot (b) and (c). As in the above analysis, only a discharge voltage of 175V produced an increase in discharge current with increasing *outer* magnet currents. Again, decreasing *outer* magnet current caused the thruster to enter current limit mode for condition with high mass flow rates and low discharge voltages (blue line in plot c).



(a)

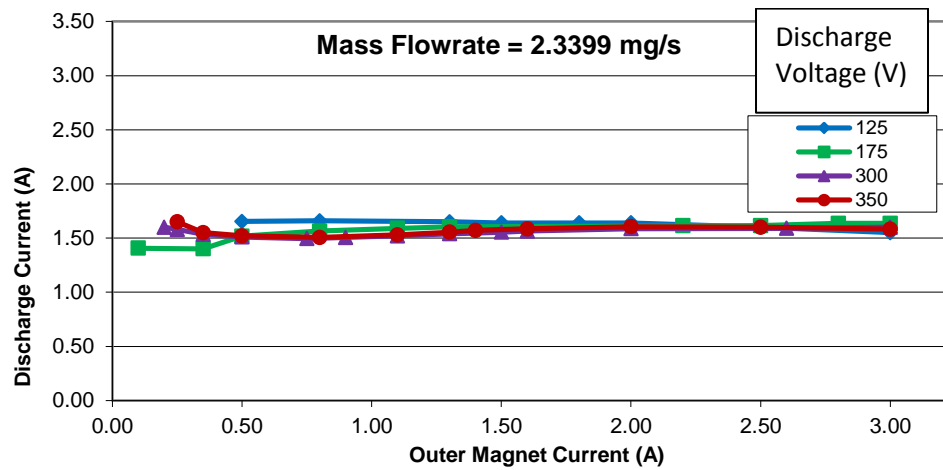


(b)

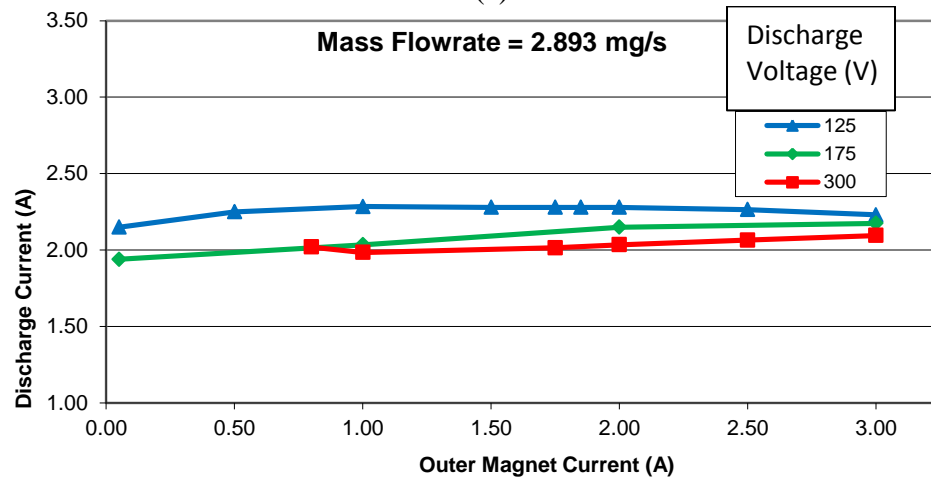


(c)

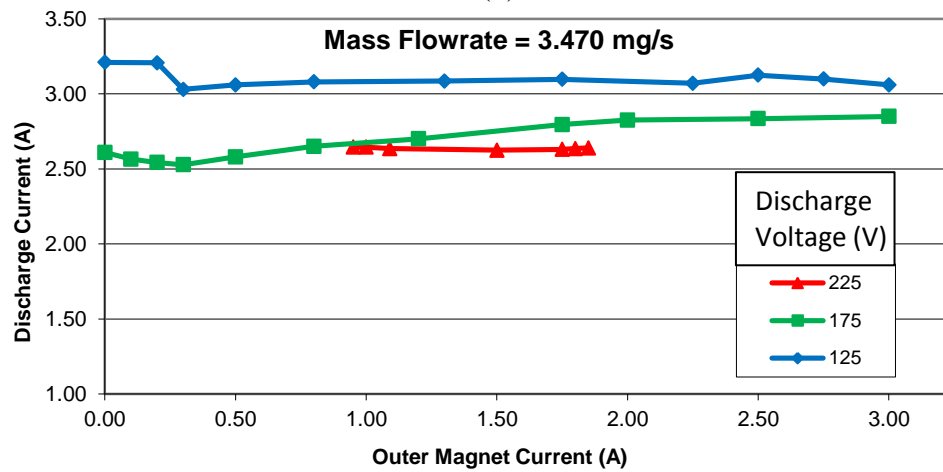
Figure 37: Inner magnet currents effect on discharge current.



(a)



(b)



(c)

Figure 38: Outer magnet currents effect on discharge current.

### IV.3 Thrust Measurement

Thrust was measured directly using a Busek T8 inverted pendulum thrust stand. As expected, the characteristics of BHT-600W were similar to other Hall thrusters such as BHT-200W. However, BHT-600W performance in terms of thrust and Isp was obviously higher than BHT-200W because it was designed to operate at higher power. The BHT-600W's thrust profile was measured for various discharge voltages as well as at different mass flow rates. Other performance parameters (i.e. Isp and propulsive efficiency) were calculated directly from measured thrusts and other parameters by using Figure 18 and 20 below. In addition to discharge voltage and anode propellant mass flow rate, the experiment also looked at thruster performance as a function of various magnetic field settings.

$$Isp = \frac{T}{\dot{m}g_0} \quad (18)$$

$$\eta_T = \frac{T^2}{2\dot{m}_p P_{in}} \quad (20)$$

#### A. BHT-200W

The research started out by taking measurements from BHT-200W. It was used as a baseline for this research because it has extensive heritage. The tests performed on BHT-200W were at its nominal operating condition. The results were used to validate the experiment equipment and methods. The BHT-200W produced 12.7 mN of thrust, 1418



sec of Isp, and a propulsive efficiency of 44.7%. These results were in good agreement with values reported by Busek and other researchers therefore provided a good baseline and validation for experimentation on BHT-600W [46, 51]. The operating parameters for BHT-200W are presented below.

Table 3: BHT-200W nominal performance parameters.

Discharge Voltage	248V
Discharge Current	0.8A
Cathode mass flow rate	0.065 mg/sec
Anode mass flow rate	0.850 mg/sec
Magnet Current	0.99A
Measured Thrust	12.7 mN
Specific Impulse	1418 sec
Efficiency	44.7 %

#### *B. BHT-600W's Performance*

One of the main objectives of this research was to determine the thrust of the BHT-600W. Thrust is a very important fundamental parameter because it enabled the researcher to quantify the specific impulse and propulsive efficiency. With analysis from the V-I curve discussed earlier, this research measured thrust for most of the BHT-600W operating conditions. The experiment started out by measuring thrust at its nominal condition. The results were compared to values cited by Busek Co. as presented in Table 4. The measured thrust from this experiment was lower but close to those values reported by Busek. These differences were expected and are assumed to be contributed by many factors such as different equipment, conditions, setup, time, etc. This research then examined other potential conditions the thruster may operate in.

Table 4: BHT-600W nominal performance parameters.

	Busek Co.	Experimental
Discharge Voltage	300V	300V
Discharge Current	2.0A	2.0A
Anode mass flow rate	2.5 mg/sec	2.66 mg/sec
Cathode mass flow rate	0.15 mg/sec	0.146 mg/sec
Magnets Current	1.75 A	1.75 A
Measured Thrust	42 mN	34.8±1.3 mN
Specific Impulse	1,585 sec	1,267±39 sec
Efficiency	55.4 %	36.2±2.4 %

Thrust was measured at five different mass flow rates while varying discharge voltage from 60V to 400V. Five mass flow rates were chosen ranging from minimum of 1.887 mg/s to maximum of 3.354 mg/s. This research only measured thruster performance for discharge power from 0-625 W even though it has the ability to reach 800W. As discussed earlier, this research was limited to maximum 625W due to the limitations of the power supply. The measured thrust for different conditions is presented in Figure 39. The plots show thrust as function of discharge power at six mass flow rates. Overall, the plot revealed a monotonic relationship between thrust and discharge power. It seems this relationship may apply to discharge powers higher than 625W. However, more data points are needed to validate such an assumption. Additionally, thrust was about the same for different mass flow rates. However, at discharge powers of 425W and higher, thrust started to diverge and became more prominent for different mass flow rates. High mass flow rates seem to produce more thrust than lower mass flow rates. This was expected because discharge current was used to calculate discharge power.

Extrapolating the data in Figure 39 reveals that thrust could possibly be as high as 55mN if discharge power were to increase to 800W. This research was constrained by time and was unable to investigate at that higher power.

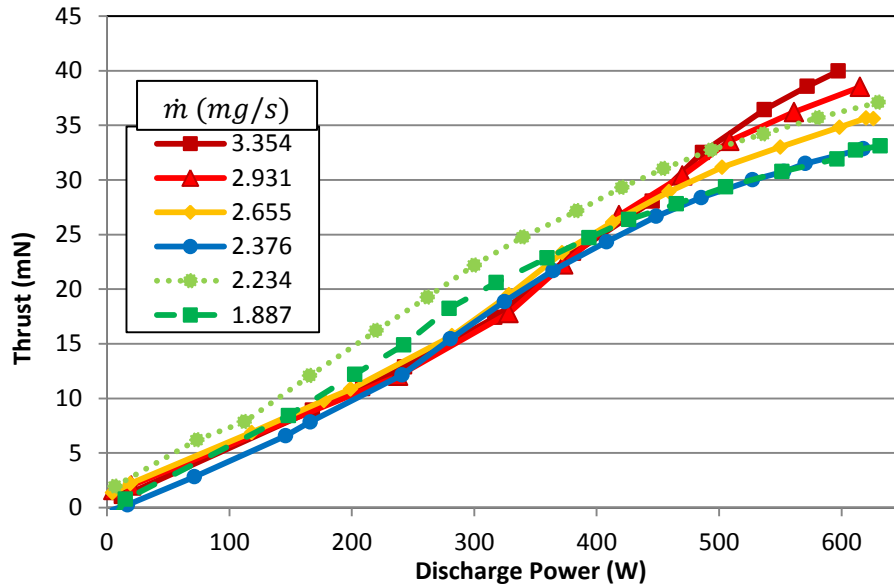


Figure 39: Thrust measured at various discharge power and mass flow rates.

Thrust also enabled calculation of specific impulse,  $I_{sp}$  according to Equation 18. Specific impulse is important because it allows the designer to choose the most efficient operating point for the system. The  $I_{sp}$  for BHT-600W at various operating conditions as discussed above is plotted in Figure 40. The plot shows that  $I_{sp}$  monotonically increased as discharge power increased. The trend was in agreement with Equation 18 because  $I_{sp}$  is directly related to measured thrust. However, the  $I_{sp}$  settled off to some value at high discharge powers. This indicated that there was a maximum point or diminishing point of return for  $I_{sp}$  as discharge power increases. The result also indicated higher  $I_{sp}$  was obtained for lower mass flow rates while the opposite was true for higher mass flow rates. The BHT-600W was predicted to produce such results.

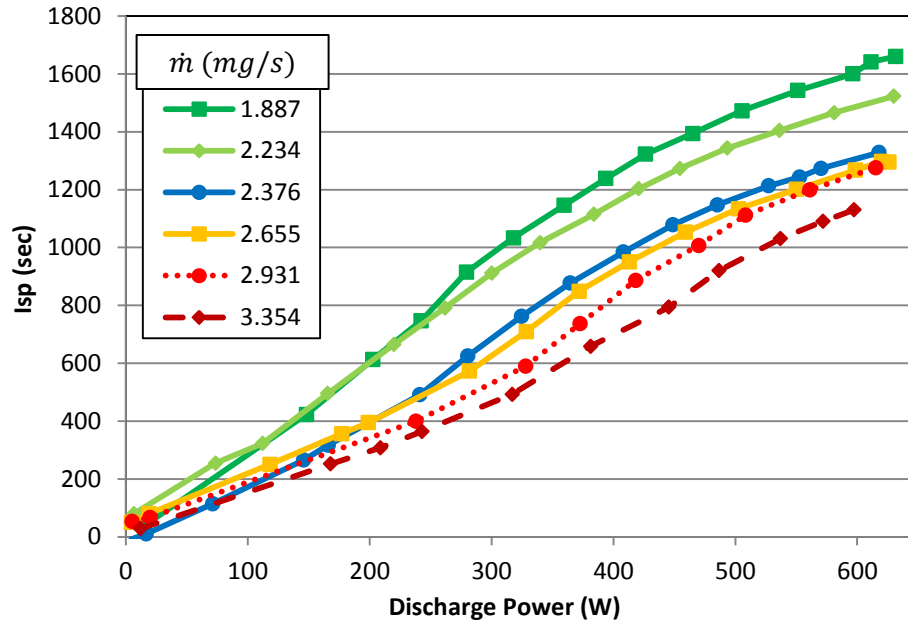


Figure 40: Isp at various discharge power and mass flow rates.

Propulsive efficiency is another important thruster parameter calculated from the thrust measurement. This value relates the thruster's output power to its discharge input power. It is a very useful parameter because it can be used to compare performance with other type of thrusters. Equation 19 was used to calculate the efficiency. The overall propulsive efficiency for BHT-600 at various discharge power for different mass flow rates is presented in Figure 41. The thruster's efficiency increased as discharge power increases. However, propulsive efficiency reached its maximum point around 600W. This corresponds to the nominal discharge power reported from Busek. This paper can only hypothesize that efficiency would decrease for discharger power higher than 600W, therefore more data is needed. The effects on efficiency due to mass flow rates were not as evident as discharge power. From Figure 41, it looks like there is no linear relationship between mass flow rates and efficiency. The data revealed that the most efficient mass

flow rate for BHT-600W is at 2.234 mg/sec. This finding is believed to be incorrect because the data for lower mass flow rate of 1.887 mg/sec and 2.234 mg/sec was taken at different dates and is therefore most likely to produce an unreliable result. If the two lower mass flow rates were disregarded, a more reasonable one seems to be 2.931 mg/sec. This mass flow rate is most efficient and close to matching with the value from Busek.

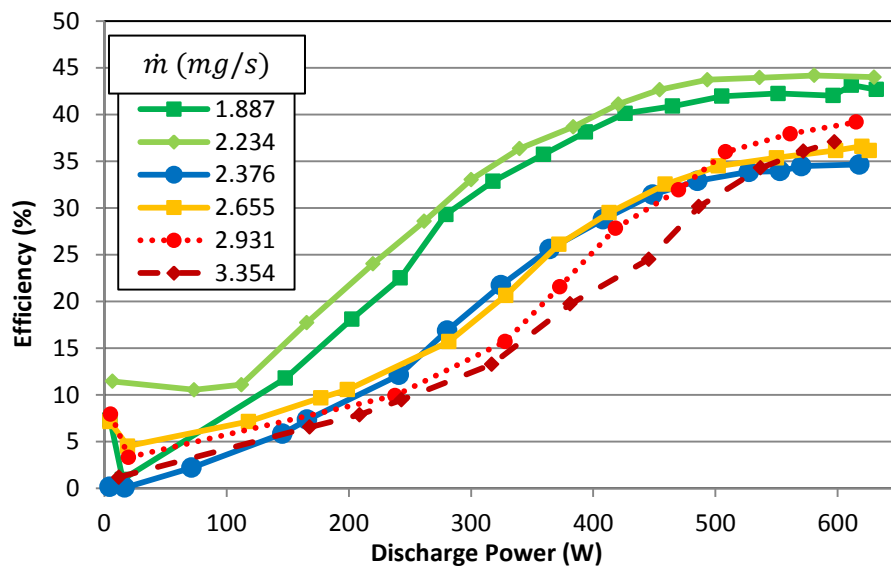


Figure 41: Propulsive efficiency at various discharge power and mass flow rates

Analysis of the thruster performance for different mass flow rates yielded imprecise results, most likely because of errors in the experimental setup, especially at mass flow rates of 1.887 mg/sec and 2.234 mg/sec,. The data from thrust measurements was gathered from various test runs on different dates which is believed to contribute to disagreement in the results. The thruster does not operate the same after being turned off or after the vacuum seal was broken to recalibrate the instrument. Additionally, Busek's T8 inverted pendulum stand is believed to provide inaccurate measurements due to

thermal drift, weight limits, and inclination of the instrument. As illustrated by Figure 42, heat from the thruster caused the readings to deviate from its real value. The experimental set up has a water cooling system to reduce this error source but could not completely eliminate it. Thermal drift was observed highest when the thruster operated at 600W and higher or 200W and lower. The heat transfer was greatest at these two extreme conditions and the cooling system was unable to compensate such a thermal flux.

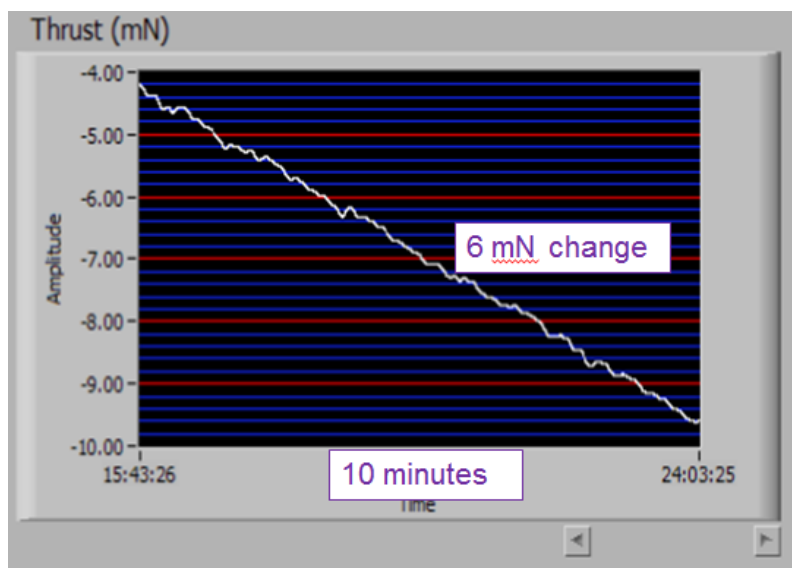


Figure 42: Thermal drift effect on thrust measurement.

The thrust measurement was also affected by the stand inclination changes over time. The user needs to manually adjust it back to zero inclination during each test run but small amount of error would always still be there. Additionally, the BHT-600W was at the weight limits of the flexures that secured the thruster to the thrust stand. The thruster was nearly too heavy and sometimes caused the flexures to buckle. In addition to thermal flux, too much weight on the flexures may induce errors in the measurements.

### C. Both Magnet Coils Effects on Thruster's Performance

This research also looked at the thruster performance from the effects of magnet currents. Both inner and outer magnet coils were connected to their respective independent power supplies. Thrust was measured for various magnet currents from 0A-3.0A at different operating conditions. The conditions BHT-600W operated were from 3.311 mg/sec to 2.077 mg/sec while setting the discharge voltage at 300V, 225V, 175V, and 125V. These operating points are illustrated by the purple diamonds from Figure 43.

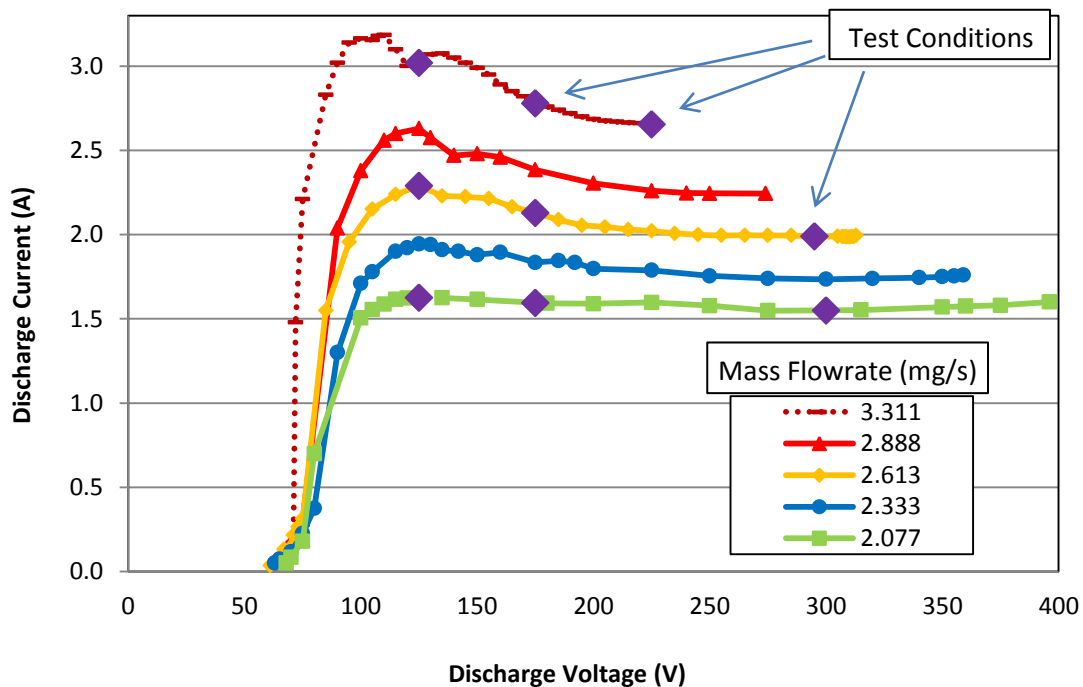


Figure 43: Operating points tested for magnet coils effects on thruster performance.

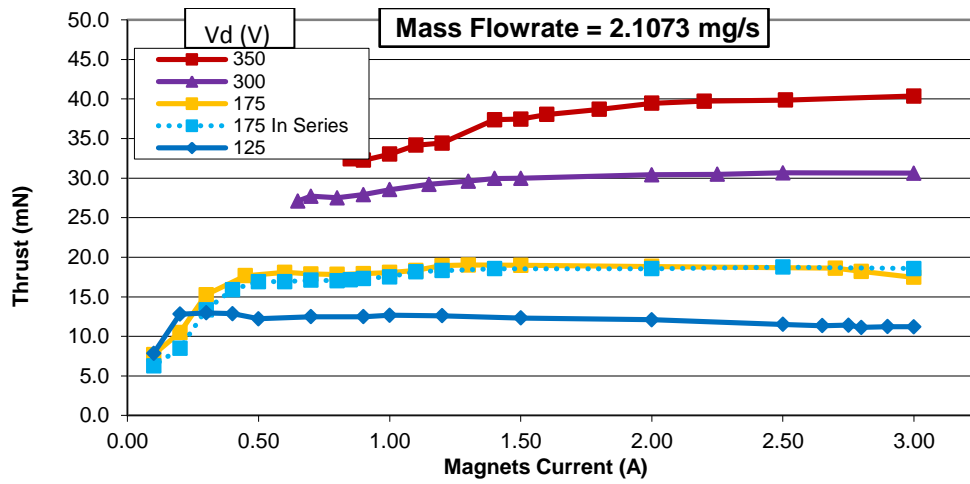
The effects of magnet current on thrust are presented in Figure 44. Overall, the results indicate that measured thrust remained fairly constant for magnet currents greater than 1.0A. A small change in thrust for magnet currents from 1.0A-3.0A was most likely due to errors in measurement from thermal drift on the instrument. Adjusting magnet

current would not affect BHT-600W performance except for few exceptions. At a low mass flow rate of 2.1073 mg/sec, increasing the magnet current would increase thrust by almost 10mN. However, such a trend was not observed at the higher mass flow rate of 3.3537 mg/sec. Plot (a) and (b) indicate thrust would drop drastically for magnet currents lower than 0.5A. The reduction in thrust was due to the thruster making a transition to current limit mode. This result corresponds to the analysis from the V-I curve. The same was observed for higher mass flow rate in plot (c). The reduction in thrust occurred at higher magnet current and has a sharper drop because higher mass flow rates and low discharge voltages are closer to current limit mode boundary.

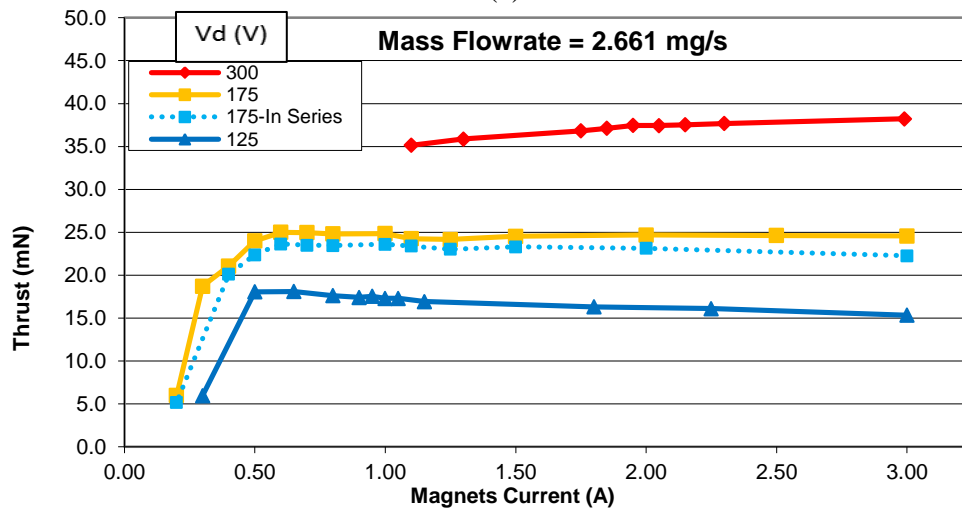
The blue lines in Figure 44 represent when inner and outer magnet coils were connected in series instead of their own independent power supplies. The results show that the thruster performance was the same and does not relate to the way each magnet coils is connected. This further confirmed the finding from VI analysis section that magnet coils needs to connect to different power supply. This gives the user greater control over the thruster.

The effects of magnet current on thruster efficiency followed the same trend as measured thrust. This was expected because thrust and efficiency are linearly related, given by Equation 20. The results are shown in Figure 45. Efficiency dropped drastically for magnet currents less than 1.0A due to thruster transition into current limit mode. However, it remains constant for magnet currents greater than 1.0A. The effects of the magnets on efficiency are more prominent at higher discharge voltages. Plot (a) and (b) revealed efficiency increased as magnet current increased.

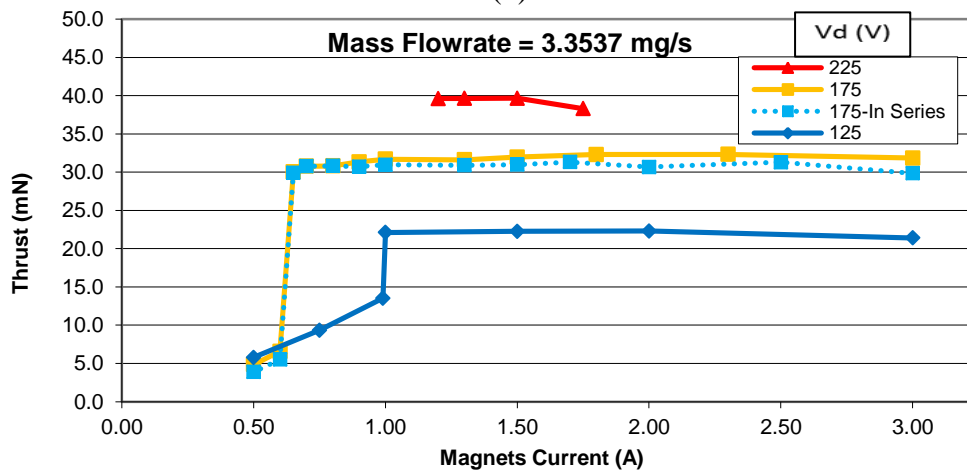




(a)



(b)



(c)

Figure 44: Magnets effect on thrust for various  $V_d$  and mass flow rates.

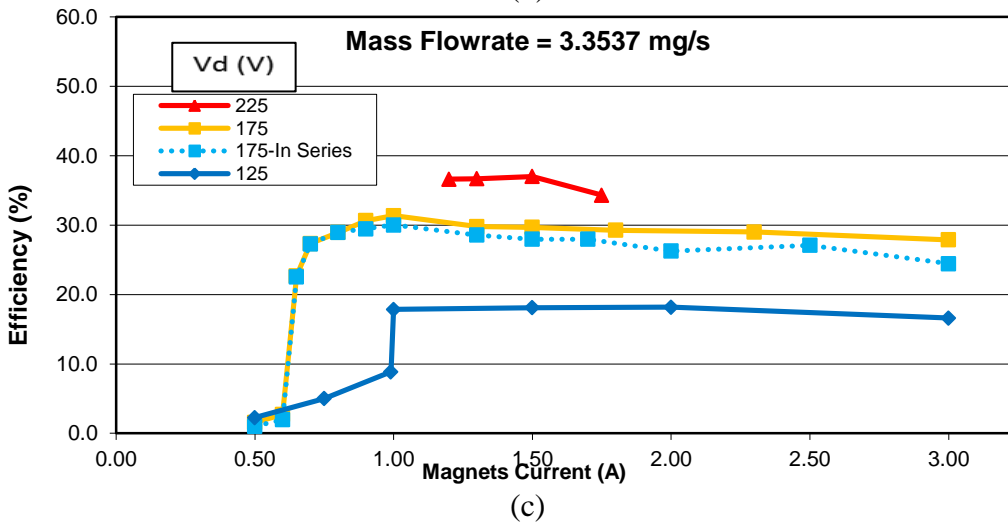
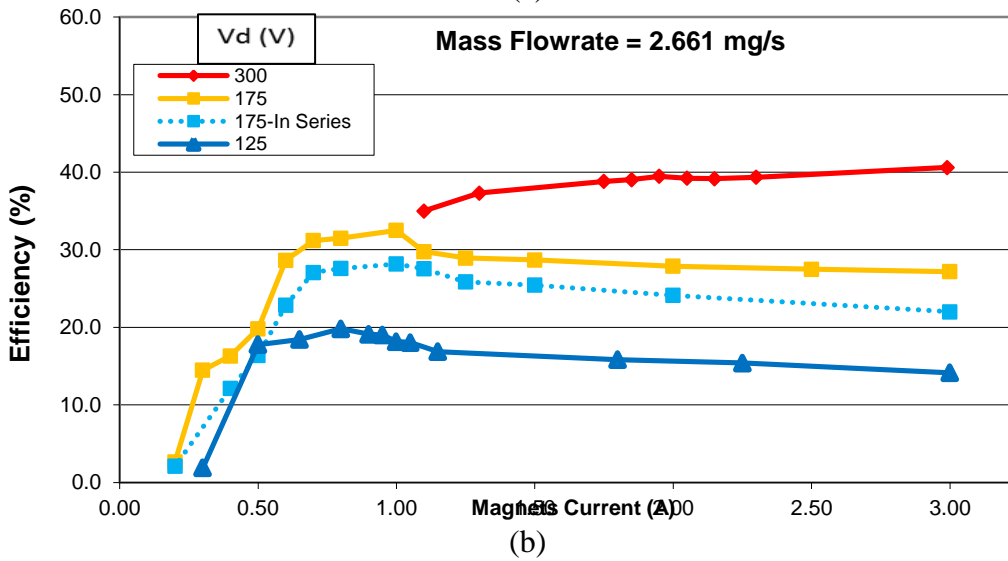
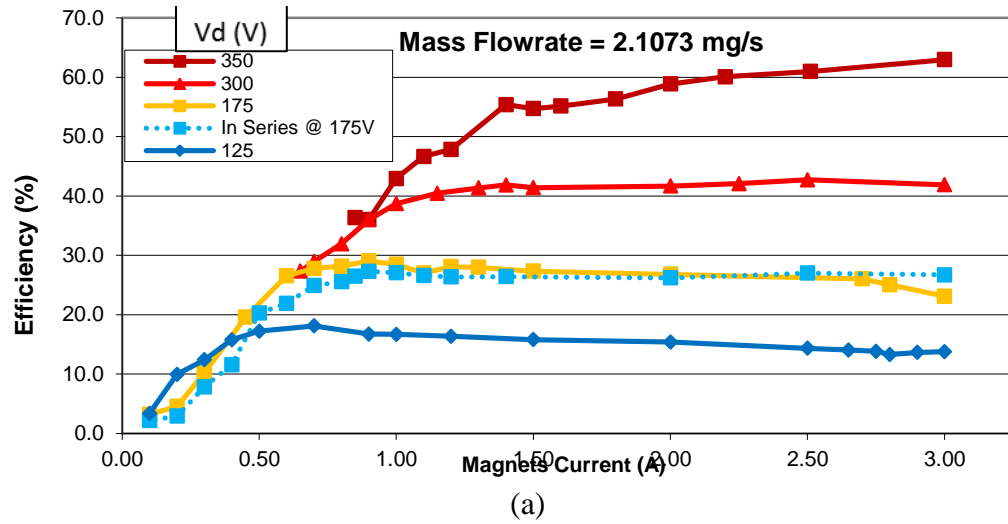
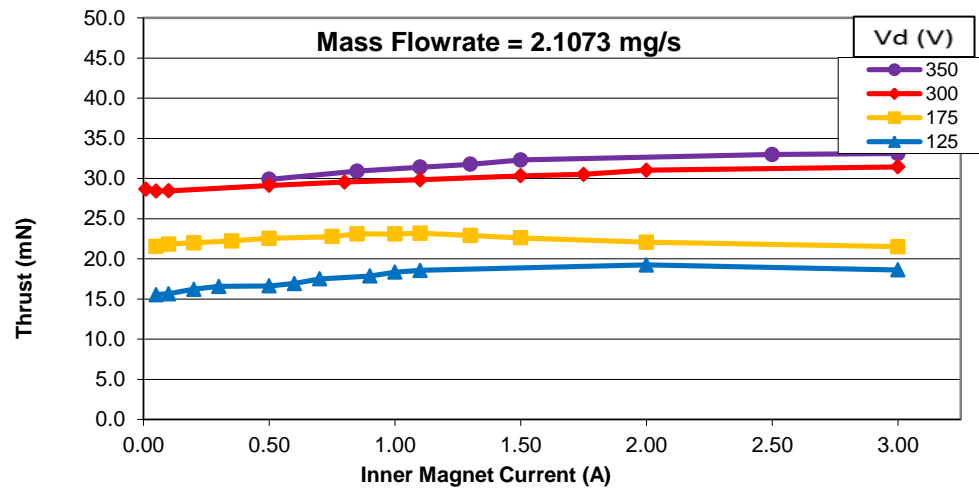


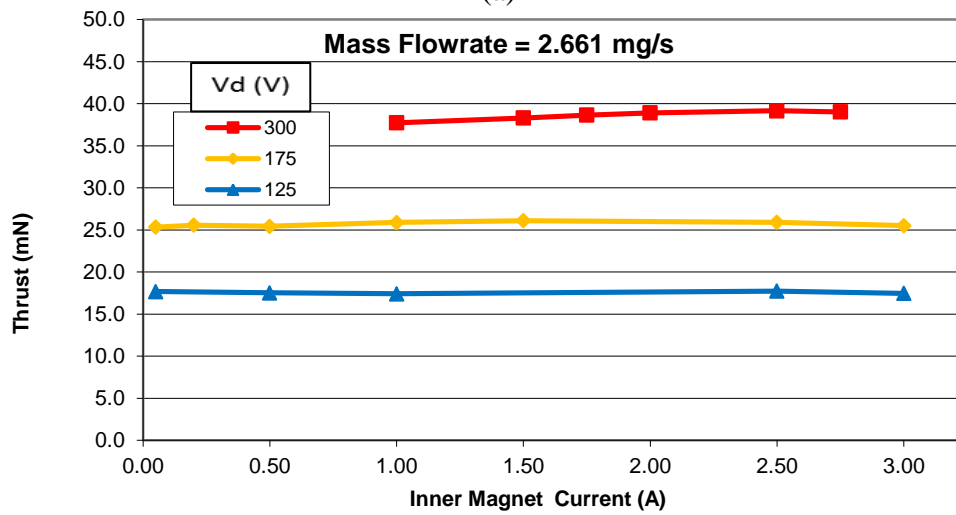
Figure 45: Inner magnet effect on efficiency for various operating conditions.

#### *D. Inner Magnet Effects on Thruster's Performance*

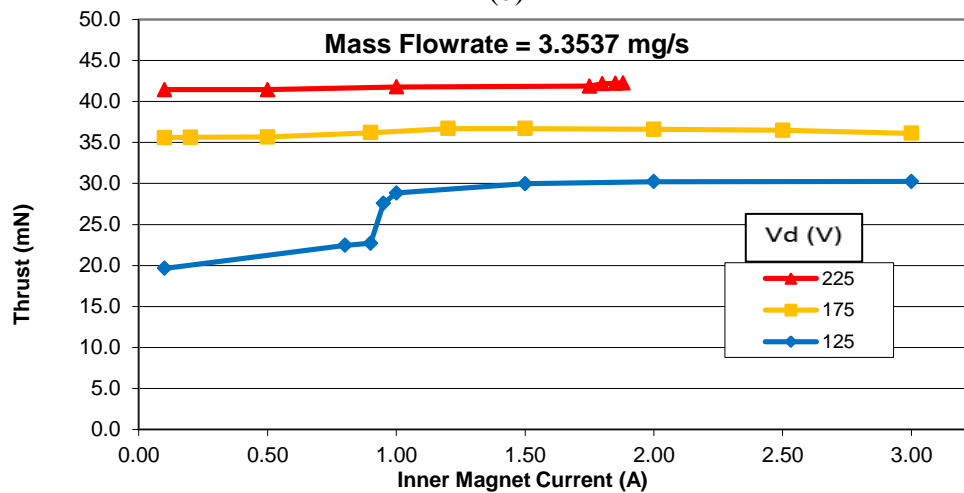
The above analysis was for both *inner* and *outer* magnet coils set to the same current when each was connected to an independent power supply. This research also studied the effects of the magnets on the thruster performance as one magnet coil remains at 1.75A while the other varied from 0-3.0A. The following results are for the condition where the *outer* magnet coils were constrained to 1.75A while the *inner* coil varied from 0-3.0A. Measurements were taken at three mass flow rates while varying three discharge voltages for each. The test conditions are better illustrated in Figure 43, represented by purple diamonds. The results of *inner* magnet current effects on thrust are present in Figure 46. Analysis of all three plots revealed that thrust remains constant for different *inner* magnet currents at all six operating conditions. There are cases where it increased by a few millinewtons, which was most likely caused by thermal drift in the instrument. However, for a mass flow rate of 3.3537 mg/sec and a discharge voltage of 125V in plot (c), the thrust dropped from 28.8mN down to 22.7mN for the *inner* magnet current of 1.0A. Again, this drop in thrust was due to a transition to current limit mode. Thrust stayed at 20mN and did not drop all the way to zero for current of 0.1A due to the *outer* magnet. The 1.75A current from *outer* magnet kept thruster from shutting down.



(a)



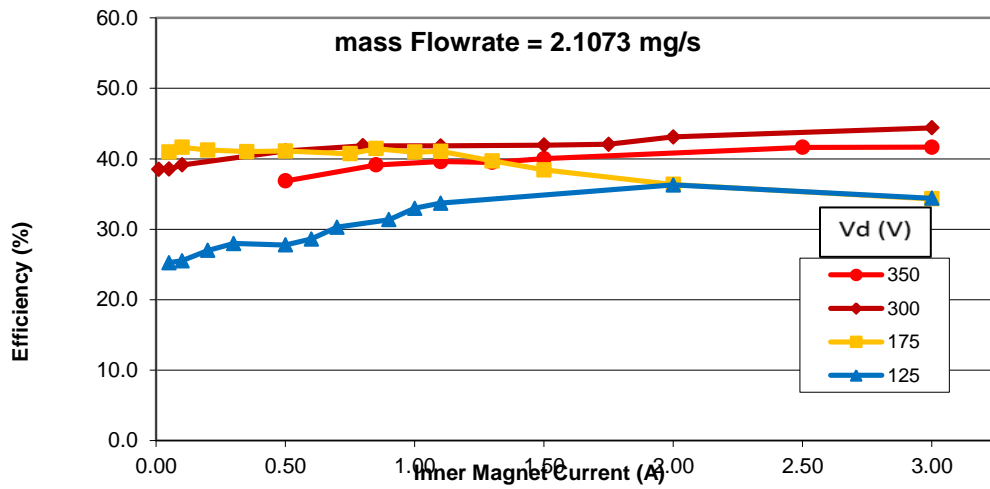
(b)



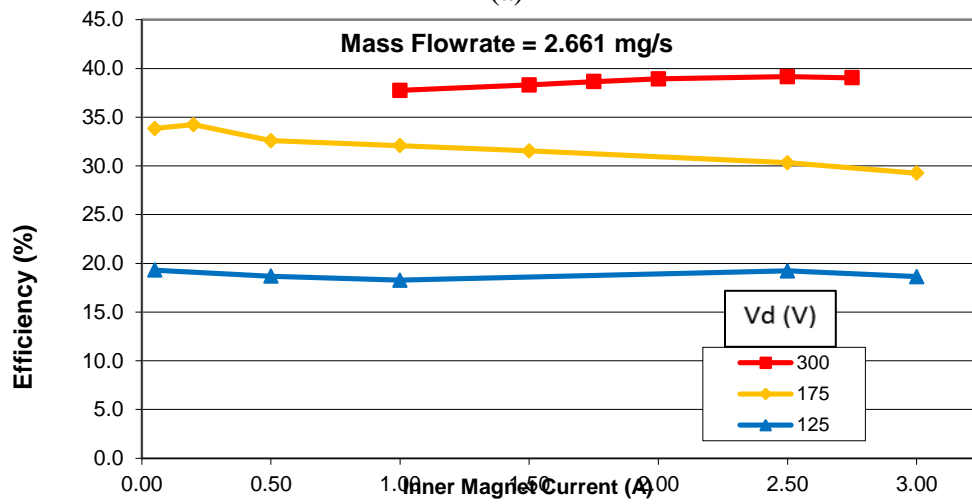
(c)

Figure 46: Inner magnet effect on Thrust for various operating conditions.

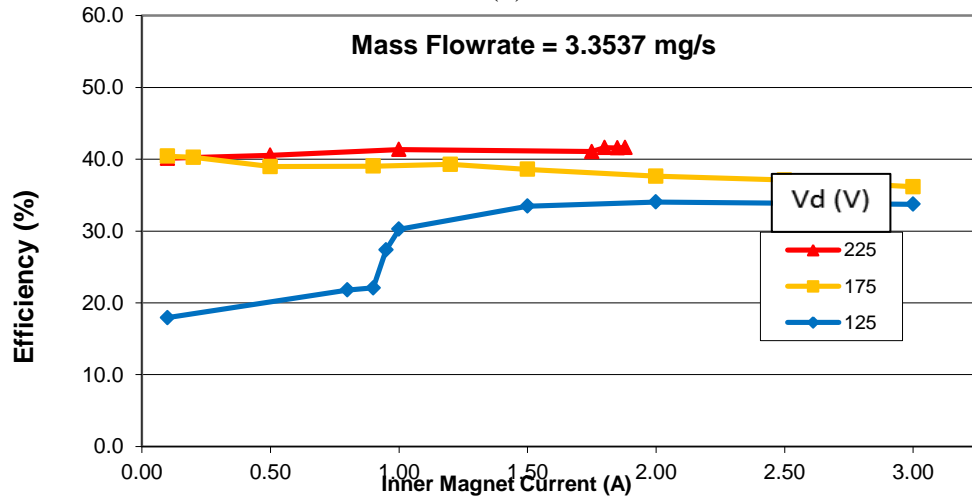
The effects on thruster efficiency were also calculated for different inner magnet current settings at the same six operating conditions as discussed above. The calculated efficiency from thrust as a function of *inner* magnet currents for various mass flow rates and discharge voltages are presented in Figure 47. The overall trend is that efficiency remains the same for different inner magnet currents, especially for a mass flow rate of 2.661 mg/s. At the higher mass flow rate of 3.3537mg/sec, the same drop in thrust at current 1.0A corresponds to the same reduction in efficiency. As discussed before, this was due to the thruster transiting into current limit mode. However, plot (a) showed that efficiency is greatly affected by *inner* magnet current at low mass flow rate and low discharge voltages. It was mainly caused by reduction in discharge current. As discussed in V-I curve section, at 125V discharge voltage and 2.1073 mg/sec, the thruster operated at a boundary condition where discharge current could drastically drop to zero or low discharge current mode. Therefore the magnet current has great influence over this region.



(a)



(b)

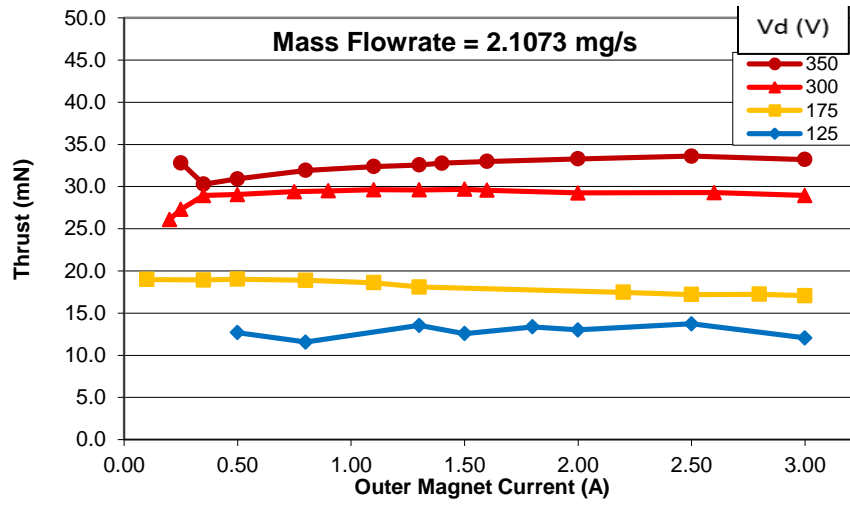


(c)

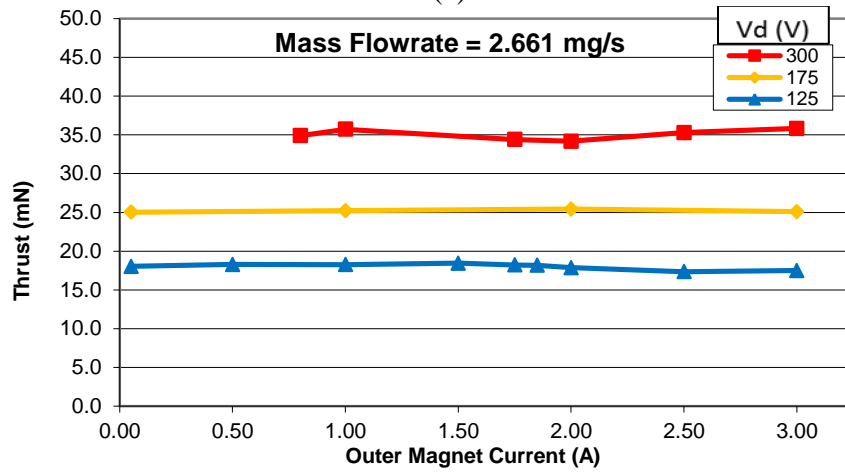
Figure 47: Inner magnet effect on efficiency for various operating conditions.

### *E. Outer Magnet Effects on Thruster's Performance*

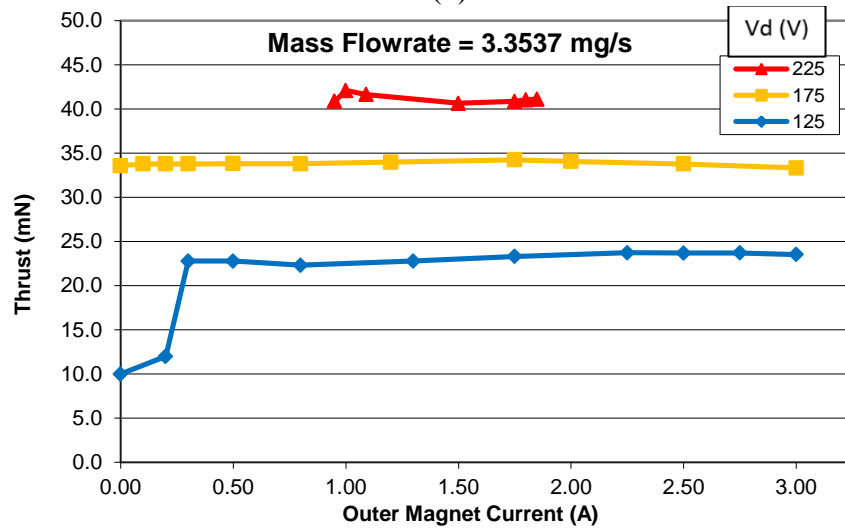
The following results are for conditions where the *inner* magnet coils were constrained to 1.75A while the *outer* coil varied from 0-3.0A. Similar to above, measurements were taken at the same three mass flow rates while varying three discharge voltages for each. The results of *outer* magnet current effects on thrust are present in Figure 48 below. The overall effects on thrust by the *outer* magnet current are the same as *inner* magnet current. Thrust remains constant for various *outer* magnet currents at different mass flow rates and discharge voltages for most cases. Plot (a) shows that thrust changed for an *outer* magnet current lower than 0.35A for 300V and 350V discharge voltages and 2.1073 mg/s. This was most likely caused by instability mode of the thruster. As seen from V-I curve analysis, high discharge current fluctuations were found for low mass flow rates and high discharge voltages, a sign of instability. As expected in plot (c), at the higher mass flow rate 3.3537mg/sec, the thrust dropped at current 0.3A due to transition into current limit mode. This transition was at lower amperage than before where it was at 1.0A for the *inner* magnet. This result affirms that the *outer* magnet current can operate in a larger range than *inner* magnet current.



(a)



(b)

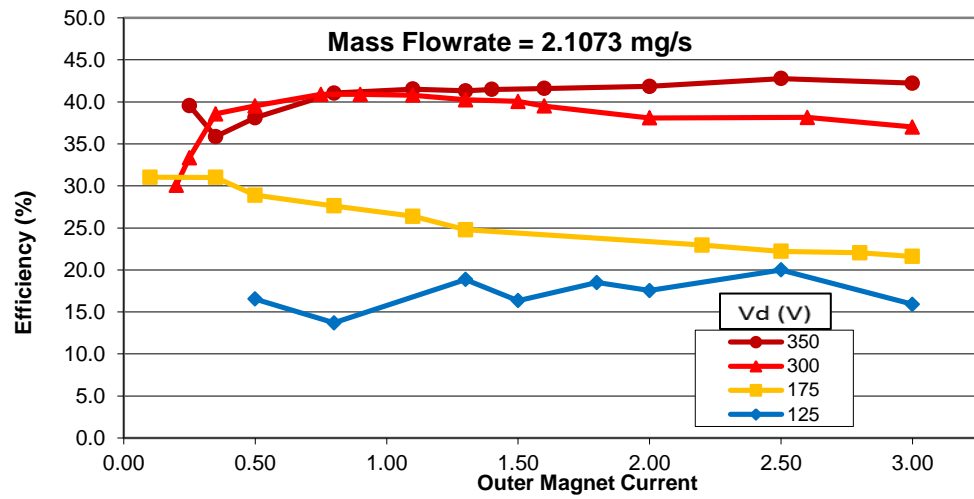


(c)

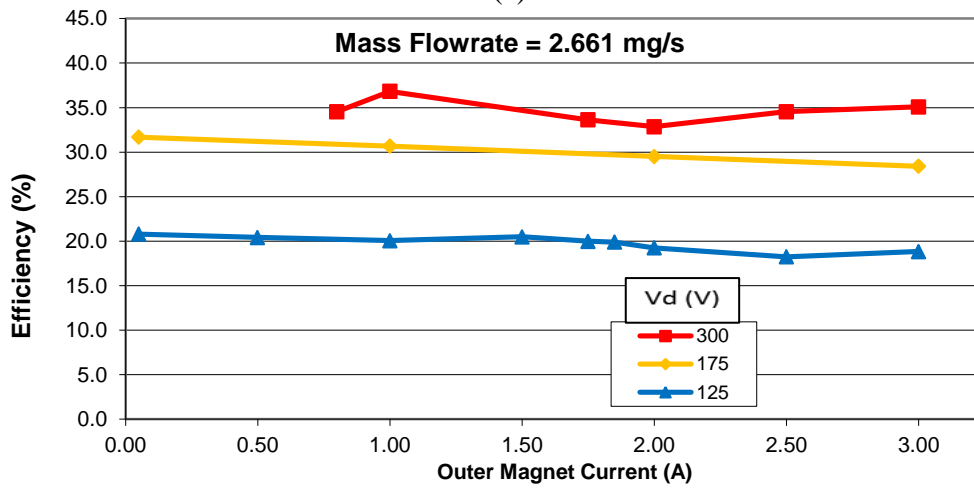
Figure 48: Outer magnet effect on thrust for various operating conditions.



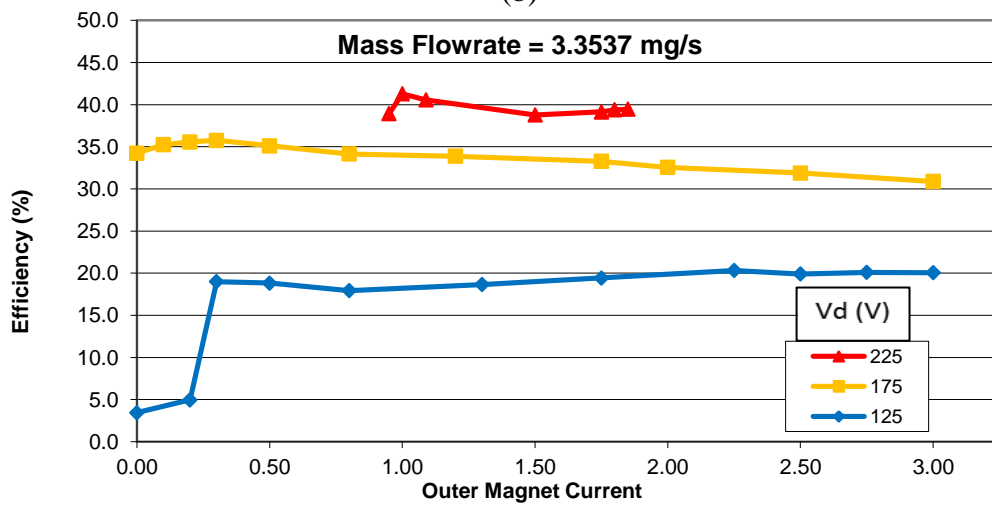
The calculated efficiency from thrust as a function of *outer* magnet currents for various mass flow rates and discharge voltages is presented in Figure 49 below. The same overall trend was seen before from the effects of the *inner* magnet currents. The efficiency remains almost constant as the *outer* magnet current varies from 0-3.0A for different operating conditions. Similarly, at the higher mass flow rate of 3.3537mg/sec, a drop in efficiency corresponds to same drop in thrust as discussed previously. For the lower mass flow rate 2.1073 mg/s from plot (a), efficiency no longer remains constant. At discharge voltages of 300V and 350V, the efficiency increases as magnet current increases from 0-0.75A. This operating condition corresponds to a region with high discharge current fluctuations, therefore adjusting the *outer* magnetic field would cause a change in efficiency.



(a)



(b)



(c)

Figure 49: Outer magnet effect on efficiency for various operating conditions.

#### **IV.4 Beam Current Density**

Another important task for this research was to examine BHT-600W exhaust plume, especially its beam current. The exhaust plume from a Hall thruster contains high-velocity ions that were neutralized by flow from a cathode. These particles can adversely impact the spacecraft if they found their way back. These ions can change the overall charge of the spacecraft, short circuit electronics, erode protective coating, and impinge on sensors. They can also increase thermal loads, cause deformation, and other damage to the spacecraft. To address these potential problems, a Faraday probe was used to examine the exhaust beam. The results helped to determine the beam efficiency as well as its shape.

Faraday probe provided local beam current density measurements. To determine the total beam current, the current density was numerically integrated over an entire beam sweep radius which was given by Equation 39. The total beam current was then correlated with discharge current, enable calculation of the beam efficiency. Additionally, the shape of the beam was quantified with its peak current and full width at half maximum (FWHM).

Faraday probe measurement is an intrusive method and was used for far-field measurement. Due to the high velocity exiting BHT-600W, the probe was placed at least 40cm away from the thruster's exit plane. Placing the probe any closer to the thruster would induce a current to the biased guard ring and skew the results. The Faraday sweep at nominal condition is illustrated in Figure 50. This corresponds to the same plume shape as shown in Figure 32.

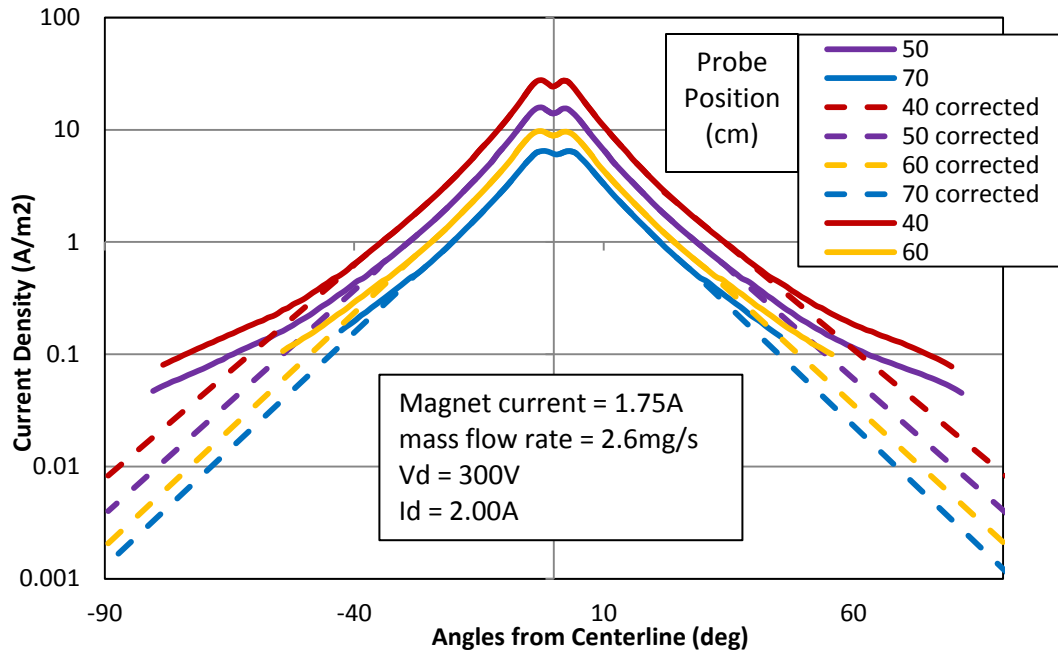


Figure 50: Faraday sweep for nominal condition.

The figure above represents the jet shaped beam found for conditions at or near nominal operating point. The plot shows the relationship between the beam current density and various beam divergence angles for different radial distances in log scale. It shows both left and right divergence angles from the centerline, so the symmetry could be evaluated. The dash lines are interpolated data compensated for missing measurements and charge exchanges with neutrals at larger angles. The results were expected for typical Hall thruster's plume. Charge exchange was detected to occur from around 30-50 degrees. However, it occurred at higher angles as the probe was positioned nearer the thruster. The current density distribution was highest near the thruster center line and approaches zero for higher divergence angle. As expected, a dip in current density at zero degree corresponds to the circular geometry of the thruster. The dip became less prominent as the probe was placed farther away from the thruster.

This research was interested in examining the exhaust plume for all conditions that operate within voltage control mode because that is where the thruster would most likely operates at if it was to put into service. The probe was swept from -90deg to +90deg from 40cm to 70cm at 10cm increment. However, physical limitations in the vacuum tank only allowed measurements for sweep from -75deg to +75deg at some positions. Therefore, extrapolated data was added to angles that could not be measured, from -75deg to -90deg. The sweeps were repeated for five different mass flow rates from 3.092mg/sec to 2.079mg/sec while varying discharge voltages from 80V to 400V. The results from Faraday probe scans at 40cm radial distance are plotted in Figure 51. Additional radial distances from 50-70cm are presented in Figure 79 through 81 in Appendix B.

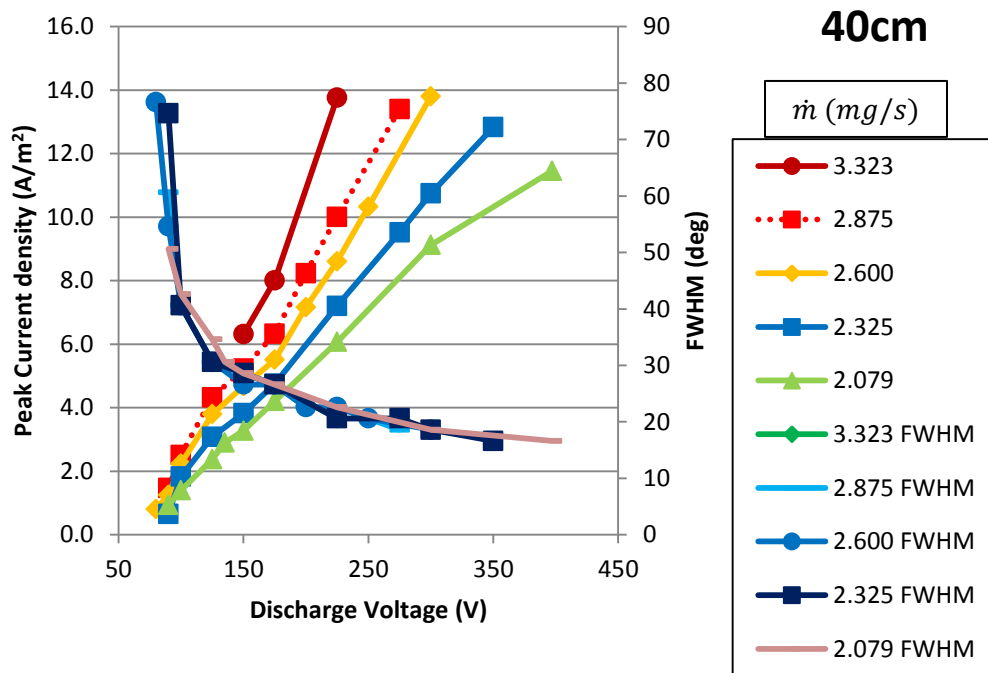


Figure 51: Faraday sweep at 40cm radial distance.

Figure 51 plots the peak current density and FWHM as a function of discharge voltages at five different mass flow rates. It also illustrates exhaust beam structure in the form of its peak current density and FWHM for various operating conditions. The data revealed that the beam peak current density increased linearly with discharge voltages. This relationship was observed to occur for all radial distances and for different mass flow rates. However, the increasing rate is not the same for different mass flow rate or radial distances. The peak density for high mass flow rates has higher slope compared to lower mass flow rates. For example, the data from the plot with the higher mass flow rate of 3.323mg/s has the slope of 0.1016 (A/m<sup>2</sup>-V) while the lower mass flow rate of 2.079mg/s has the slope of 0.035 (A/m<sup>2</sup>-V). The data also revealed the peak current density increased exponentially as the probe radial position approached the thruster. This trend can be seen from Figure 52. The following figure illustrates peak current as function of radial distance at different mass flow rates. The discharge voltage at these conditions was kept at constant 225V.

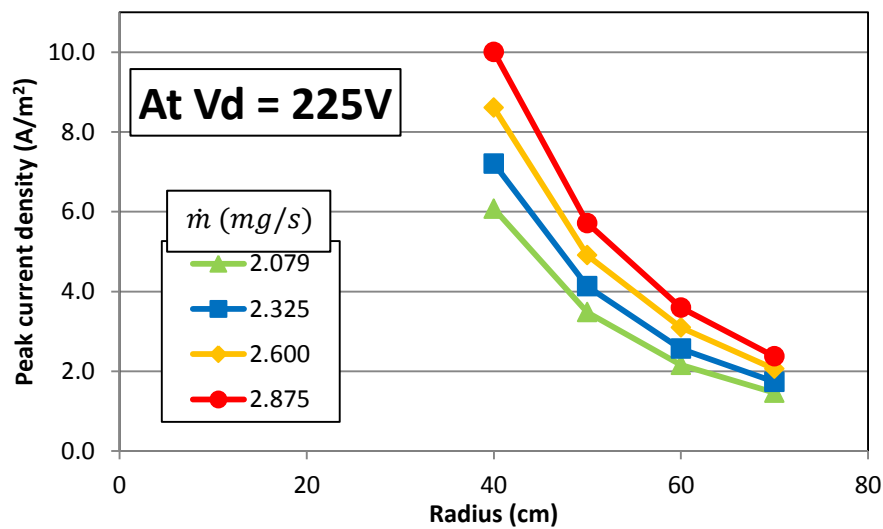


Figure 52: Faraday probe position effect on peak current density.

The FWHM was also plotted in Figure 51 as a function of discharge voltages and mass flow rates at four radial distances. Examining the figure showed FWHM decreases exponentially as discharge voltages increases. It means the beam shape was approaching an impulse characteristic. At first glance, the trend exhibited exponential decrease, but a detailed examination revealed linear decrease for some regions. For discharge voltages from 135V and higher, the FWHM has the slope of  $-0.069\text{deg/V}$ . The slope was steeper ( $-1.9\text{deg/V}$ ) for low discharge voltages from 80V-100V. It was around discharge voltages of 110V when the beam had wide divergence angles and started to focus into a cone shape. This phenomenon was also confirmed through physical observation. Discharge voltages around 110V represent a transition from the low current mode to a voltage control mode with cone shaped plume. It is theorized that the increase in voltage potential enables the energy within the discharge chamber to reach a certain level to accelerate the ionization process. Once the ionization process reached certain energy level, the beam became more focused and the cone shape appeared. The data also showed the FWHM was only affected by discharge voltages. The plots revealed that FWHM remained unaffected and constant for different mass flow rates and radial distances.

Another important parameter calculated from the Faraday probe data is the discharge beam current efficiency. The efficiency is given by the beam current and discharge current. It describes how efficiently the ion flow is exiting the thruster. This quantity was calculated for all the operating conditions discussed above. The results for 40cm radial distance are presented in Figure 53 below. Additional radial distances from 50-70cm are plotted in Figure 82 through 84 in Appendix B.

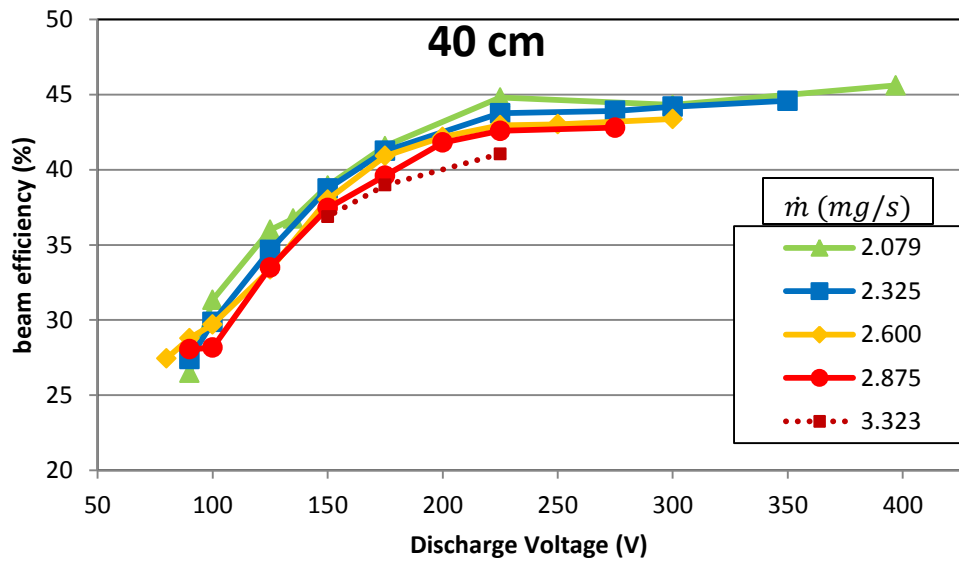


Figure 53: Beam efficiency at 40cm radial distance.

Figure 53 shows the discharge beam efficiency as a function of discharge voltage for various mass flow rates at 40cm radial distances from the thruster. All plots revealed that discharge beam efficiency increased at low voltages and reached its maximum point around 225V. The efficiency remained constant at maximum for discharge voltages greater than 225V. Additionally, the results showed different mass flow rates had little effect on beam efficiency. This voltage potential might represent the maximum energy level where the Xenon ions cannot be ionized further by this thruster. This phenomenon is better explained with ion species analysis, which will be discussed later in this chapter. The data also revealed that thruster operated with higher mass flow rates will produce the same efficiency as those with lower rates. The differences are small but became more prominent at higher discharge voltages.

Lastly, the results indicated that beam efficiency is affected by the probe's radial distance from the thruster. It is plotted in Figure 54 below. The figure graphs beam



efficiency as a function of the probe radial distance for four different mass flow rates. Again, different mass flow rates have little effects on beam efficiency. However, beam efficiency was affected by the probe placement. It almost linearly decreased as the probe placed farther away from the thruster. The extrapolated lines in the plot represent the maximum beam efficiency ranges from 52-56%, when the probe was placed at the thruster exit plane, with an assumption that the thruster was a point source. The results are expected because reduction in current intensity at farther downstream was due to recombination of electron and Xenon ions, CEX, and effect from constant solid angle.

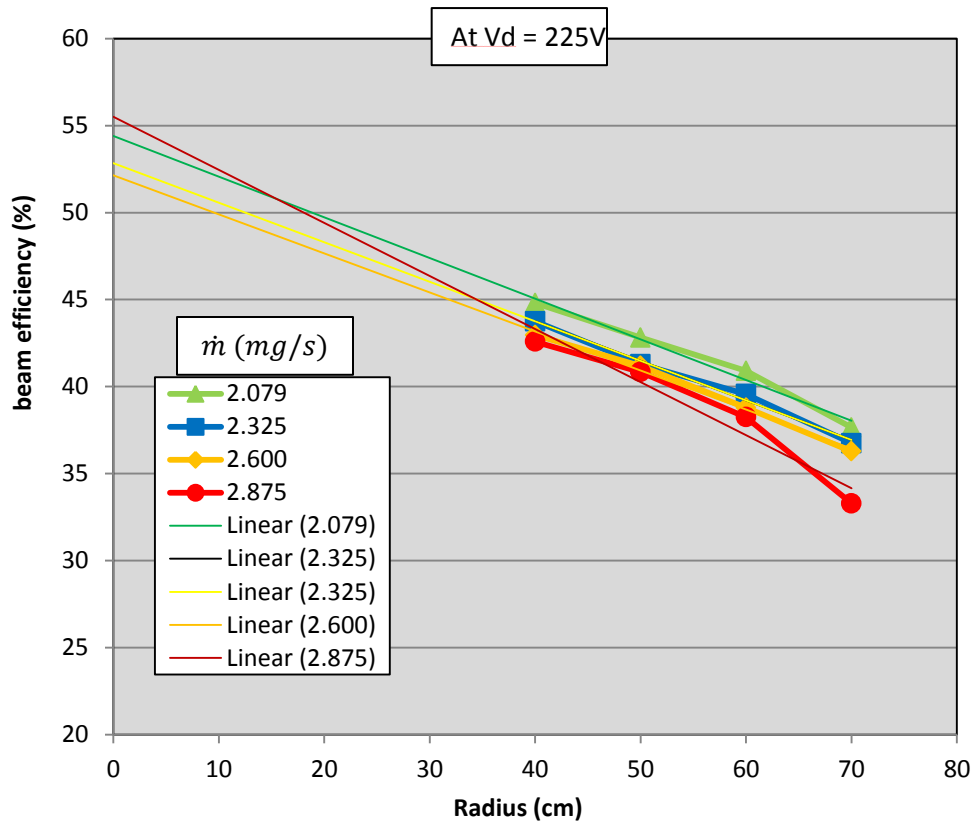


Figure 54: Beam efficiency relationship to probe radial distance from the thruster.

### A. Both Magnets Effects on Plume's Shape

This research also looked at the thruster exhaust plume from the effects of both magnet currents. Both inner and outer magnet coils were connected to their respective independent power supplies. Exhaust plume current density was measured for variations in both magnet coils current from 0A-3.0A at different operating conditions. All of the following Faraday measurements were done for a probe sweep from -90deg to +90deg with radial distance of 60cm. The Faraday probe was swept for mass flow rates of 3.092mg/sec, 2.600mg/sec, and 2.079mg/sec while varying three discharge voltages for each at 250V, 150V, and 100V. These test conditions are better illustrated in Figure 55, represented by purple diamonds.

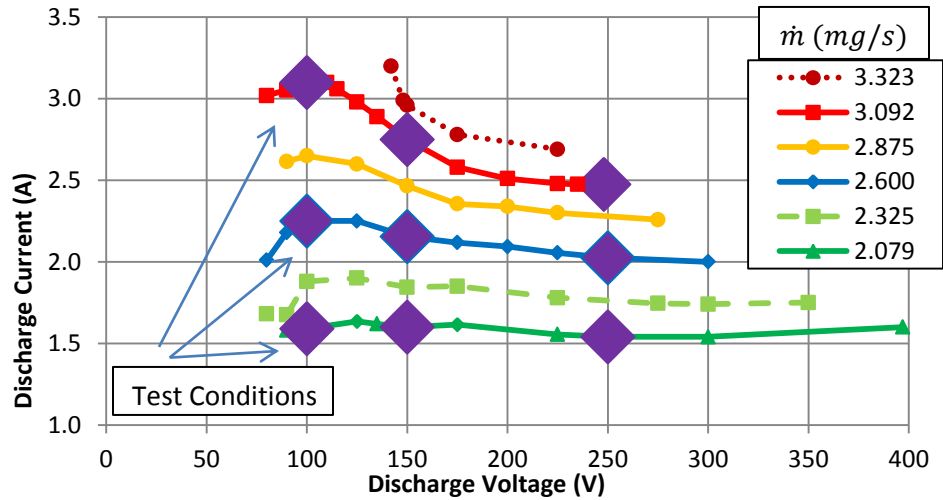


Figure 55: Operating points tested for magnet coils effects on plume shape.

The effects of magnet current on plume shape for mass flow rate of 2.079mg/s are presented in Figure 56 and 57. Additional data for mass flow rates of 2.600mg/s and 3.092mg/s are plotted in Figure 85 through 88 in Appendix B. Figure 56 and 57 illustrates the effects on peak current density and FWHM from magnets current at various

mass flow rates and discharge voltages. Overall, the results indicated that shape of the exhaust beam can be adjusted with various magnet settings. This is important because it allows the user to change the beam shape to be closer to an impulse. The plots reveal that for all mass flow rates, the beam with a low discharge power of 100V is highly affected by the magnet current in term of its FWHM. Lower magnet currents created a narrower beam while higher magnet currents caused the beam to diverge. As discharge voltages increased, the beam's FWHM became less sensitive to magnet currents. However, the effects on peak current density were more prominent. For low mass flow rates, the peak current density remained relatively constant for different magnet currents. Only as mass flow rates increase was it affected by the magnet currents. Figure 85 and Figure 88 in Appendix B show that maximum current density was found at magnet currents around 1.0-1.5A. This finding may not be accurate due to the lack of data for 250V in Figure 87 and 88.

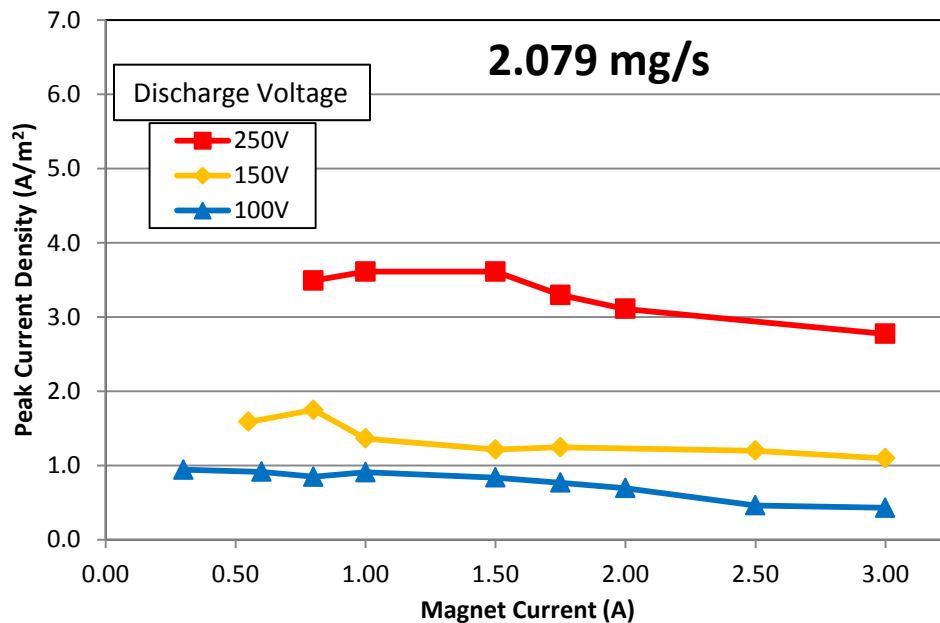


Figure 56: Magnets effects on peak current density.

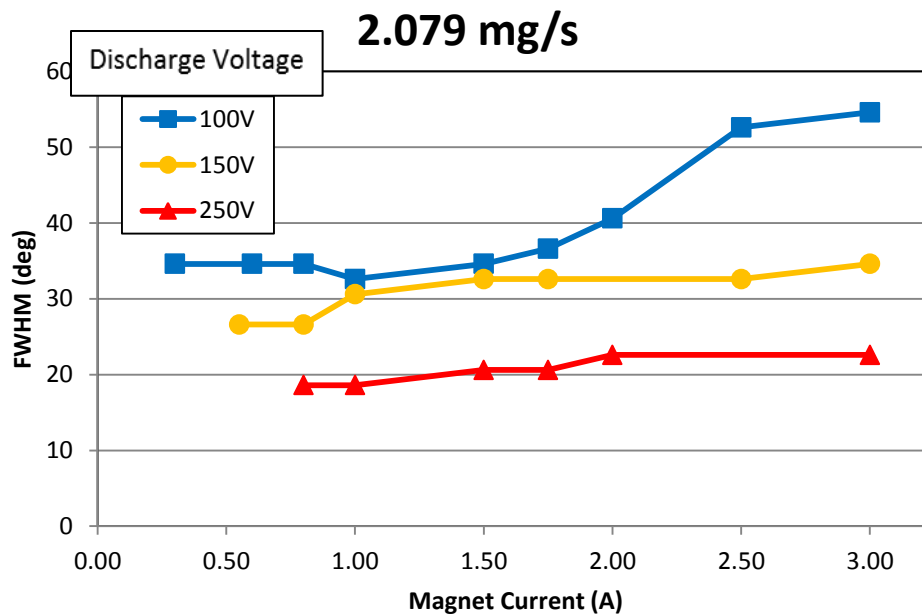
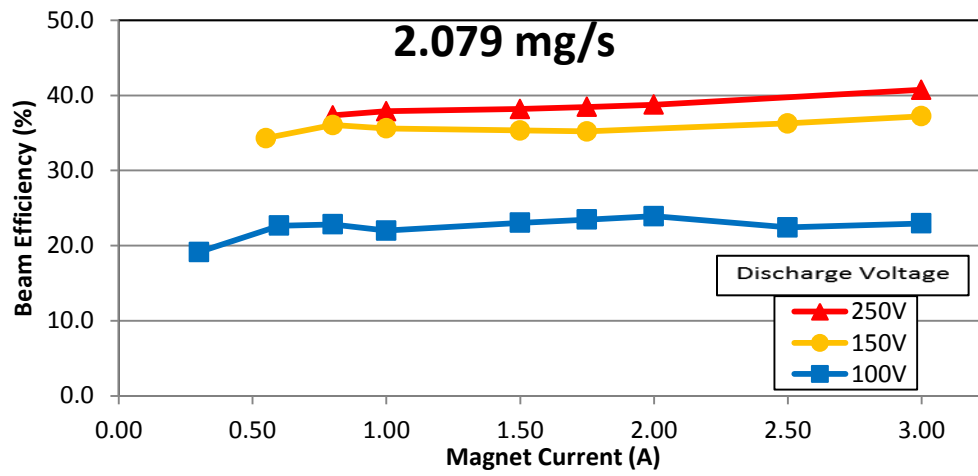
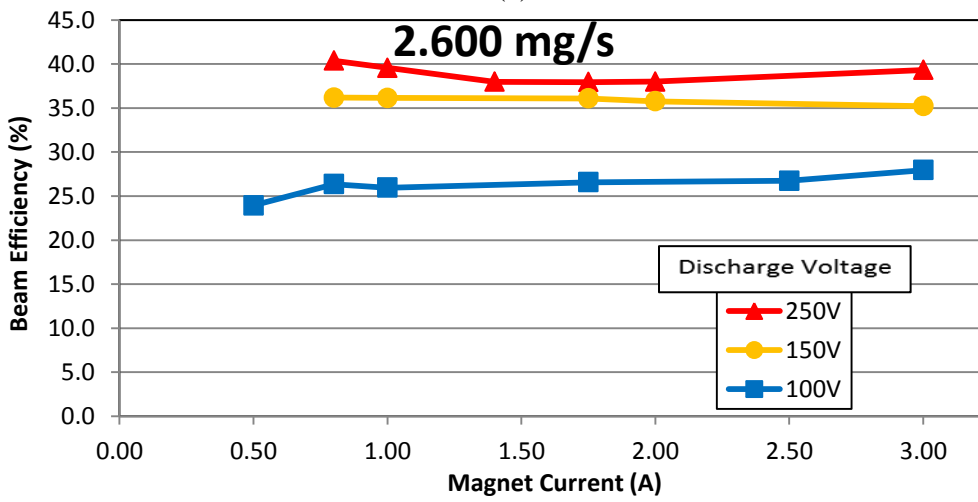


Figure 57: Magnets effects on FWHM.

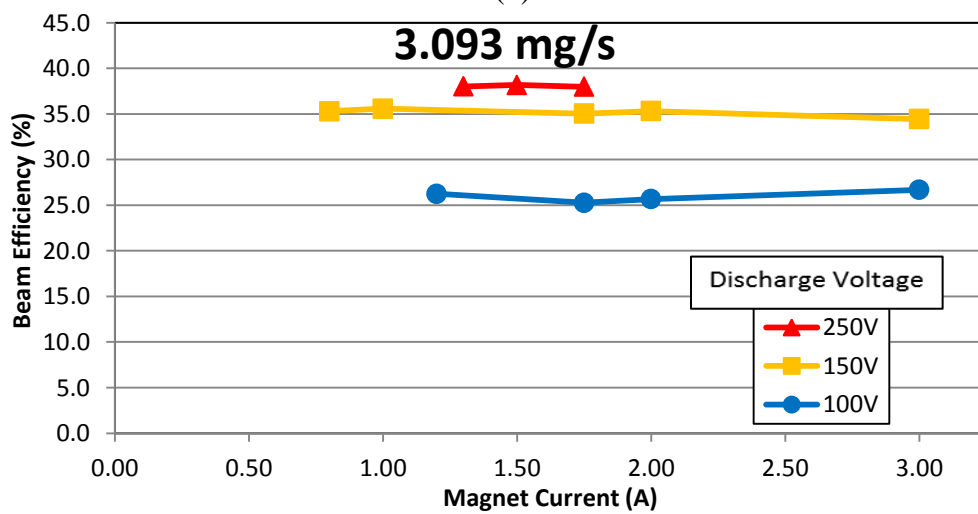
The study assessed the effects of magnet current on discharge beam efficiency. The results are plotted in Figure 58 below. Figure 58 illustrated discharge beam efficiency as a function of magnet current for different discharge voltages and mass flow rates. Overall, the magnet currents had very little or no effect on discharge beam efficiency for all nine conditions tested. However, plot (a) and (b) revealed that lower mass flow rates and low discharge voltage would reduce the beam efficiency if the magnet current is lower than 0.6A. This result corresponded to a region in the V-I curve where discharge current started to drop drastically at 100V discharge voltage.



(a)



(b)



(c)

Figure 58: Magnets effects on beam efficiency.

### *B. Inner Magnet Effects on Plume's Shape*

The effects on peak current density and FWHM were also calculated for different *inner* magnet current settings at the same six operating conditions as discussed above, illustrated by Figure 55. The measurements were done under the condition where the *outer* magnet coils were constrained to 1.75A while the *inner* coil varied from 0-3.0A. All of the following Faraday measurements had been taken at probe sweep from -90deg to +90deg with radial distance of 60cm. The peak current density and FWHM as a function of inner magnet currents for various mass flow rates, 2.079mg/s and discharge voltages are presented in Figure 59 and 60 below. Additional data for mass flow rates of 2.600mg/s and 3.092mg/s are plotted in Figure 89 through 92 in Appendix B. The peak current density remained the same for different inner magnet settings and discharge voltages for low mass flow rates as shown in Figure 59. For higher mass flow rates in plot Figure 89 and 91, it can easily be seen that there is a maximum peak-current density at low inner magnet settings. It located at 1.0A in Figure 89 and around 0.5A in Figure 91. The opposite effect was observed at the same locations for FWHM. The maximum points from peak-density current corresponded to the same dips in FWHM. This correlated with the transition of the plume shape from strong central cone to a less collimated and dispersed beam. At higher mass flow rates in Figure 91, the plume shape highly affected by inner magnet settings, especially at 100V discharge voltage. This is the region that borders with the current limit mode, so high fluctuation in plume shape is expected.

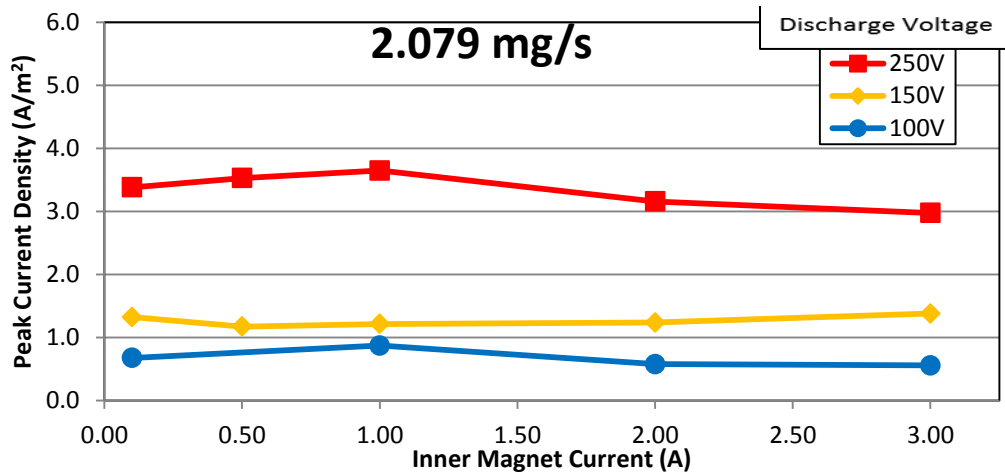


Figure 59: Inner magnets effects on peak current density.

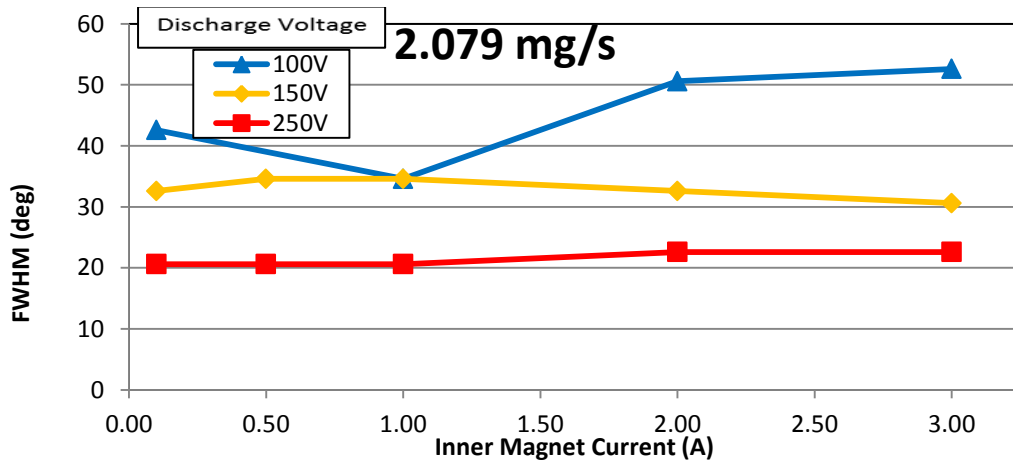
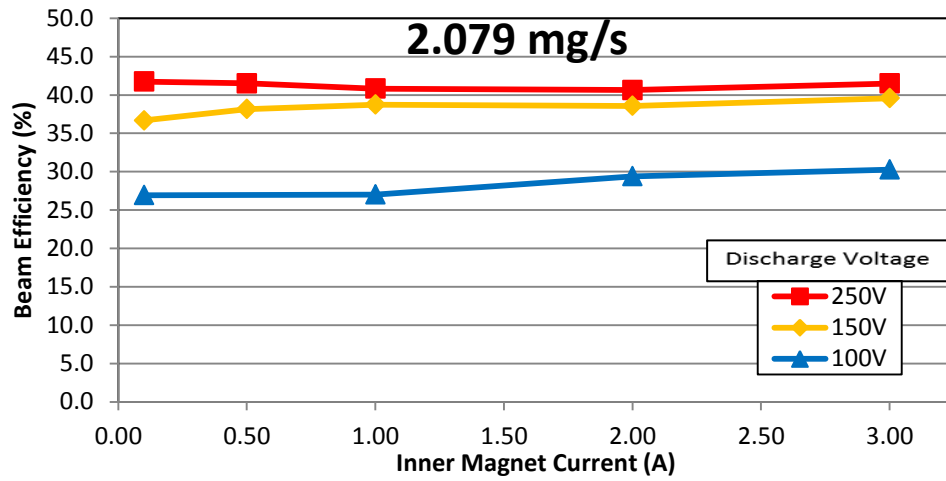
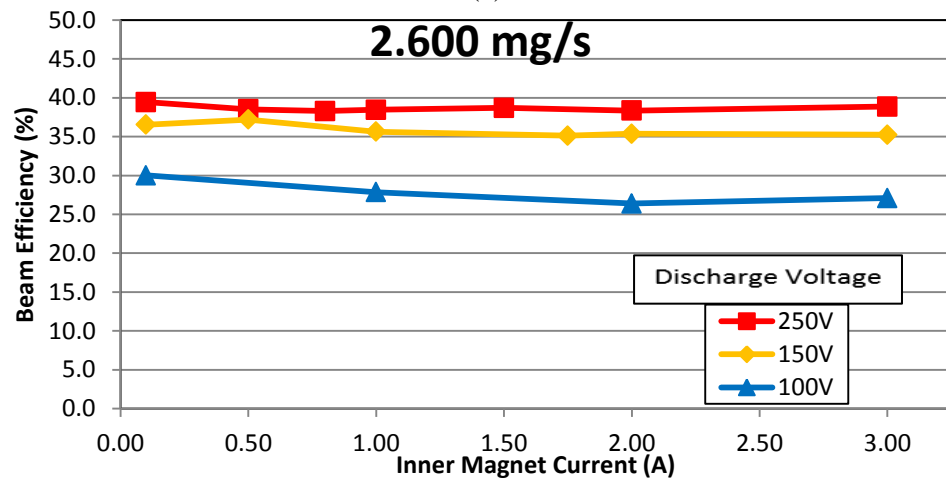


Figure 60: Inner magnets effects on FWHM.

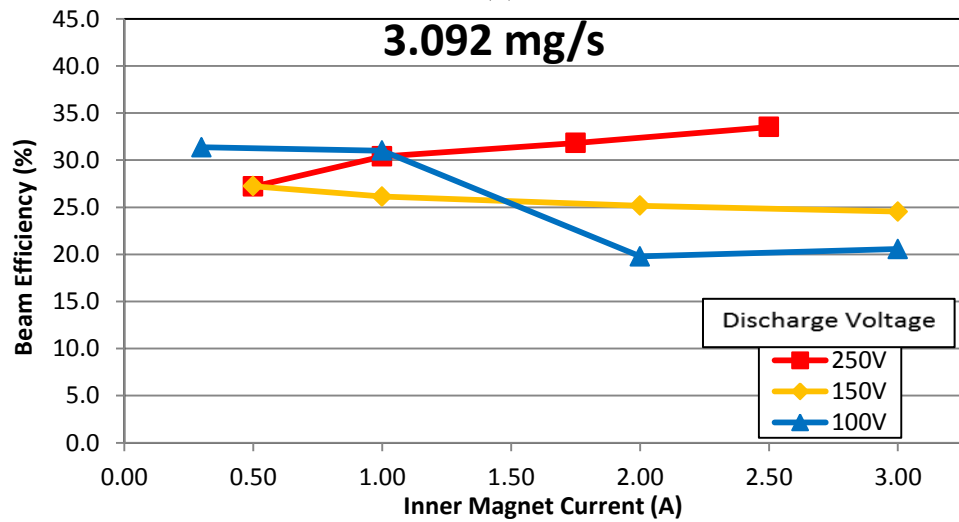
The effects of inner magnet currents on discharge beam efficiency were also examined. The results are plotted in Figure 61 below. Figure 61 illustrated discharge beam efficiency as a function of inner magnet currents for different discharge voltages and mass flow rates. Similar to the above analysis, the overall magnet currents have very little or no effects on discharge beam efficiency for all nine conditions tested. However, higher mass flow rates and low discharge voltages in plot (c) revealed beam efficiency fluctuation for different inner magnet settings. Again, this was due to transition from voltage control mode to current limit mode at that region.



(a)



(b)



(c)

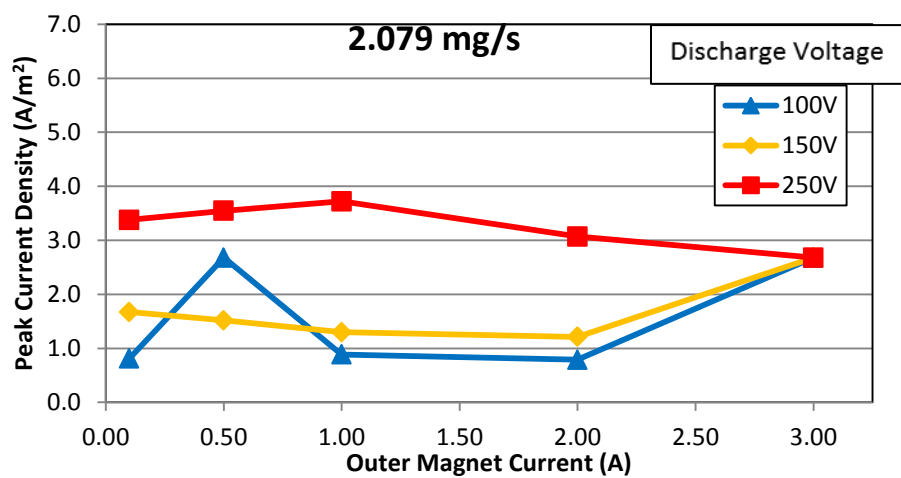
Figure 61: Inner magnets effects on beam efficiency.



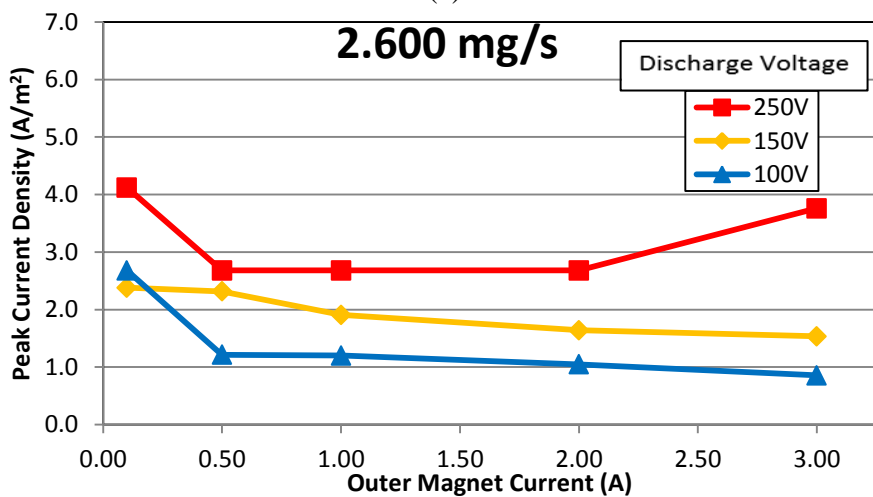
### *C. Outer Magnet Effects on Plume's Shape*

This experiment also examined at the effects on peak current density and FWHM from different *outer* magnet currents. The thruster operated at the same six conditions as discussed above, illustrated by Figure 55. The measurements were done at the condition where *inner* magnet coils were constrained to 1.75A while *outer* coil current varied from 0-3.0A. All of the following Faraday measurements had been taken at probe sweep from -90deg to +90deg with radial distance of 60cm. The peak current density as a function of *outer* magnet currents for various mass flow rates and discharge voltages are presented in Figure 62 below. All three plots revealed that the peak current density is highly affected by *outer* magnet currents, mass flow rates, and discharge voltages. There is no single *outer* magnet current that would produce a maximum in peak-current density that satisfies various mass flow rate and discharge voltage conditions. If one had to decide, *outer* magnet current at 1.0A would be the most reasonable. It is because more operating conditions showed that the peak current density reached its maxima for that point.

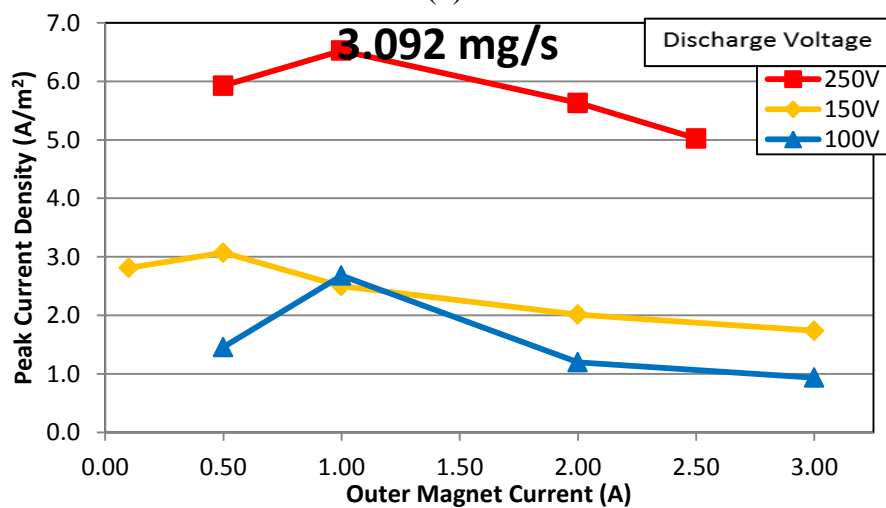
Analyzing results for FWHM also revealed that *outer* magnet current of 1.0A would produce a more collimated exhaust beam. Figure 63 below shows the FWHM as a function of discharge voltages at the same nine operating conditions as discussed earlier. Overall, the FWHM increased as the *outer* magnet current increased. This implied that higher *outer* magnet current would cause the plume to become wider or less collimated, which is undesirable. The plume also seems to exhibit less divergence at low *outer* magnet currents. Therefore, setting the *outer* magnet current at 1.0A would produce the most collimated plume.



(a)

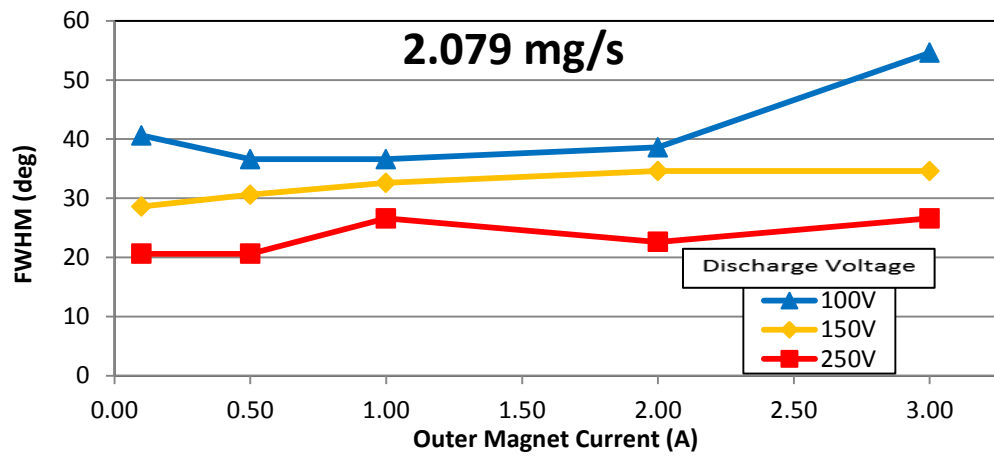


(b)

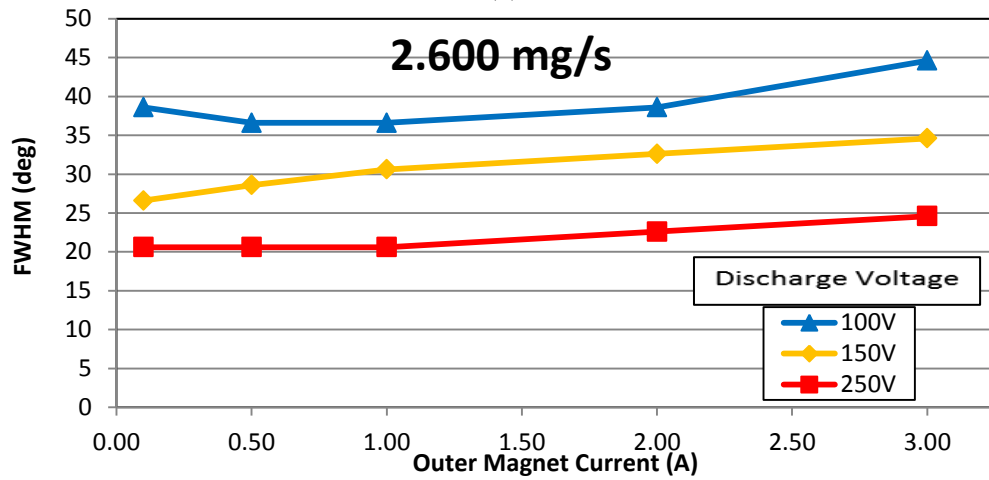


(c)

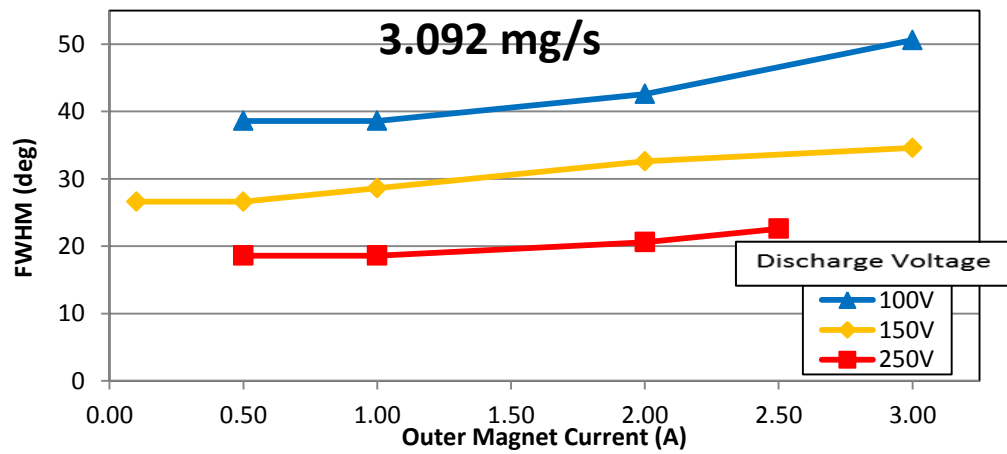
Figure 62: Outer magnets effects on peak current density.



(a)

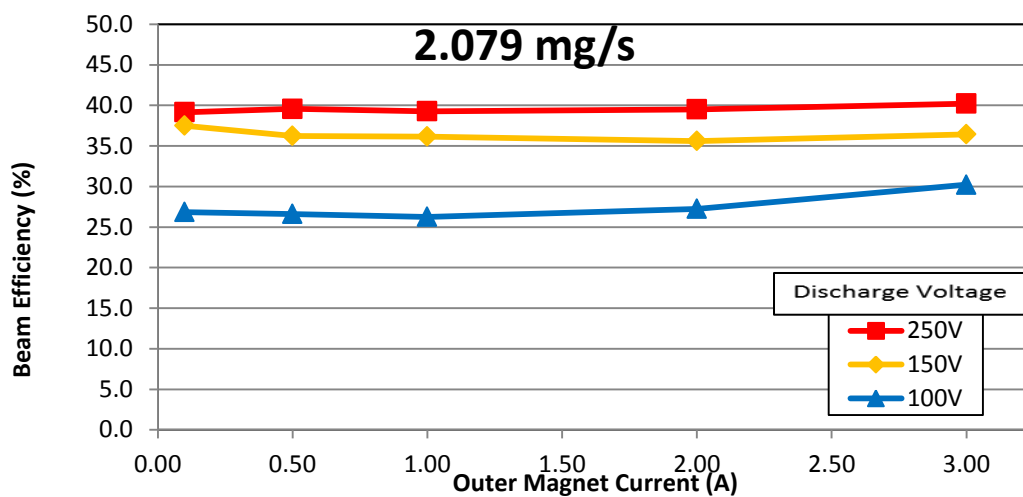


(b)

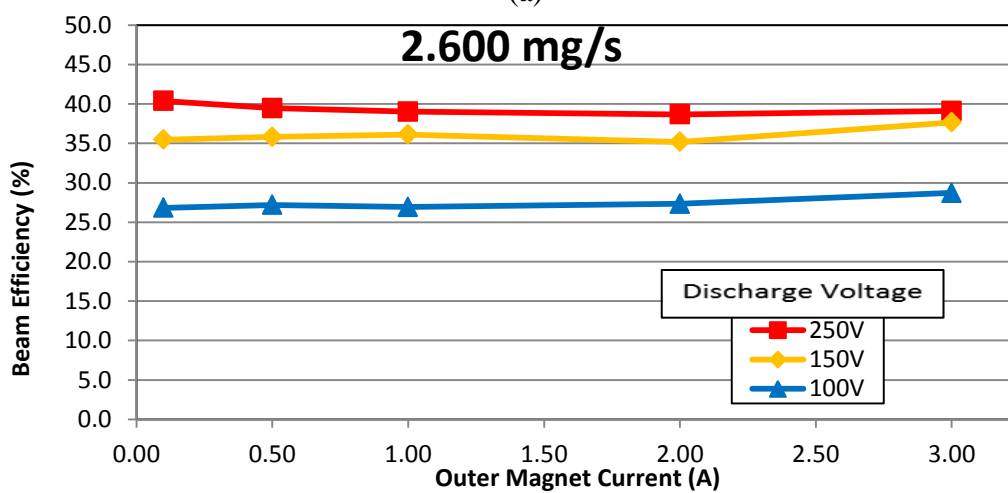


(c)

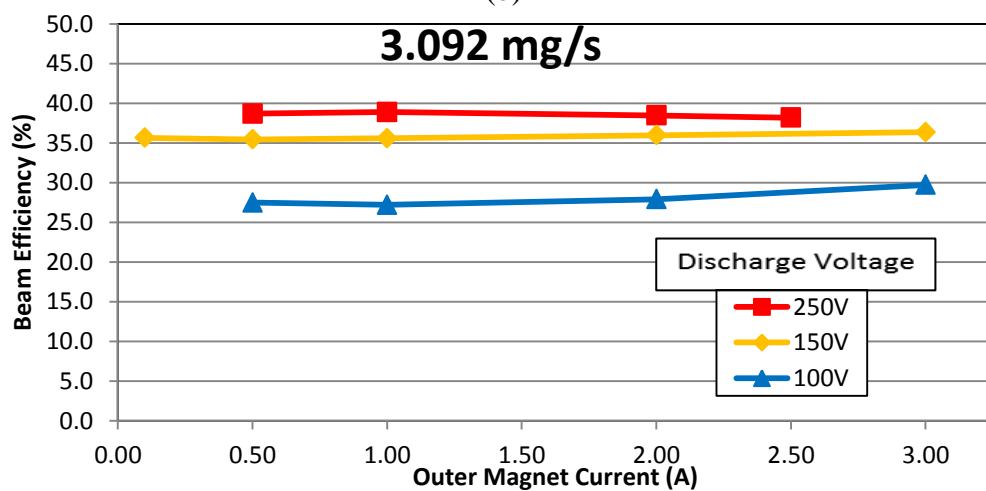
Figure 63: Outer magnets effects on FWHM.



(a)



(b)



(c)

Figure 64: Outer magnets effects on beam efficiency.

The effect of *outer* magnet currents on discharge beam efficiency was also examined. The results are plotted in Figure 64 below. Figure 64 illustrates discharge beam efficiency as a function of *outer* magnet current for different discharge voltages and mass flow rates. Overall, the *outer* magnet current has little or no effect on discharge beam efficiency for all nine conditions tested. Combining the results from peak current density and FWHM showed that adjusting *outer* magnet settings would only change the shape of the exhaust plume and not the thruster's beam efficiency

#### **IV.5 Ion Species**

Another method employed to examine the exhaust plume was using the ExB probe. Ion species fraction or species distribution were measured and determined by ExB probe. It is an important factor in determining the thruster overall efficiency, because ion species fraction is an essential variable to determine the multiply-charged ions correction factor. The probe has the ability to sort the plasma according to its velocity, energy, mass, and charge state [50]. This experiment used the probe to measure the exhaust plume velocity and energy. The ExB probe measurement provided the swept potential (V) and its corresponding current (pA) for certain location within the plume. The data was then used to calculate the ion species found within the plasma. Beam voltage efficiency could also be calculated from the data, but this research did not investigate this parameter due to time constraints. The theory behind this probe was presented in Diagnostic Tools in Chapter 2.

The ExB probe was positioned along the centerline and 60cm downstream from the thruster. This experiment determined that placing the probe closer than 40cm from the

thruster would cause the bias potential to fluctuate. The measurement would be inaccurate if the bias voltage was strongly disturbed by the exhaust plasma. The probe was fixed 60cm from the thruster while the voltage was swept from 0V to 50V, which should account for all major xenon species regularly found in hall thruster's plume. The voltage sweep for nominal operating condition is presented in Figure 65 below. Similar ExB trace for some other conditions can be seen from Figure 93 to 97 in Appendix C.

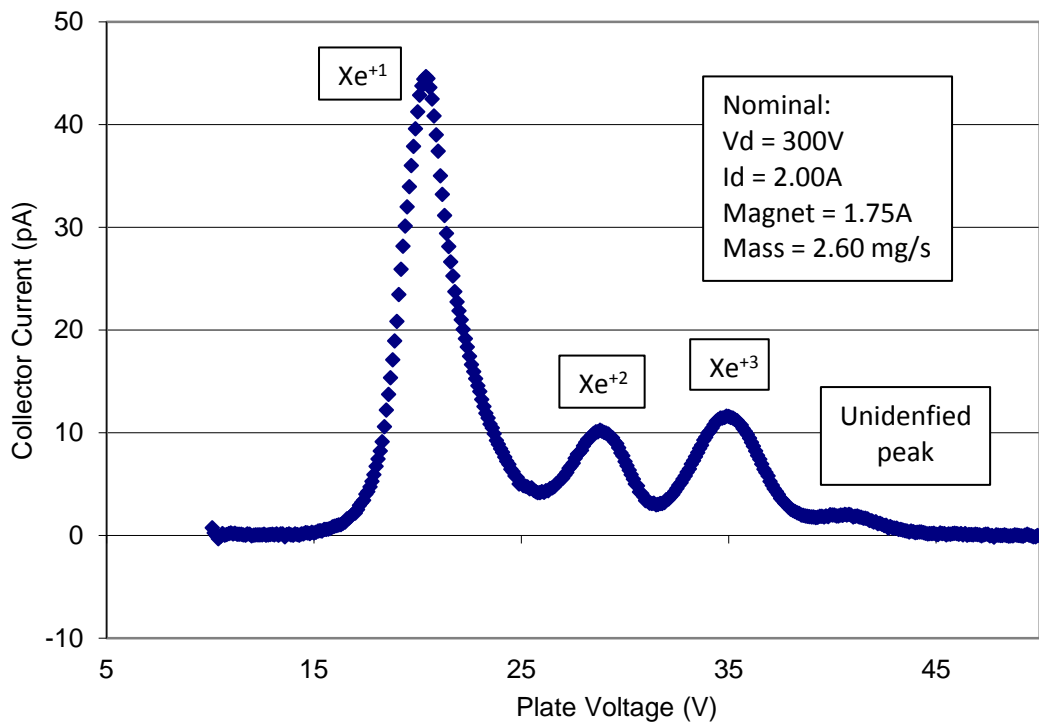


Figure 65: ExB swept for nominal condition.

Figure 65 plotted collector current (pA) as a function of swept voltages (V). The figure illustrated a typical ion species trace determined by ExB probe. There are distinct peaks for certain probe voltages. These current peaks were important because calculation for relative ion species fractions were highly dependent on them. This research only utilized the peak magnitude for calculation due to its simplicity and ease of automation

for large data sets, therefore the width and overlaps associated with each peak were neglected. The plot shows three distinct peaks, which represent energy for three different xenon species. Only xenon was expected because it was used as the propellant source. The first peak corresponds to  $\text{Xe}^{+1}$ , followed by  $\text{Xe}^{+2}$  and  $\text{Xe}^{+3}$ . The singly-charged peak was located at 20.4V, doubly-charged at 28.8V, and triply-charged at 34.9V. These voltages could be used to determine the beam voltage. At this nominal condition, the data yields ion species fraction for  $\text{Xe}^{+1}$ ,  $\text{Xe}^{+2}$ , and  $\text{Xe}^{+3}$  of 0.903, 0.051, and 0.041, respectively. From Figure 65, it is apparent that triply-charged peak is higher than doubly-charged. Higher collector current at  $\text{Xe}^{+3}$  peak suggested that energy was wasted ionizing xenon to a higher charge. This characteristic was found through all operating conditions with greater than 600W discharge power. Also, an unidentified peak in the figure above was not expected. The unidentified peak does not correspond to  $\text{Xe}^{+4}$  but rather an elastic collision between  $\text{Xe}^{+3}$  and  $\text{Xe}^{+4}$ . This resulted from same  $\text{Xe}^{+3}$  particles trying to make transition to higher state. However, some indications of  $\text{Xe}^{+4}$  species were detected for a different operating condition. When different a discharge voltage was applied, the ExB trace shifted and changed in magnitude. Figure 66 illustrates such change. The trace shifted to lower swept voltage (left) for lower discharger potential and vice versa. Also, the peak current reduced in magnitude as the discharge potential decreased. The reduction seems to decrease monotonically with decreasing discharge voltages. Also, higher charged or triply-charge ion peak currents vanished at lower discharge potentials. This shows that ion species production is highly affected by discharge potential.

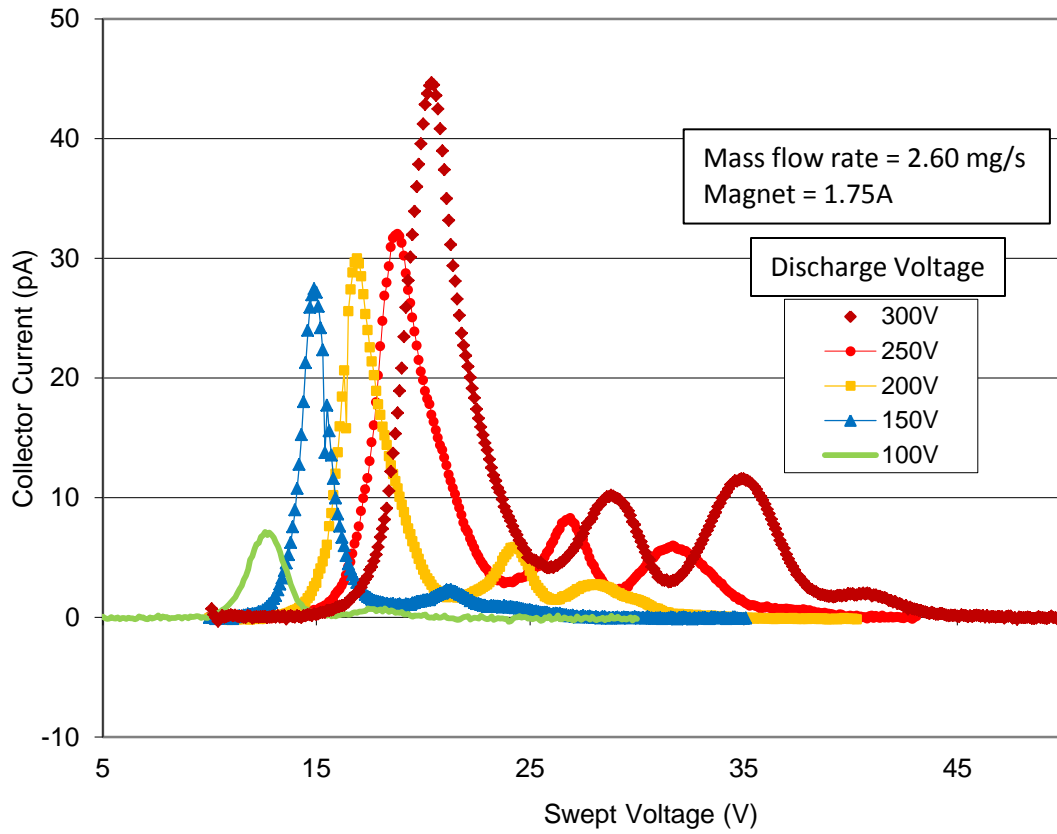


Figure 66: ExB sweep for different discharge voltages.

This research also looked at the ExB trace for all other conditions operated within voltage control mode. The ExB measurements were taken for five mass flow rates from 2.079 mg/s to 3.092 mg/s while varying the discharge voltage from 80-400V. The resulting ExB traces would contain too many plots to present in this paper; therefore, only ion species fractions were calculated and presented in Figure 67 below. The data yielded species fraction for  $\text{Xe}^{+1}$  makes up about 97-82% for discharge voltages from 80-400V, respectively. This result is in agreement with previous research [2, 22].



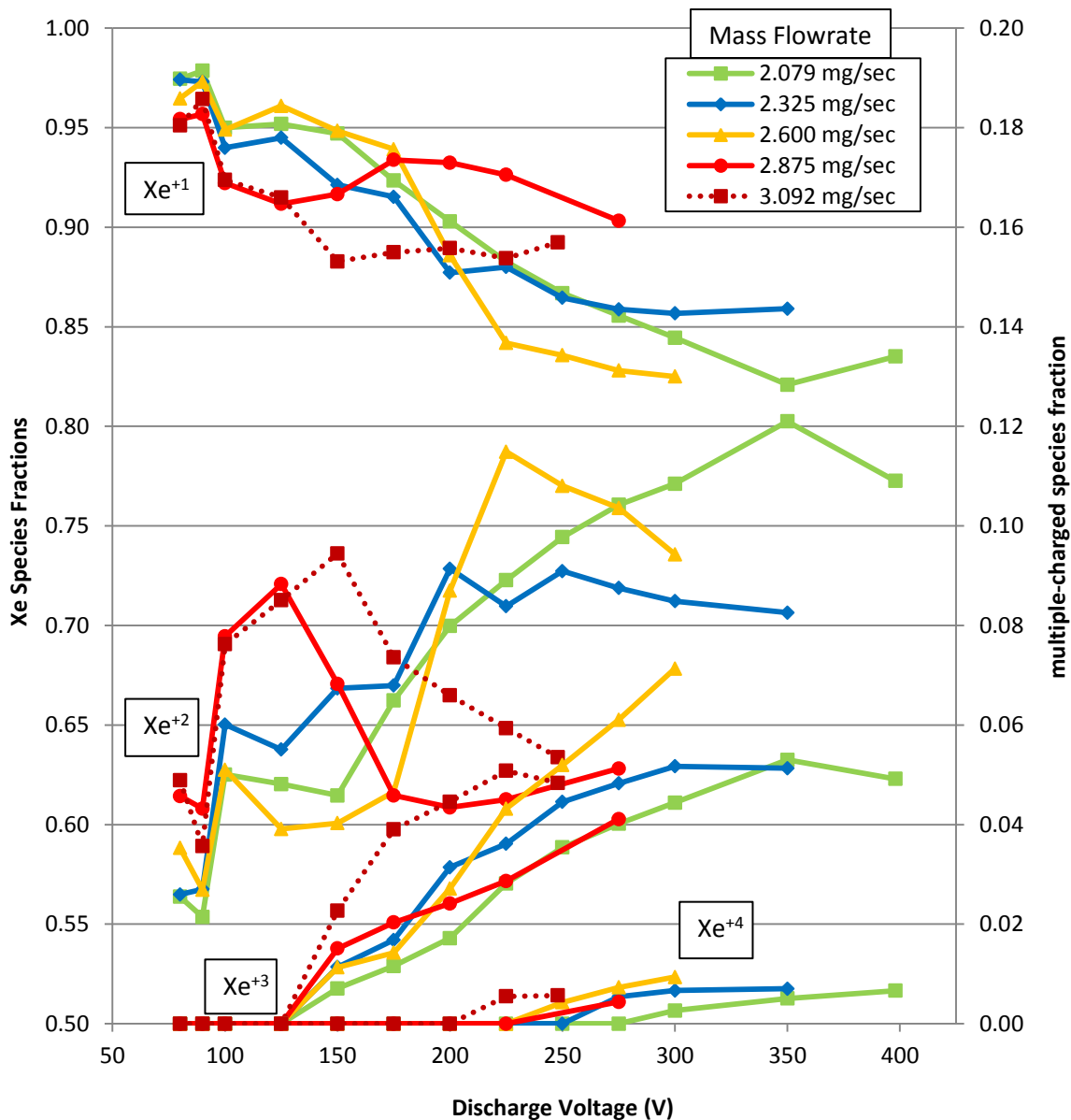


Figure 67: Xe species fractions for various operating conditions.

Figure 67 shows different xenon species fraction as a function of discharge voltages at five different mass flow rates. Overall, the data clearly showed that more highly charged species were produced as discharge potential increased. This further validated that ion species production was related to discharge potential. The graph

revealed that all charged species changed slowly with discharge potential, in a nonlinear fashion. This could be challenging if one tries to fit the experimental data into a model. It looked like creation of highly-charged species peaked around 300-350V, but this cannot be certain unless additional data is taken for higher discharge potentials. Unfortunately, this research could not operate the thruster at discharge voltage higher than 400V.

Figure 67 also shows ion species fraction for various mass flow rate. Similarly, more highly charged species were produced as the discharge potential increased for different mass flow rates. Lower mass flow rates such as 2.079mg/s and 2.325mg/s appeared to produce more  $\text{Xe}^{+2}$  than other flow rates. This was assumed to be caused by low mass within discharge chamber. Since extra energy was available was further excited charging xenon atom to higher states rather than ionizing new neutral xenon. Similar processes occurred for higher mass flow rates. For example, at a higher flow rate of 2.875mg/s and 3.092mg/s, the  $\text{Xe}^{+2}$  fraction decreased for 150V-175V discharge voltage. At same time, the  $\text{Xe}^{+3}$  fraction increased. Because there was not enough neutral xenon, extra energy pumped into the system was used to excite  $\text{Xe}^{+2}$  species to higher charges. This assumption was further validated by the appearance of  $\text{Xe}^{+4}$  species at higher discharge potentials. Therefore, any drop in the  $\text{Xe}^{+2}$  species curve most likely represented a transition to higher state. For mass flow rate of 2.079mg/s, 2.600mg/s, and 2.875mg/s, the transition occurred at discharge potential of 350V, 225V, and 125V, respectively. If the data were to be plotted as species fraction versus discharge powers instead of discharge potential, the  $\text{Xe}^{+3}$  and  $\text{Xe}^{+4}$  species would appear first at lower

power and lower mass flow rate. This indicates that more power is needed to excite xenon atoms to  $\text{Xe}^{+4}$  state. The plot of species fraction versus discharge power is presented in Figure 98 in Appendix C. The figure above indicates only  $\text{Xe}^{+1}$  and  $\text{Xe}^{+2}$  were created at low discharge voltages.

#### *A. Effect of Divergence Angles*

In addition to faraday probe measurements, this research used the ExB to examine the ion species within the plume shape. Previous research had shown that exit velocities of these charged particles could be as high as 16,000 m/s [22]. Therefore, it is important to evaluate the divergence angle so appropriate step can be taken to model the exhaust plume interaction with the spacecraft in orbit.

Similar to the experiment set up above, the ExB probe was set to perform a voltage sweep from 0-50V. However, a probe sweep was carried out for different divergence angles at 40cm radially away from the thruster. The divergence angles were varied from -90° to +90° at 5° increment. Due to physical dimension of the vacuum chamber, the experiment was limited to 40cm radial distance. Also, this research looked at the effects of divergence angles on ion species fraction only at the nominal condition: discharge voltage of 300V, discharge current of 2.00A, magnet current at 1.75A, and mass flow rate of 2.600mg/s. The calculated ion species fraction for divergence angles are plotted in Figure 68.

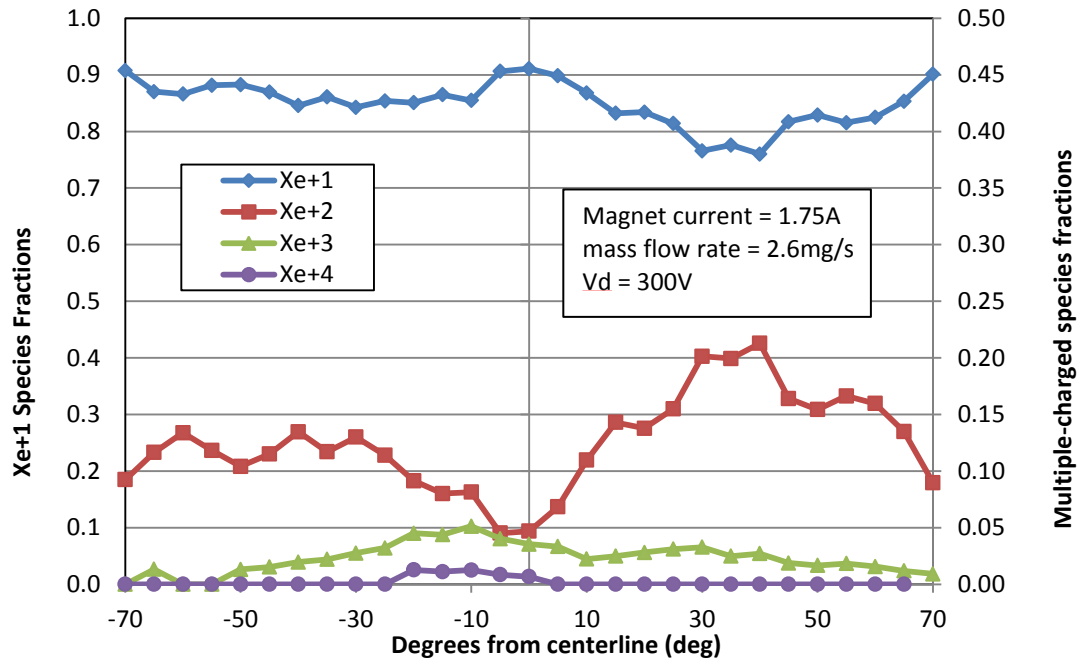


Figure 68: : Xe species fractions for various divergence angles.

Historically, increasing divergence angle caused population of singly-charge ion to decrease and multiply-charge ion to increase. The result showed that the  $\text{Xe}^{+1}$  species was the most prominent in the plume. It peaked near the centerline and fell as the beam diverged outward. Basically the ion species fractions shifted toward higher charges as the divergence angles move away from centerline  $-30^\circ$  to  $+30^\circ$ . This region corresponds to what is normally found in the literature [22]. This observation was expected because of the reduction in ion flux as the beam diverges. For divergence angles from  $-30^\circ$  to  $-70^\circ$ , the ion species fractions remain relatively constant. As from  $+30^\circ$  to  $+70^\circ$ , the ion species fraction shifted back to lower charges. The results at wider divergence angles were unexpected, but not unseen before [22].

The differences in the results could be due to many sources such as charge exchange, high background pressure, asymmetry in thruster geometry, background

environment, effectiveness of the probe, or incompatible math equation. Different results for left and right divergences angle may point to asymmetry in the thruster geometry; therefore, more experimental data is needed. However, Faraday data revealed that the exhaust plume was symmetrical, so the thruster geometry should be the same. The background pressure for this operating condition was around  $4.5 \times 10^{-5}$  torr. High background pressure may introduce additional collision and charge exchange. This occurrence may explain why the charge exchange wing started at  $30^\circ$  rather than at the wider angles from literature. Another reason was likely due to thermal effects on the ExB probe. It took about an hour to obtain the measurements for this data. During such a timeframe, there might be enough heat built up in the probe to cause the permanent magnets and electric plates to change their properties and skew the measurements. Also, the method used to determine the ion species fraction only considered the peak current ratio, which neglected the signal width and overlaps. This technique only applies to regions near the centerline, and it is invalid at angles contained charge exchange and collisions. The main reason for the unexpected results was assumed to be plume interaction with chamber walls. The exhaust particles most likely collided with the chamber wall and reflected back toward the plume. The energy transfer between low energy particles and highly charged-species caused the overall reduction in  $\text{Xe}^{+2}$  at angles higher than  $40^\circ$ . This finding was reinforced by the plot in Figure 69. The plot illustrates ExB trace for divergence angles at  $\pm 60^\circ$ ,  $\pm 65^\circ$ ,  $\pm 70^\circ$ . At negative angles, the appearance of an unidentified peak most likely represented plume interaction with the chamber wall.

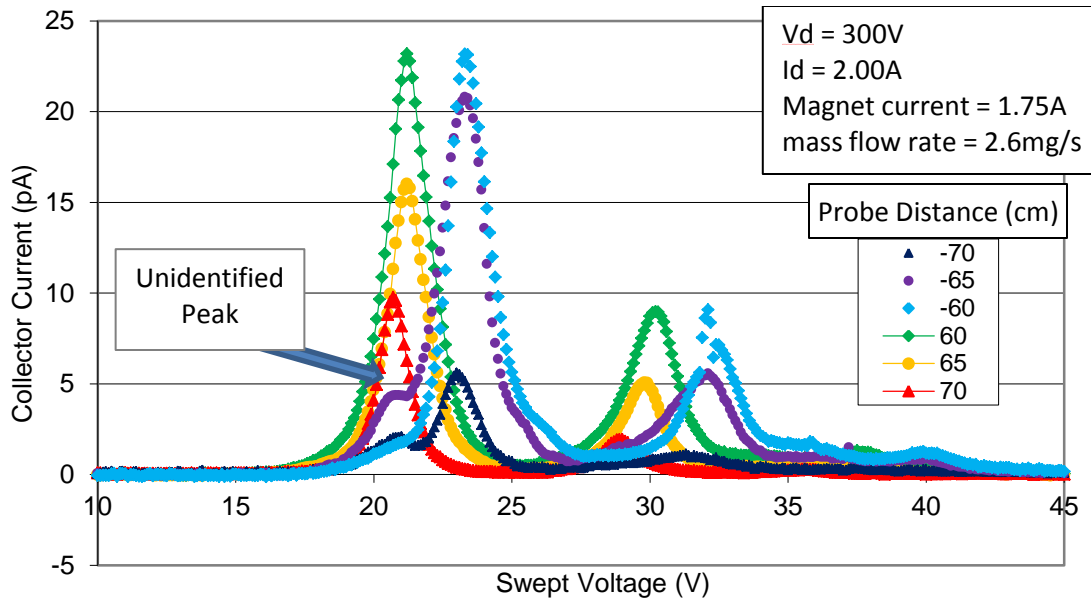


Figure 69: ExB trace for high divergence angles.

### B. Magnet Effects on Exhaust Species

This study also assessed the effects on ion species production from various magnet settings such as connecting the inner and outer magnets in series or varying one while keeping the other at some constant current. It was possible for the BHT-600W because it has the ability to control both magnet coils independently. The ExB probe setup was the same as before. It was placed 60cm radially away from the thruster while swept from 0-50V. An ExB sweep was performed for each tested operating condition. The thruster was tested with five operating conditions while both magnet coil currents varied from 0-3.0A. The operating conditions included mass flow rates of 3.092mg/s, 2.600mg/s, and 2.079mg/s and discharge voltages of 250V, 150V, and 100V. These test conditions are better illustrated in Figure 70, represented by purple diamonds. The experiment determined that ion species production was highly affected by both inner and outer magnetic coils setting.

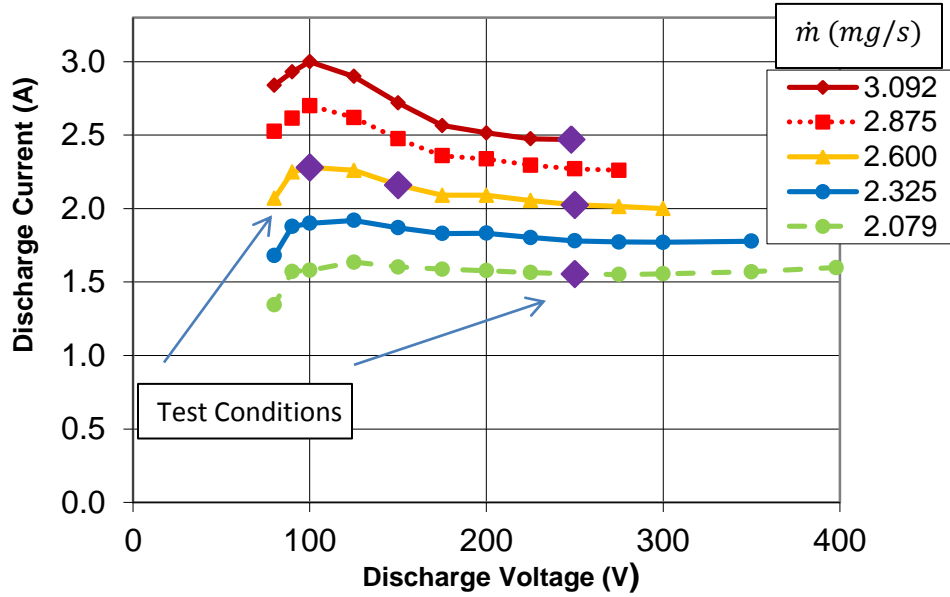


Figure 70: Operating points tested for magnet coils effects on xenon species.

The effects of magnet current on ion species productions are presented in Figure 71 and Figure 99 in Appendix C. Figure 71 illustrates the effects on xenon species from both magnet currents at various mass flow rates and a discharge voltage of 250V. Overall, the results indicated that species production shifts towards  $\text{Xe}^{+2}$  ions as the current in both magnets is increased from 0.5-3.0A. According to the plot, all major charged-species ions were present at low magnet current for all mass flow rates at a discharge voltage of 250V. However, the numbers of  $\text{Xe}^{+3}$  and  $\text{Xe}^{+4}$  decreased with higher magnet current while  $\text{Xe}^{+2}$  productions increased. At the same time,  $\text{Xe}^{+1}$  ion seem to remain constant for different magnet currents. The different proportions of ion species resulted from changes in magnetic field at different magnet current settings. This effectively changed the ionization process because the electron either speed up or slow down, depending on the B field strength, within the discharge chamber. This can be

explained by Equation 13. Also,  $\text{Xe}^{+1}$  was barely affected by the magnet current, implying that it was indifferent to energy level at this operating condition. The results indicated that the user has the capability to reduce energy being applied to multiply-charged ions or adjust the thruster ionization process.

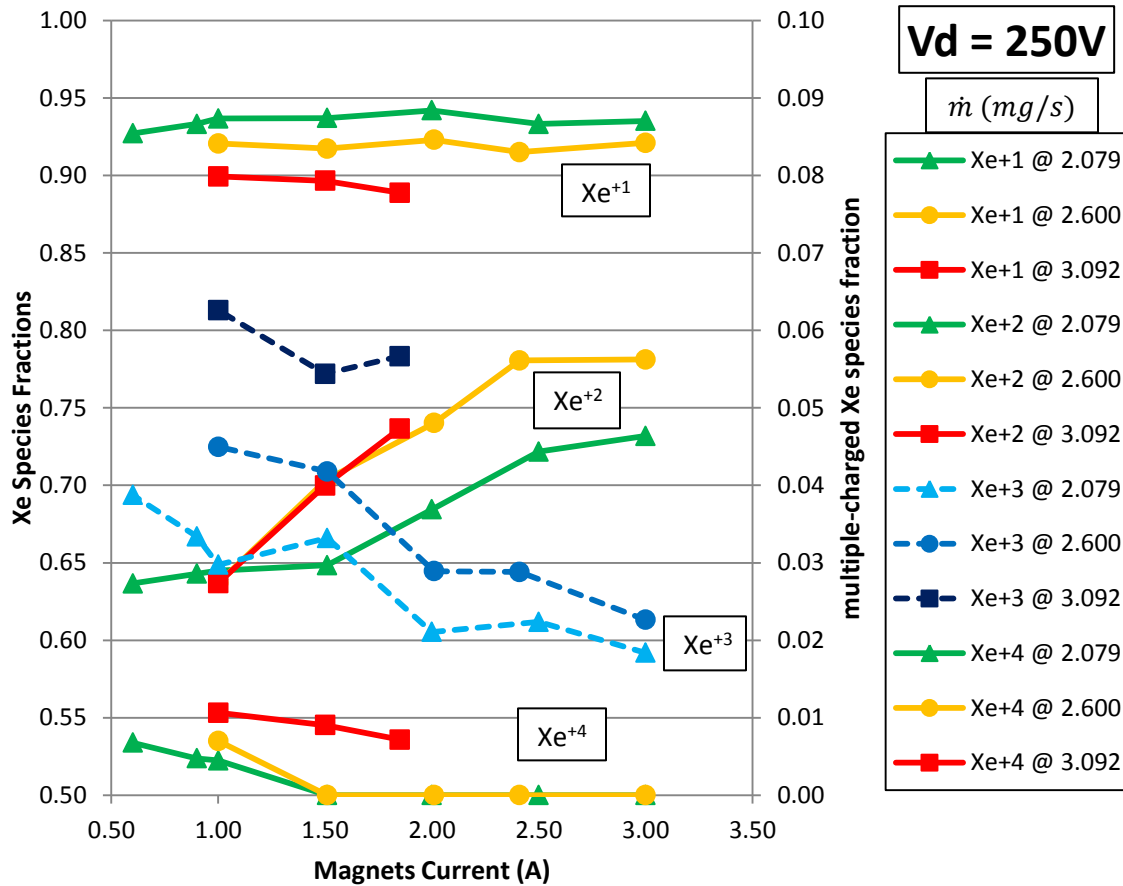


Figure 71: Magnet current effects on xenon species production.

The effect from various mass flow rates are also shown in the figure above. The data showed higher mass flow rates produced more multiply-charge ions than lower mass flow rates. It means that there is proportionally more  $\text{Xe}^{+1}$  for low mass flow. This result is desirable because lower mass flow rates and higher  $\text{Xe}^{+1}$  means less propellant used and



less wasted energy goes into the ionization process. The data also revealed that higher mass flow rates shift ion production toward multiply-charge states. This clarified earlier analysis that showed an inconclusive effect of mass flow rates on ion species production as illustrated in Figure 67. Similar data was present for conditions with a constant mass flow rate of 2.600mg/s while varying discharge voltages at 100V, 150V, and 250V. The results showed a similar trend for various magnet current settings. The overall results indicated that species production shift toward  $\text{Xe}^{+2}$  ions as the current of both magnets increased from 0.5-3.0A. This data is presented in Figure 99 in Appendix C.

### *C. Outer Magnets Effects on Exhaust Species*

The effects on ion species production from various *outer* magnet settings were also examined. The BHT-600W has the ability to enable the end-user to set *inner* magnet at constant current while adjusting *outer* coils to various settings. The ExB probe setup was the same as before; 60cm radially distance and voltage sweep from 0-50V. An ExB sweep was performed for each tested operating conditions. The thruster was tested with seven operating conditions while the *inner* magnet remained at a constant 1.75A and the *outer* magnet coils currents were varied from 0-3.0A. The operating conditions included mass flow rates of 3.092mg/s, 2.875mg/s, 2.600mg/s, 2.325mg/s, and 2.079mg/s and discharge voltages of 300V, 250V, and 100V. These test conditions are illustrated in Figure 72, represented by purple diamonds. The experiment determined that ion species production was affected by *outer* magnetic coils settings.

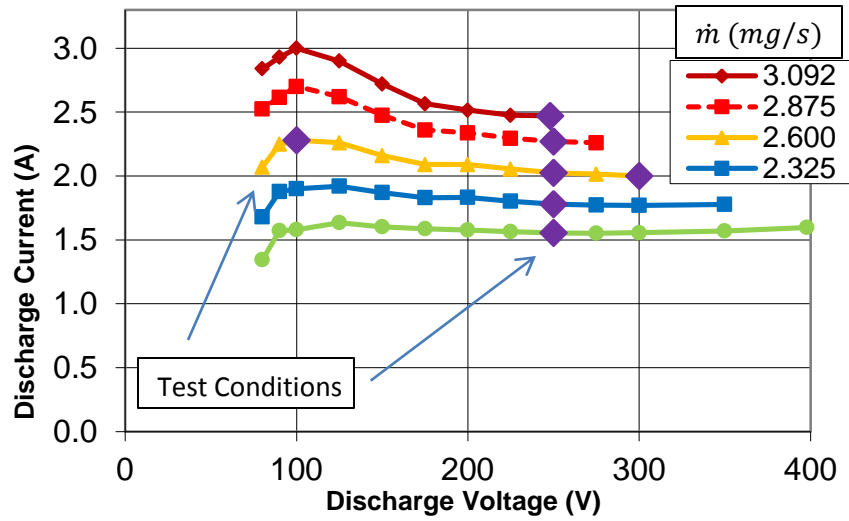


Figure 72: Operating points tested for outer magnet coils effects on xenon species.

The effects of *outer* magnet current on ion species productions are presented in Figure 73 and Figure 100 from Appendix C. Figure 73 illustrates the effects on xenon species from outer magnet current changes at various mass flow rates and discharge voltages of 250V. Overall, the results indicate the same pattern found in previous analysis. The plot shows that species production shifts toward  $\text{Xe}^{+2}$  ions as the current of the *outer* magnets was increased from 0.5-3.0A. The plot revealed that for all mass flow rates, all major charged-species ions were present at low *outer* magnet currents. The number of  $\text{Xe}^{+3}$  and  $\text{Xe}^{+4}$  decreased with higher magnet current while  $\text{Xe}^{+2}$  productions increased. At the same time,  $\text{Xe}^{+1}$  ions remain constant for different *outer* magnet currents. The effects from mass flow rates and outer magnet current were almost identical to previous analysis. The data showed that higher mass flow rates produced more multiply-charged ions than lower mass flow rates. However, it was less prominent for  $\text{Xe}^{+2}$  species. Also, more  $\text{Xe}^{+1}$  species were found in low mass flow rates than those in higher mass flow rates, which is desirable.

The data for condition at constant mass flow rate of 2.600mg/s while varying discharge voltages at 100V, 150V, and 250V are plotted in Figure 100 in Appendix C. The plot illustrates the effect of ion species production as a function of *outer* magnet current for constant mass flow rates. The results showed similar trends compared to previous analysis. The overall results indicated a species production shift toward  $\text{Xe}^{+2}$  ions as *outer* magnet current increased from 0.5-3.0A. The results also showed that the user has the capability to regulate production of ion species with *outer* magnet current.

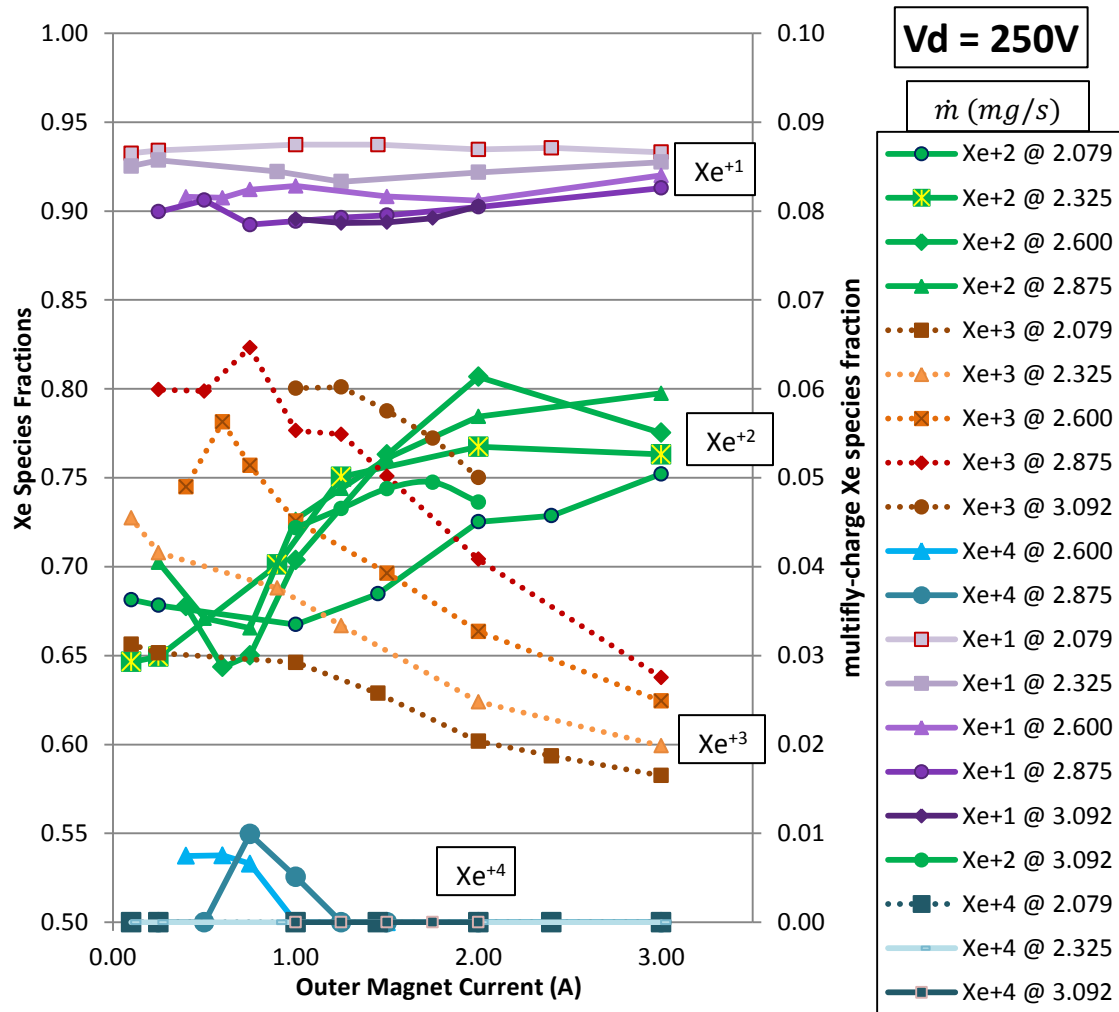


Figure 73: Outer magnets current effects on xenon species production.

#### D. Inner Magnets Effects on Exhaust Species

The same experiment was performed for the *inner* magnet coil. The experimental set up was exactly the same as for outer magnet methods. However, an ExB sweep for each test point was performed at different operating conditions. The thruster was tested with five operating conditions while outer magnet coils remained at constant 1.75A and *inner* magnet coil currents varied from 0-3.0A. The operating conditions included mass flow rates of 3.092mg/s, 2.600mg/s, and 2.079mg/s and discharge voltages of 250V, 150V, and 100V. These test conditions are shown in Figure 74, represented by purple diamonds. The experiment determined that ion species production was affected by inner magnetic coil settings.

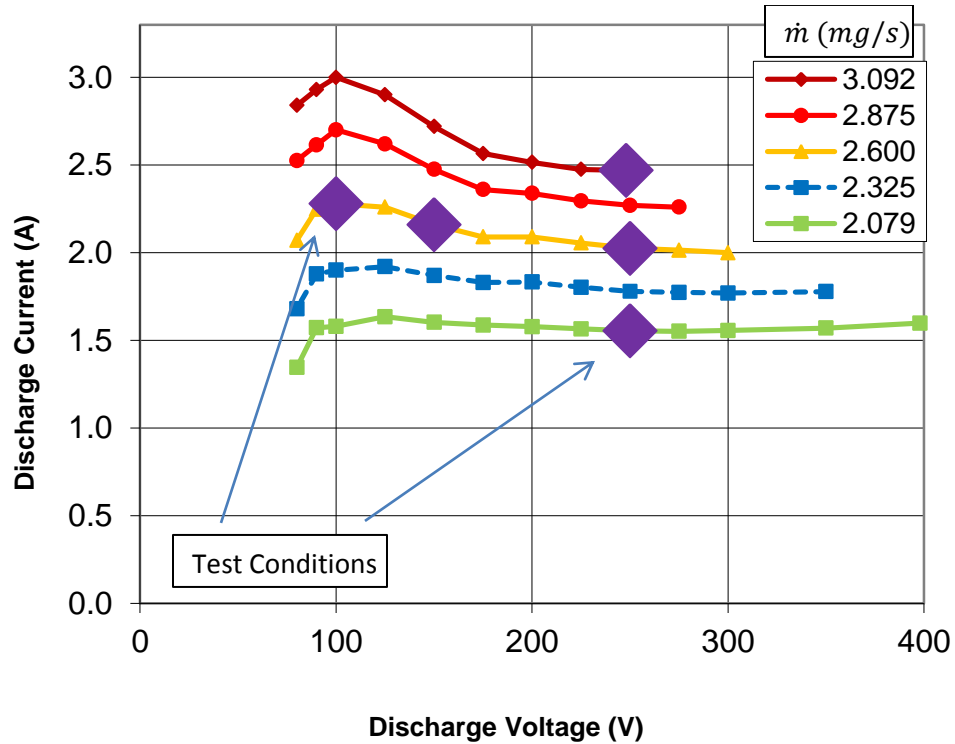


Figure 74: Operating points tested for inner magnet coil effects on xenon species.

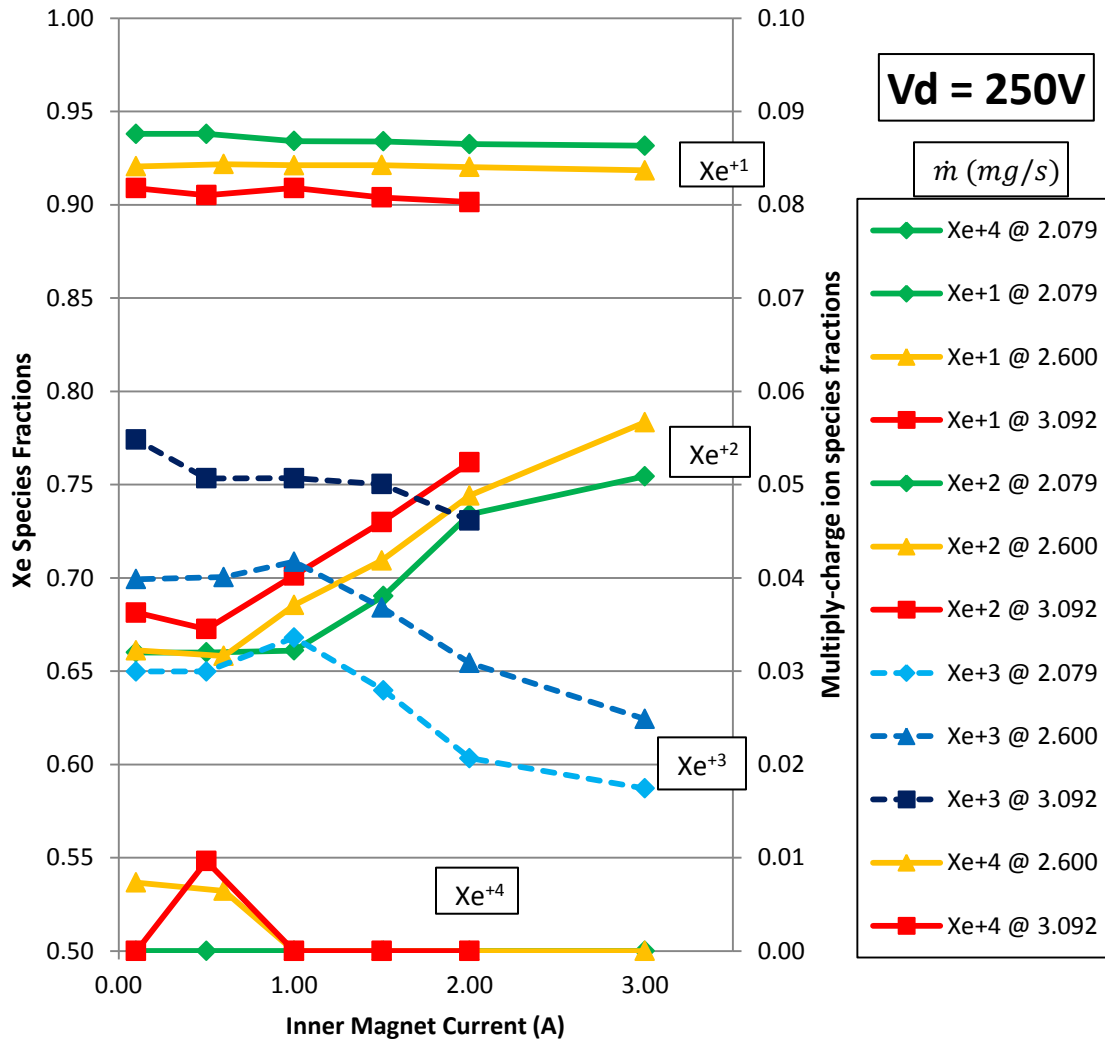


Figure 75: Operating points tested for inner magnet coils effects on xenon species.

The effects of *inner* magnet current on ion species productions are presented in Figure 75 and Figure 101 in Appendix C. Figure 75 illustrates the effects on xenon species from *inner* magnet currents at various mass flow rates and a discharge voltage of 250V. Overall, the results were found to be the same as before. The plot shows that species production shift toward  $\text{Xe}^{+2}$  ions as current of the *inner* magnets increased from 0.5-3.0A. The number of  $\text{Xe}^{+3}$  and  $\text{Xe}^{+4}$  decreased with higher magnet current while  $\text{Xe}^{+2}$

productions increased. The  $\text{Xe}^{+1}$  species remained constant for different inner magnet currents. The data showed higher mass flow rates produced more multiply-charge ions than lower mass flow rates. However, the figure indicated higher  $\text{Xe}^{+1}$  species fractions were found in low mass flow rates for all magnet current settings. Additional data for conditions of constant mass flow rate of 2.600mg/s with varying discharge voltages at 100V, 150V, and 250V are plotted in Figure 101 in Appendix C. The results correspond to the same trend as previous analyses. The *inner* magnet current also has the ability to regulate ion species production. The overall analysis of BHT-600W magnets leads to a conclusion that any combinations of *inner* and *outer* magnet currents give the user the ability to control ion species production.

The characterization of BHT-600W was presented in the form of a V-I curve and thruster performance such as thrust, specific impulse, and propulsive efficiency from thrust stand measurements. This research examined the exhaust plume with Faraday and ExB probe. It was determined the thruster's performance improved as discharge voltage increased while propellant mass flow rate decreased, which was expected. Additionally, in term of beam current density and species mass fraction, the exhaust plume exhibited a similar trend found in other Hall thrusters. Lastly, the two magnet coils found in BHT-600W has the capability to adjust the exhaust beam shape but yield minimal improvement on performance.

## **V. Conclusion and Recommendation**

Studies have shown that electrical propulsion system such as a Hall thruster provide substantial cost savings, increased payload and reduce complexity. The Busek Co. 600 Watt Hall thruster (BHT-600) is one of many electric propulsive systems available. In this study, the thrust and the exhaust plume of the BHT-600 were measured in terms of current density, divergence angles, and charged ions species and analyzed for propulsive and beam efficiencies during different operating conditions.

### *V.1 Challenges and Implications*

This research had four objectives laid out at the beginning. All were successfully met and some exceeded. Many challenges and implications arose. One was that not all operating conditions were examined by this research. Although the thruster can operate under millions of different operating conditions, this study only inspected operating points close to nominal conditions and the boundary points. A voltage control model region was derived from the V-I curves, setting the operation limits for the BHT-600 because this thruster can only operate effectively within the voltage control mode. Data from this study suggested that BHT-600 should only operate in the discharge voltage range of 80–400V, mass flow rates of 2.079–3.323mg/s, and magnet currents of 0.5–3.0A. For discharge voltages lower than 80V, the thruster would enter the ball plume mode or low current mode. For conditions with low discharge voltages and high mass flow rates, the thruster would transition into current limit mode. Operating the thruster away from its nominal point would degrade its performance.

The other challenge was the limitations of the power source for the PPU, that severely limited data collection for higher power conditions. The power supply for the BHT-600 during this experiment was limited to a discharge power of 625W. This problem was not discovered until the end of the experiment. Therefore, only data for conditions up to 625W was collected, and thruster performance at conditions from 625W to maximum 800W was not examined. Due to this limitation, a supplement study is needed to characterize the full range of the BHT-600's performance capabilities.

## *V.2 Thrust Stand Measurements*

The inverted pendulum stand was used to measure the thruster performance parameters such as thrust and specific impulse for different discharge voltages. The BHT-600W's thrust profile was measured for various discharge voltages as well as at different mass flow rates. In addition, the experiment also looked at thruster performance as a function of various magnet settings. Thrust was directly measured using a Busek's T8 inverted pendulum thrust stand. The nominal condition for BHT-600W was at 300V discharge voltage, 2.0A discharge current, 2.66 mg/s, and 1.75A magnet current. This research determined optimal performance for this thruster was lower but close to values stated by Busek Co. The measured values were  $34.8 \pm 1.3$  mN of thrust,  $1,267 \pm 39$ s specific impulse, and the measured propulsive efficiency was  $36.2 \pm 2.4\%$ . Last, beam efficiency from Faraday probe measurements yielded  $52.1 \pm 0.27\%$ .

The thruster's performance was measured at five different mass flow rates while varying discharge voltage from 60V to 400V. Overall, it has been observed that there was a monotonic relationship between thrust and discharge power. Measured thrust was



about the same for different mass flow rates and it increased with discharge power. The results for  $I_{sp}$  showed a similar trend. However, the data indicated that higher  $I_{sp}$  was obtained for lower mass flow rates, and the opposite was true for higher mass flow rates. The overall propulsive efficiency increased as discharge power increased. It settled to maximum value for discharge voltages around 600V. The effects on efficiency due to mass flow rates were not as prominent as discharge power. Propulsive efficiency seemed to be the same for all mass flow rates. The effects of magnet current on thrust were also investigated. Overall, the results indicated that measured thrust remained fairly constant for magnet currents greater than 1.0A and decreased drastically with lower magnet currents.

### *V.3 Faraday Probe Measurements*

The Faraday probe provided local current density of the beam. Simultaneously, it was used to profile the divergence angles and determine the total beam current. The ExB probe was swept at different mass flow rates while varying discharge voltages from 400V to 80V. The data revealed that the beam's peak-current density increased linearly with discharge voltages. This relationship was observed to occur for all radial distances and for different mass flow rates. The measurements also showed the FWHM decreased exponentially as discharge voltages increased. It suggested that the beam shape narrowed or approached toward an impulse characteristic. Additionally, this research found that various mass flow rates had no effect on FWHM. Lastly, charge exchange was detected at angles around 30-50 degrees. The result was as expected for a typical Hall thruster's plume.

The Faraday probe measurements were also used to calculate the beam efficiency. It describes how efficient the ion flow is exiting the thruster. The results revealed that discharge beam efficiency increases at low discharge voltages and reached its maximum point around 225V. The efficiency remained constant at this maximum value for discharge voltages greater than 225V. Additionally, the results showed different mass flow rates had little effect on beam efficiency.

This experiment also examined the thruster exhaust plume effects of both magnet currents. Overall, the Faraday results indicated that shape of the exhaust beam can be adjusted with various magnet settings. Lower magnet currents created a narrower beam while higher magnet currents caused the beam to diverge. As discharge voltage increased, the beam's FWHM became less sensitive to magnet currents. However, the effects on peak current density were more prominent. For low mass flow rates, the peak current density remained relatively constant for different magnet currents. Only as mass flow rates increased would it be affected by the magnet currents. This research also looked at the effects of magnet current on discharge beam efficiency. Overall, the magnet currents had little or no effect on discharge beam efficiency for different conditions tested. These results are important because they provide an insight into how to make the beam to be closer to an impulse.

#### *V.4 ExB Probe Measurements*

The ExB probe was used to evaluate the ion energy distribution within the plume. Ion species fractions were calculated from the probe measurements. The data yielded species fraction for  $\text{Xe}^{+1}$  seem to make up about 97-82% for discharge voltages from 80-

400V, respectively. Overall, more highly charged species are produced as discharge potential increased for different mass flow rates.

In addition to Faraday probe measurements, this research used the ExB to examine the ion species within the plume shape for various divergence angles. The result showed that the  $\text{Xe}^{+1}$  species was the most prominent in the plume. It peaked near the centerline and decreased as the beam diverges outward. Basically the ion species fractions shifted toward higher charges as the divergence angles moved away from centerline  $-30^\circ$  to  $+30^\circ$ . For divergence angles from  $-30^\circ$  to  $-70^\circ$ , the ion species fractions remained relatively constant. However, the results at wider divergence angles were unexpected. The causes for differences in results could be from sources such as charge exchange, high background pressure, asymmetry in thruster geometry, background environment, effectiveness on the probe, or incompatible math equations.

The effects of magnet current on ion species production were also discussed. Overall, the results indicated that species production shift toward  $\text{Xe}^{+2}$  ions as the current of either or both magnets increased from 0.5-3.0A.

Results from this study validated performance values for the BHT-600W after comparing experimental values with those provided by the manufacturer, Busek Co., and other researchers. The results from the research will hopefully be of use in future developments and will contribute to operational application. The end-user can use this information and its supporting data to develop detailed plans that will meet the various mission constraints.

## Appendix A. Additional Diagnostic Tools

### *Langmuir Probe*

One of the most widely used instruments is the Langmuir probe. The probe measures plasma potential, electron and ion density, electron temperature, and ion flux within the plume. The probe construction is relatively simple because it typically consists mainly of a heated wire and tubing. The schematic for a single probe is illustrated in Figure 76. This exposed wire is usually made from Tungsten or Nickel due to high melting point and conductivity. The wire or electrode is about 0.5 mm in diameter and 4 mm length. This simplification leads to easy construction, low cost, and easy to use.

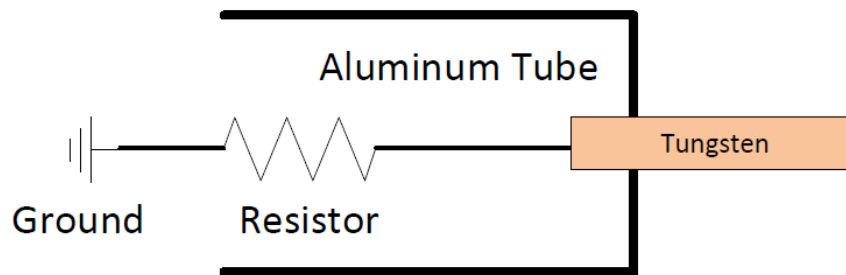


Figure 76: Typical single Langmuir Probe.

There are different types of Langmuir probe developed for analyzing the plasma plume. Most widely used are the Single probe, Double probe, and Triple probe. The basic difference between the three is an additional electrode on the tip. The theory of operation is similar for all cases. Different configurations were developed to address the probe limitation, ambiguity, and especially error sources. Some of these problems include sweep rate, plasma fluctuation, noises, sampling rates, contaminations, and poor resolution.

The basic concept for Langmuir probe use to measure plasma characteristics has remained the same since the 1920s [41]. It is a proven technique and is used extensively in electrical propulsion. Measurement from Langmuir probe was done by applying voltage to the conducting electrode through electrical circuit. This voltage caused the probe to be bias. The electrode then either attracts electrons or ions, depending on the bias voltage, which then induce a current that can be interpreted to the plume properties. The applied voltage or bias voltage is usually slowly swept across a range of interest where each induced current measurement is associated with each apply voltages. This enables the creation of current-voltage (I-V) curve. Typical I-V curve is illustrated in Figure 77. Various plume properties, as stated earlier, can be analyzed by using Langmuir probe theory from the current-voltage trace [17].

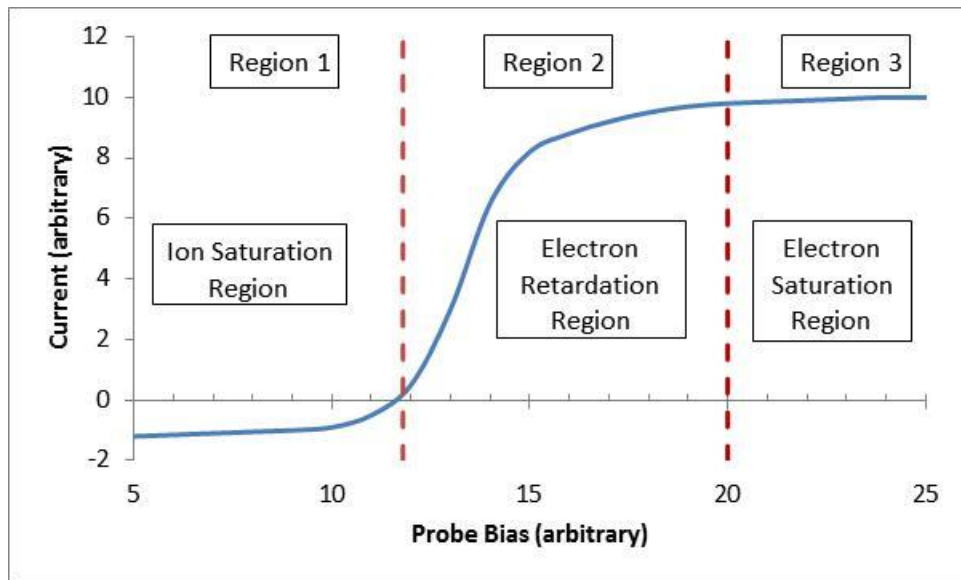


Figure 77: Langmuir probe theoretical result.

The I-V curve is separated into three regions: ion saturation, electron retardation, and electron saturation [41]. The first region is called the ion saturation. The ion current

is calculated from this region because the probe has negative potential relatively to the plume. Negative potential enables the probe to attract positive ions and repel any negative electrons. Ions attracted to the probe induce a current, which yield the plume ion current. Furthermore, when the probe current is zero, this implies that at associated probe voltage is at the plume floating potential.

The middle region of the curve is called electron retardation. Similar to previous region, the ions are attracted to the probe. However, more energetic electrons would overcome the repulsion force and become absorbed by the probe. The current produced by the electrons are called exponential electron current. The measured currents from this region are contributed from both the electrons and ion saturation current. This region enables calculation for the electron temperature, which is given by Equation 47 [41].

$$\frac{1}{k_B T_e} = \frac{I_p}{\int_{V_f}^{V_p} I(V) dV} \quad (47)$$

where  $I_p$  is the measured current associated with plasma potential and  $k_B$  is the Boltzmann constant.  $V_f$  and  $V_p$  are the floating potential and plasma potential, respectively. The plasma potential is determined by the voltage that associates with a peak in I-V curve, i.e. second-derivative is zero. Additionally, ion density could be calculated from the following [41], assuming  $n_e = n_i$ .

$$n_e = \frac{I_p}{A_p} \left( \frac{2\pi m_e}{e^2 k_B T_e} \right)^{1/2} \quad (48)$$

where  $A_p$  is the probe area.

The third region is called electron saturation. It is the region where the probe potential is equal to or greater than the plasma potential. The probe absorbs incoming

electrons because it has positive potential relative to the plume. The current measured from this region would produce a more accurate plasma potential when combining with data from electron retardation region. The new plasma potential is a voltage where the current from electron saturation region intersects with current from electron retardation region. This method is described by Laframboise theory [41]. A more accurate electron temperature and ion density can be calculated with Equation 47 and 48. In practice, it is often difficult to measure the electron saturation current and the error can be as high as 30-50%.

#### *Retarding Potential Analyzer (RPA)*

Another tool used to measure the plume properties is called retarding potential analyzer (RPA). The RPA was developed by Hass which measures the ion energy distribution by examine energy-to-charge ratios [2]. The results from RPA provide the relationship between the probe current produced by the ion and probe applied voltage. The slope of current-voltage (I-V) relationship is proportional to the ion voltage distribution function  $f(V)$ , which is given by the following [15]:

$$\frac{dI}{dV} = \frac{Z^2 e^2 n_i A_c}{m_{Xe}} f(V) \quad (49)$$

where

- $Z$  = Ion charge-state
- $e$  = Elementary charge
- $n_i$  = Ion density
- $A_c$  = Collection surface area
- $m_{Xe}$  = Propellant mass (Xenon)

The technique only examines the energy per charge which inherently cannot distinguish different charge state occurred in the real plume. This produce ambiguity in the measurement because all Xenon Hall thruster will produce different charge state [12, 15]. Additionally, charge exchange outside the plume further skew measurements. As suggested by Hofer, this method must use in combination with other technique to discriminate individual ion charge-state [15].

RPA is constructed with two main components; series of bias grids and ion collectors. The bias grids are usually made up by three and sometimes four grids and are separated by insulators. Each grid acts as high-pass filter that allow ion with specific energy to enter the collector surface where it induce a current. The induced current and applied voltage then can be used for analysis. The schematic for RPA is illustrated in Figure 78.

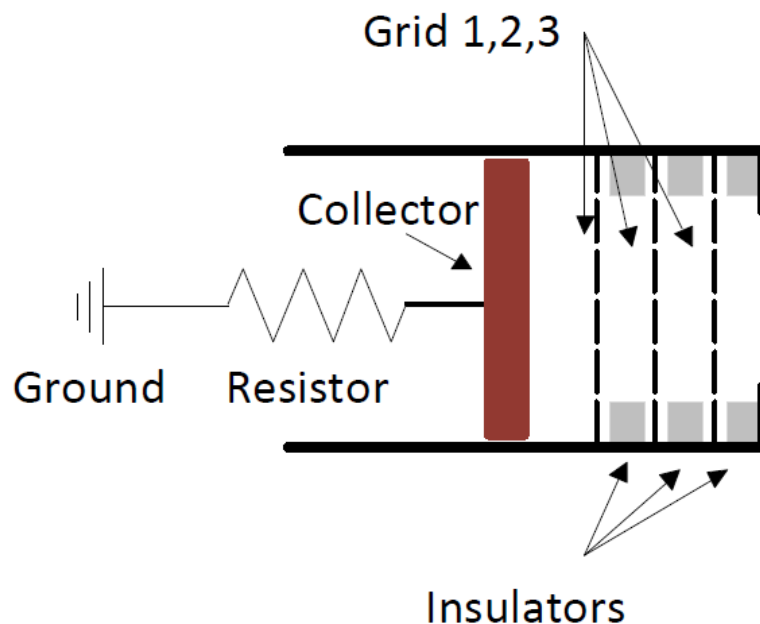


Figure 78: Typical RPA.



The outermost is an attenuation grid [37]. Its function is to reduce the ion flux and maintain local floating potential into the analyzer which ultimately reduces perturbation. The plasma then enters a second grid, which is negatively bias to repel any electron; this ensures only positive ions would enter. The third grid retards any ion with energy per charge that is lower than the grid voltage. The ion that has greater energy per charge would be able to pass the third grid and enter the collector electro to induce a current. The third grid usually sweeps for a range of voltage that would produce current-voltage relationship. A fourth grid is sometimes added to suppress any secondary electron emission because it can reduce the true ion current measurements.

#### *Laser Induced Fluorescence*

Using laser to analyze the plume characteristic is a fairly new technique in plasma diagnostic for electric propulsion. This is an ongoing research and needs to be thoroughly examined. One of such popular methods is called Laser Induced Fluorescence (LIF). It uses light interaction with the plume to characterize the velocity profile and particle density. Basically, light produced from a laser passes through a medium, the plume, where it will be excited. The excitation releases the fluorescence light then collected by a detector. The data then can be used to determine the plume properties. Unlike electrostatic probe, this method is non-intrusive because there are no physical mechanisms that interact with the local flow. The plume remains unperturbed. This is a great tool for an area that is inaccessible by intrusive methods. For example, with an intrusive probe, an area that has high heat flux such as the interior chamber may reduce the probe lifetime and even skew the data with its infringement.

LIF theory and technique has been well developed in other fields and now are being deployed in electric propulsion diagnostic. It was well established that interaction between matter and light must have absorption and emission. Theory for understanding laser diagnostic is through line spectra for absorption and emission of radiance as best described by simple Bohr model for hydrogen [39]. Rather being a wave, here lights are treated as a partial, photon. When light passes through low density gaseous medium, plasma plume for this case, the atoms in the plume absorb incoming light with specific wavelength. This absorption produces a missing wavelength on the line spectra. This wavelength is a unique characteristic for each atom within the plume. LIF basically uses this theory to determine the particle velocity and density.

The density of the plume can be determined by examining the laser intensity. Each atom species has associated wavelength that absorb incoming light that would produce the missing frequency in the line spectra. By tuning the laser with specific wavelength, the associated atom would absorb the laser's energy and reduces its energy. This reduction intensity governs by Beer's law for absorption which is given by Equation 50 and 51 [39].

$$N_i = \frac{\ln \frac{I_0}{I_f}}{\sigma_{abs} l} \quad (50)$$

$$\sigma_{abs} = \frac{A_{21} C^2 g_2}{8\pi f^2 g_1} \quad (51)$$

Where  $I_i$  = initial and final intensity  
 $l$  = path length through absorbing material  
 $\sigma_{abs}$  = cross – sectional area of absorption

$A_{12}$  = Einstein spontaneous emission rate coefficient

$C$  = speed of light

$g_i$  = degeneracy term related to atom transitioning energy levels

$f$  = frequency

These relationships state that the ion density is determined by the change in the laser intensity as it passes through the medium.

Laser Induced Fluorescence technique also provides the plasma plume velocity profile by using Doppler's shift principle. As stated earlier, an atom absorbs light emitted from a laser. According to the Bohr model, if an atom absorbs enough energy, it is in an "excited" state. The atom would want to be in its natural state and therefore has to release photon or emit light with specific wavelength with corresponding energy drop. This phenomenon is called fluorescence [39]. If the plasma plume is in motion, the light detected from it will have different frequency. This change in frequency due to moving body is governed by Doppler's shift, giving in Equation 52 [39].

$$\Delta f = \pm f_0 \frac{v}{c} \quad (52)$$

where  $v$  is the particle velocity and  $f_0$  is the original frequency. Similarly to sound, the frequency increases as the particle move toward the "observer." The opposite occurs when the particle move away from the "observer." The relationship given by Equation 52 would yield the plasma plume velocity profile. LIF is a great diagnostic tool because it provides detailed description of the plume. However, it is complicated to perform.

## Appendix B. Additional Faraday measurements

Figure 79-81 plot the peak current density and FWHM as a function of discharge voltages at five different mass flow rates. It also illustrates exhaust beam structure in the form of its peak current density and FWHM for various operating conditions. The data revealed that the beam peak current density increased linearly with discharge voltages. This relationship was observed to occur for different mass flow rates and radial distance of 50cm, 60cm, and 70cm.

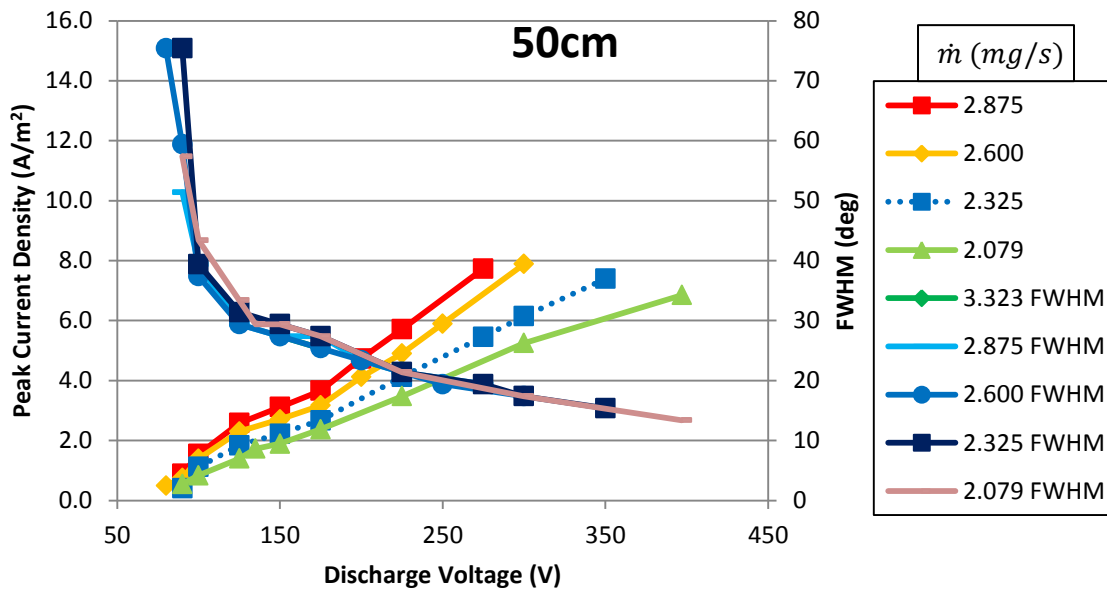


Figure 79: Faraday sweep at 50cm radial distance.

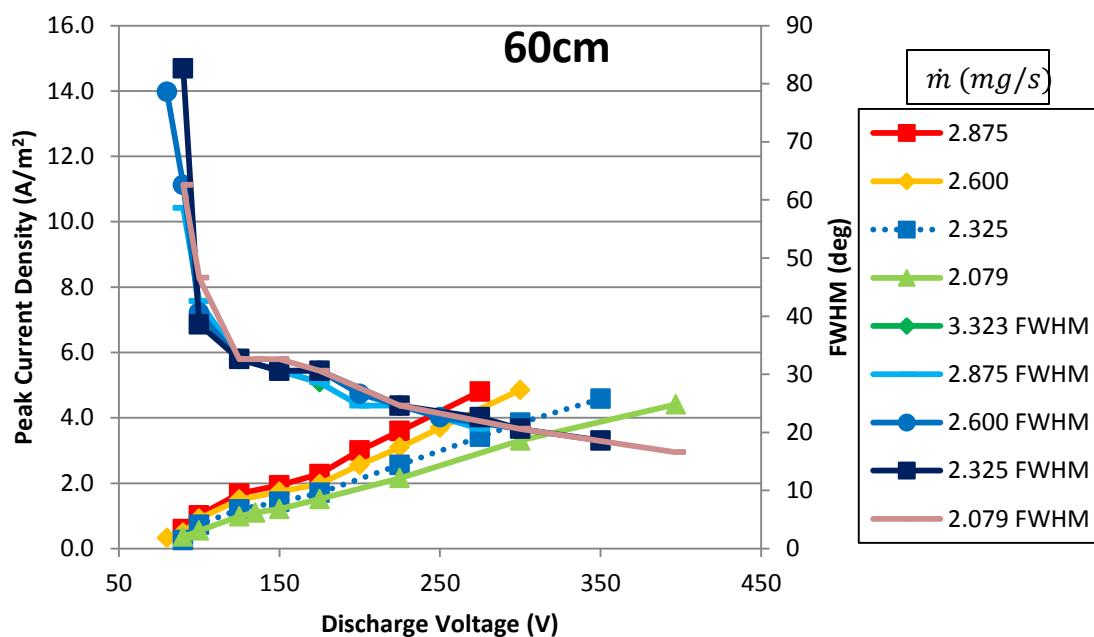


Figure 80: Faraday sweep at 60cm radial distance.

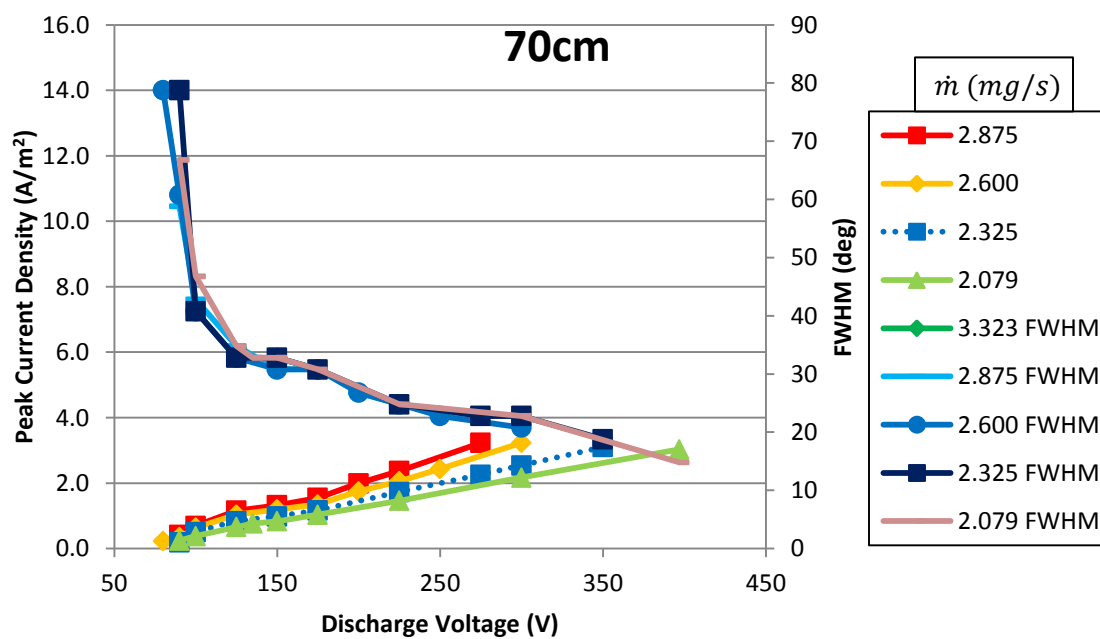


Figure 81: Faraday sweep at 70cm radial distance.

The beam efficiency is given by the beam current and discharge current. It describes how efficiently the ion flow is exiting the thruster. This quantity was calculated for discharge voltage from 60-400V at five different mass flow rates. Figure 82, 83, and 84 show the discharge beam efficiency as a function of discharge voltage for various mass flow rates at 50cm, 60cm, and 70cm radial distances from the thruster, respectively.

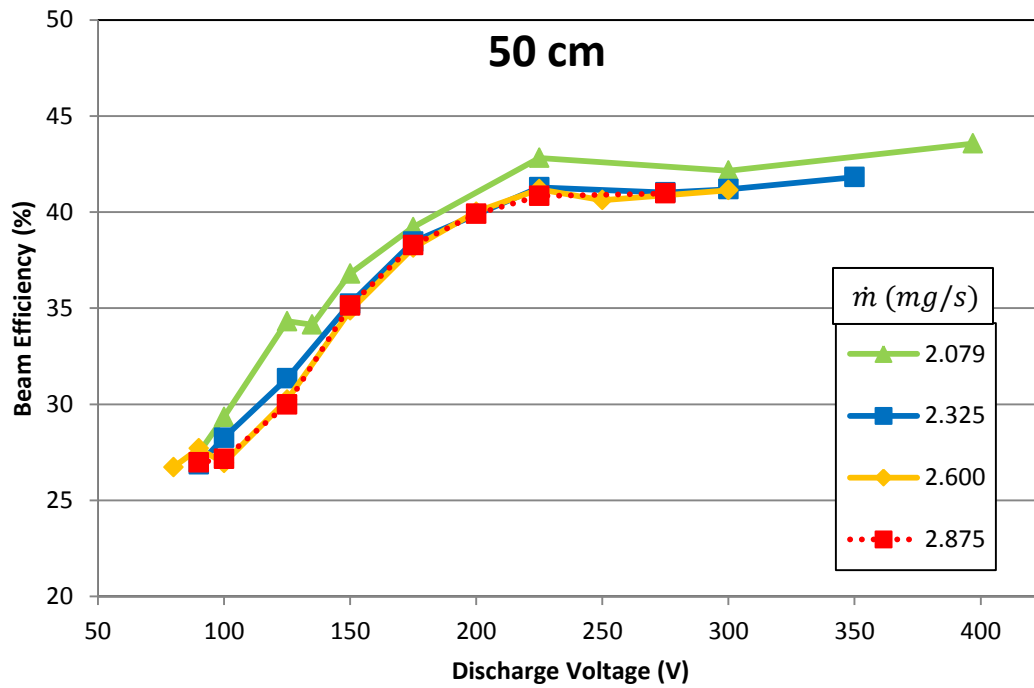


Figure 82: Beam efficiency at 50cm radial distance.

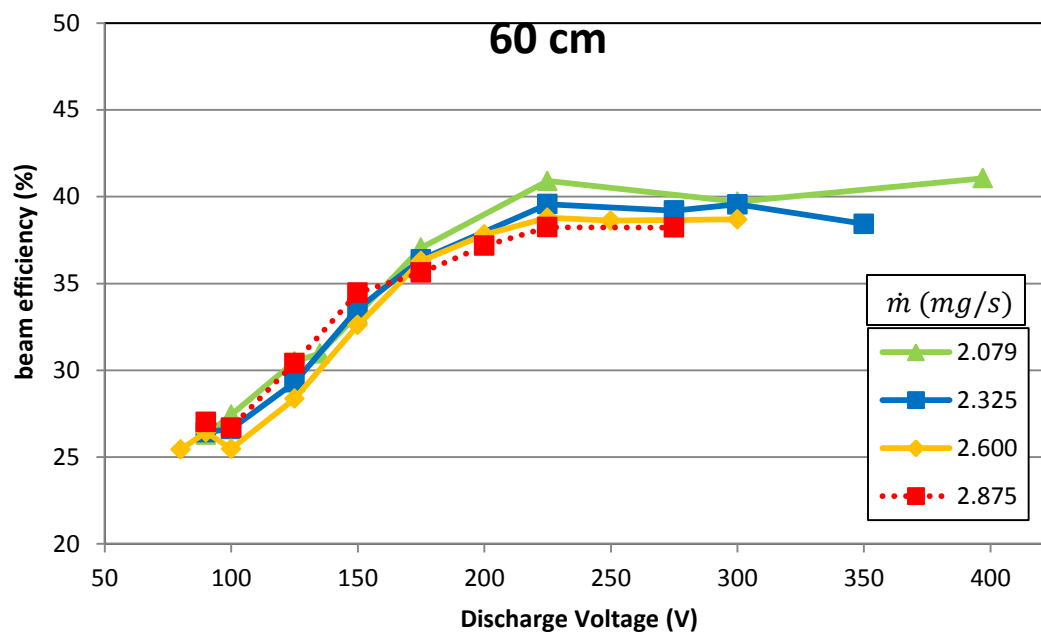


Figure 83: Beam efficiency at 60cm radial distance.

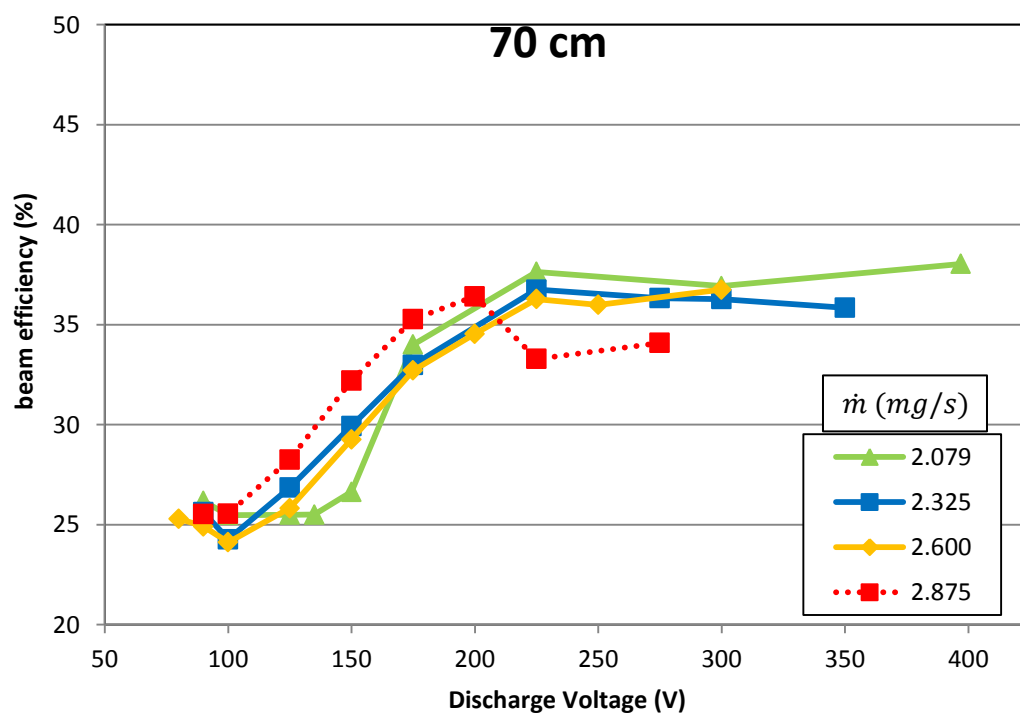


Figure 84: Beam efficiency at 70cm radial distance.

The effects of magnet current on plume shape for mass flow rate of 2.600mg/s and 3.092mg/s are presented in Figure 85 and 88. The figures illustrate the effects on peak current density and FWHM from magnets current at various mass flow rates and discharge voltages. Overall, the results indicated that shape of the exhaust beam can be adjusted with various magnet settings. The optimal point seems to occur around magnets current of 1.0A.

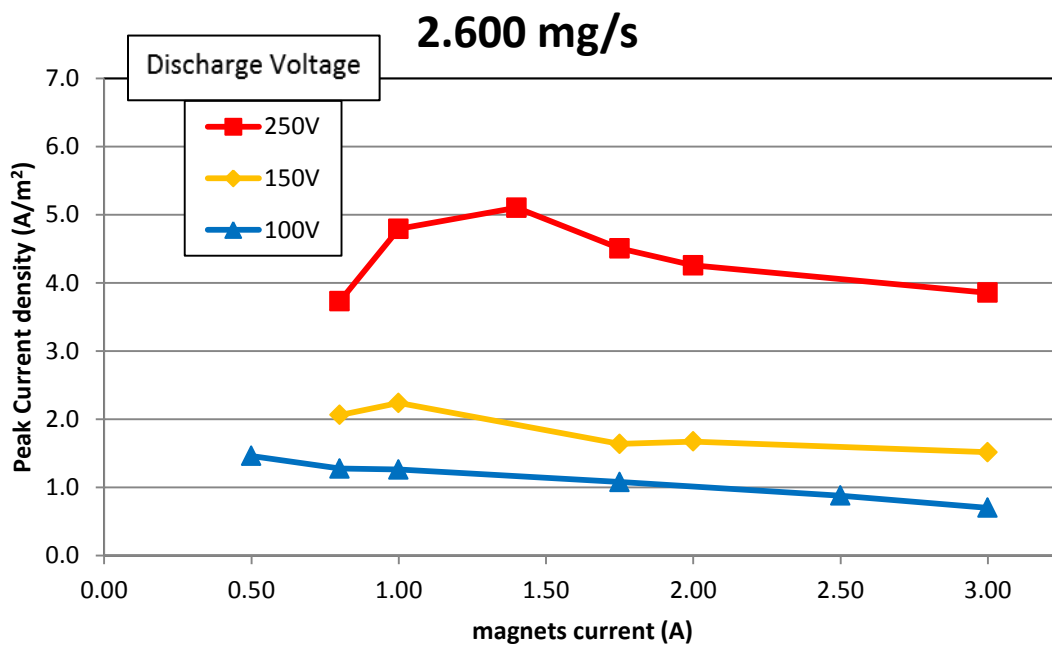


Figure 85: Magnets effects on peak current density.



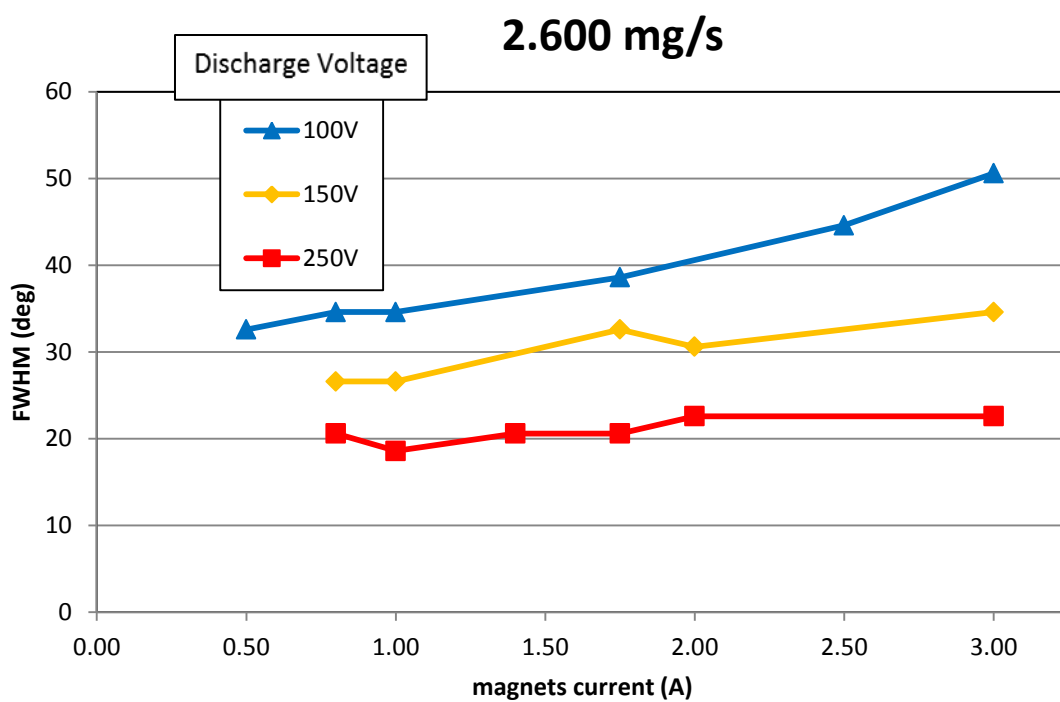


Figure 86: Magnets effects on FWHM.

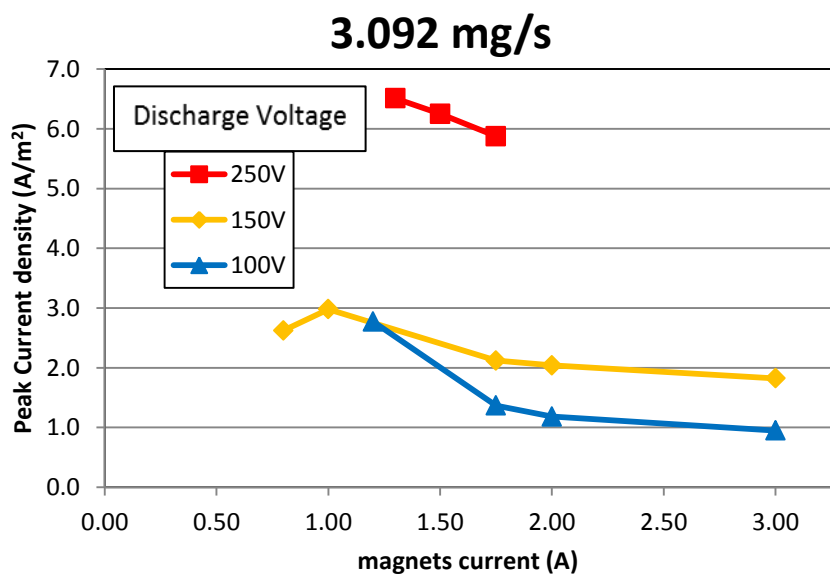


Figure 87: Magnets effects on peak current density.

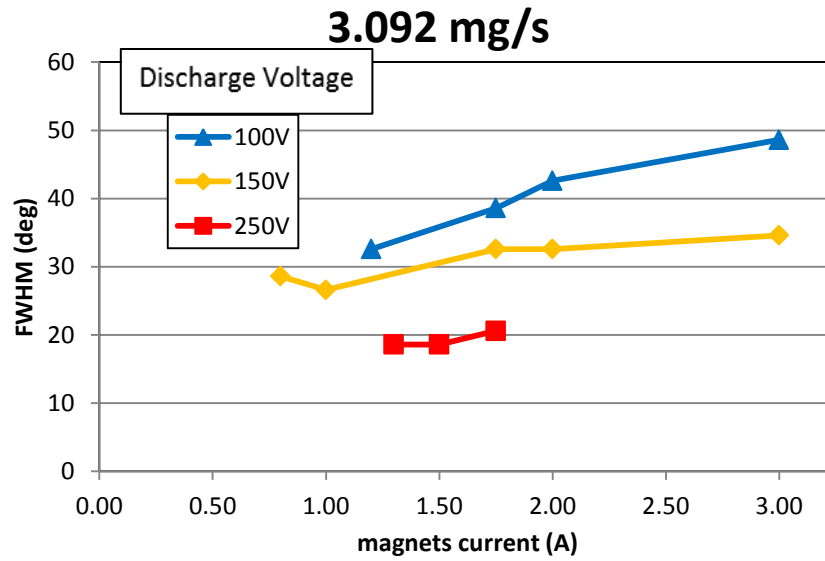


Figure 88: Magnets effects on FWHM.

The peak current density and FWHM as a function of *inner* magnet currents for various mass flow rates, 2.600mg/s and 3.092mg/s, and discharge voltages are presented in Figure 89 and 92 below. At mass flow rates of 2.600mg/s, it can easily be seen that there is a maximum peak-current density at low inner magnet settings. It located at 1.0A in Figure 89 and around 0.5A in Figure 91. The opposite effect was observed at the same locations for FWHM. At higher mass flow rates in Figure 91, the plume shape highly affected by inner magnet settings, especially at 100V discharge voltage. This is the region that borders with the current limit mode, so high fluctuation in plume shape is expected.

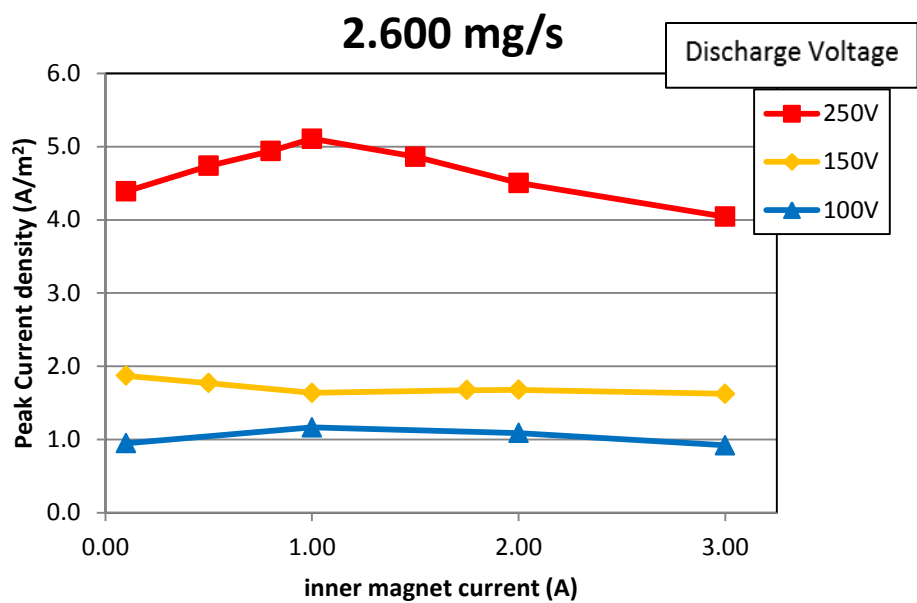


Figure 89: Inner magnets effects on peak current density.

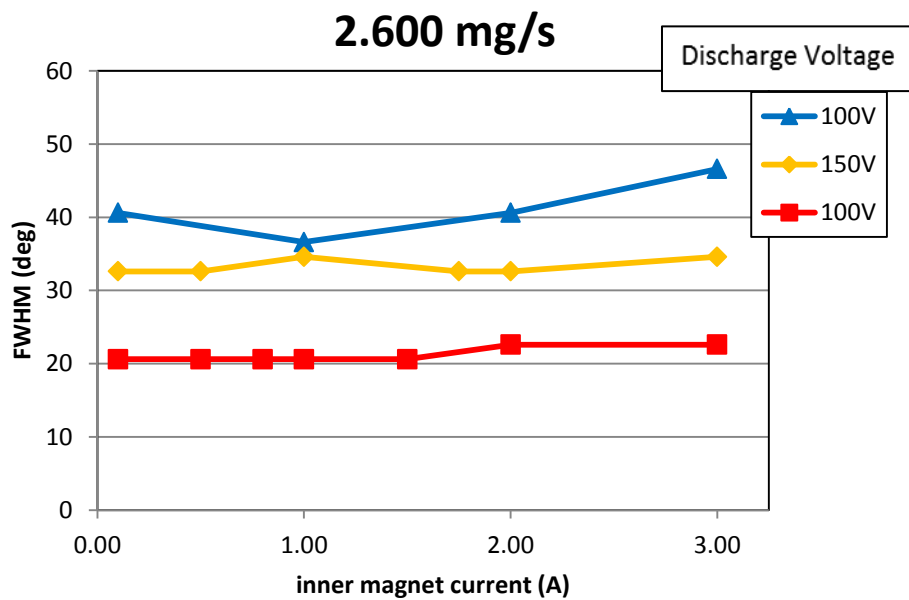


Figure 90: Inner magnets effects on FWHM.

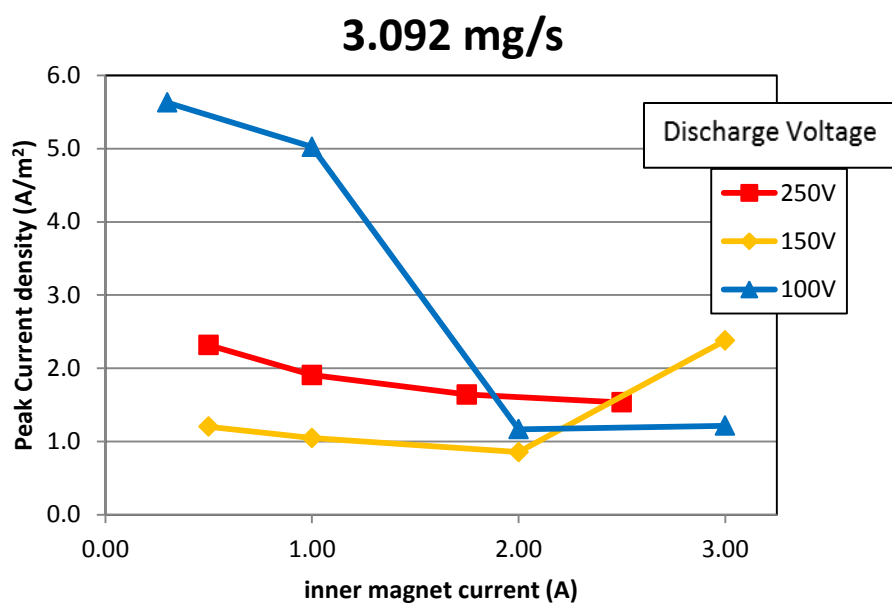


Figure 91: Inner magnets effects on peak current density.

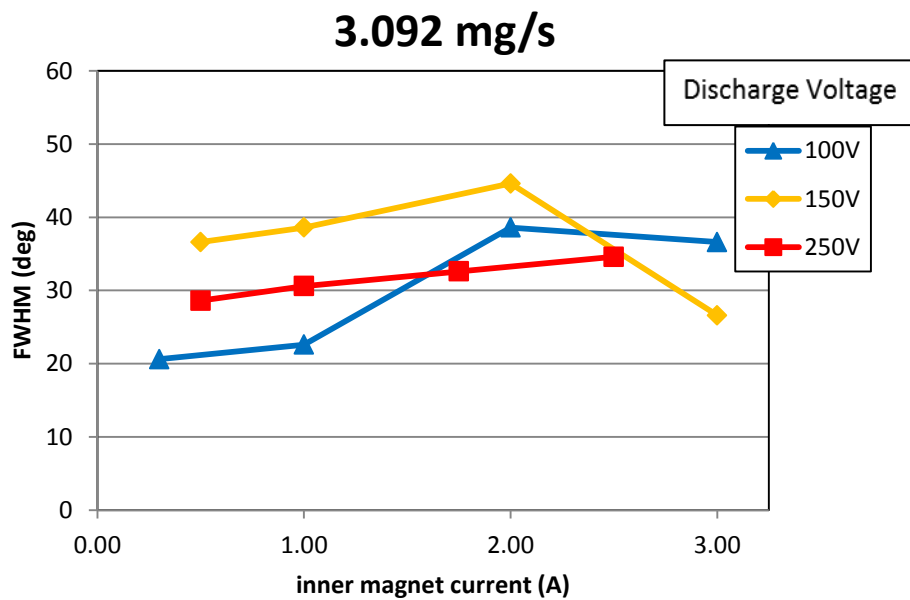


Figure 92: Inner magnets effects on FWHM.

### Appendix C. Additional ExB measurements

The voltage sweep for different operating conditions are presented in Figure 93 through 97 below. The probe was fixed 60cm from the thruster while the voltage was swept from 0V to 50V, which should account for all major xenon species regularly found in hall thruster's plume. The plot shows three distinct peaks, which represent energy for three different xenon species.

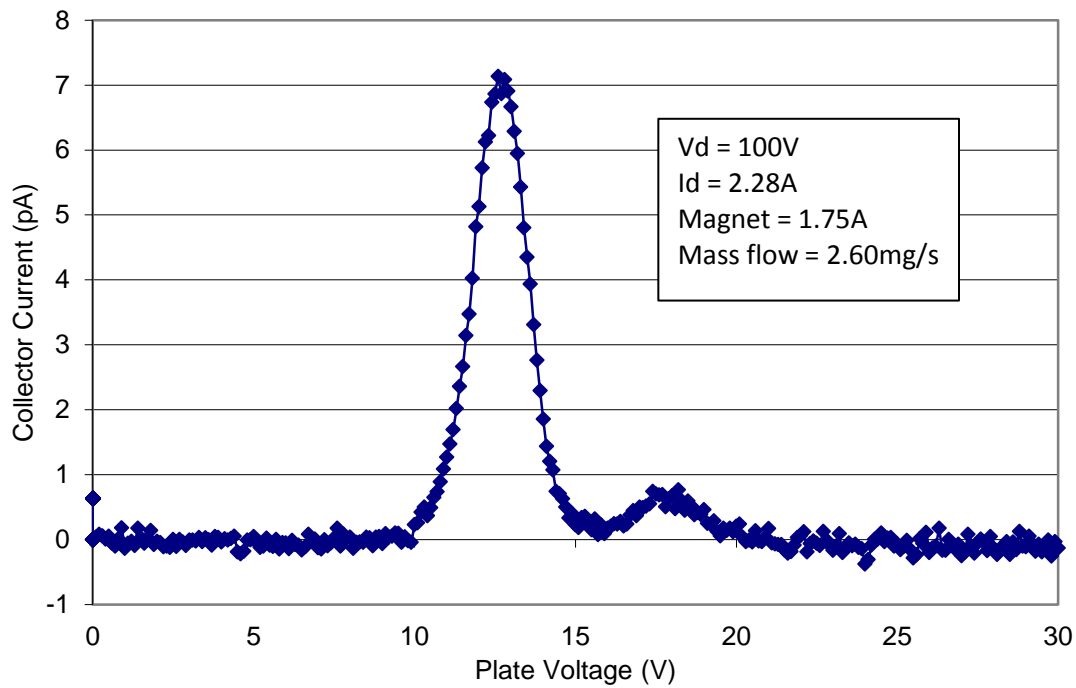


Figure 93: ExB swept for Vd=100V, Id=2.28A, mass flow = 2.60mg/sec.

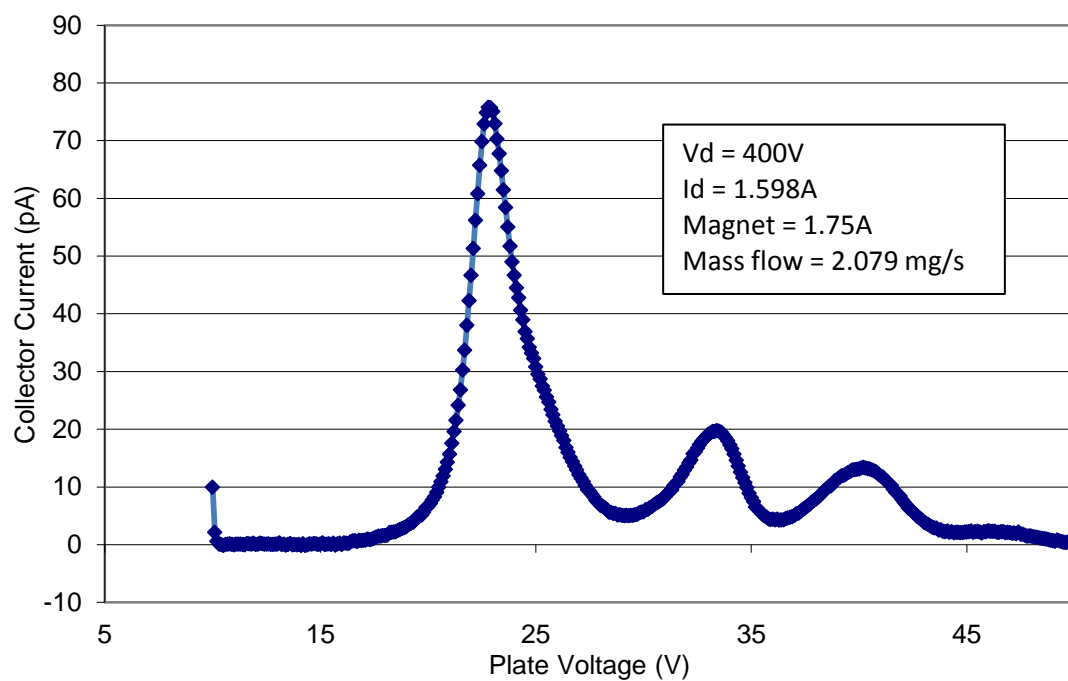


Figure 94: ExB swept for Vd = 400V, Id = 1.598A, mass flow = 2.079mg/sec.

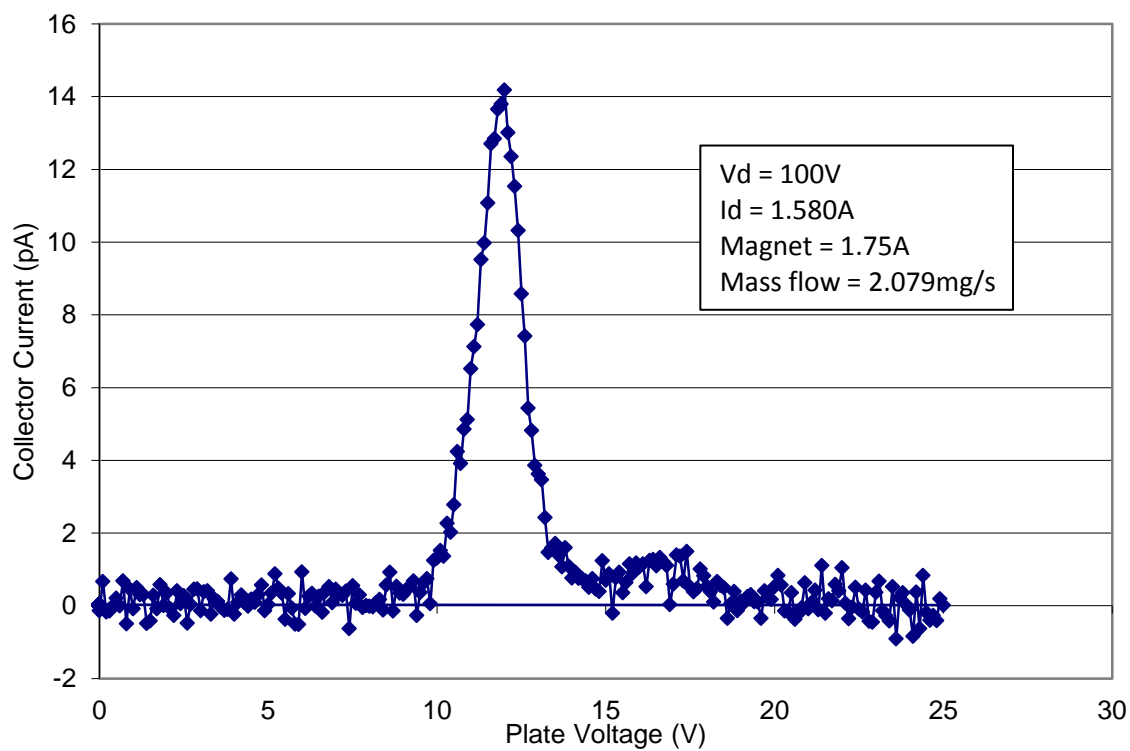


Figure 95: ExB swept for Vd = 100V, Id = 1.58A, mass flow = 2.079mg/sec.

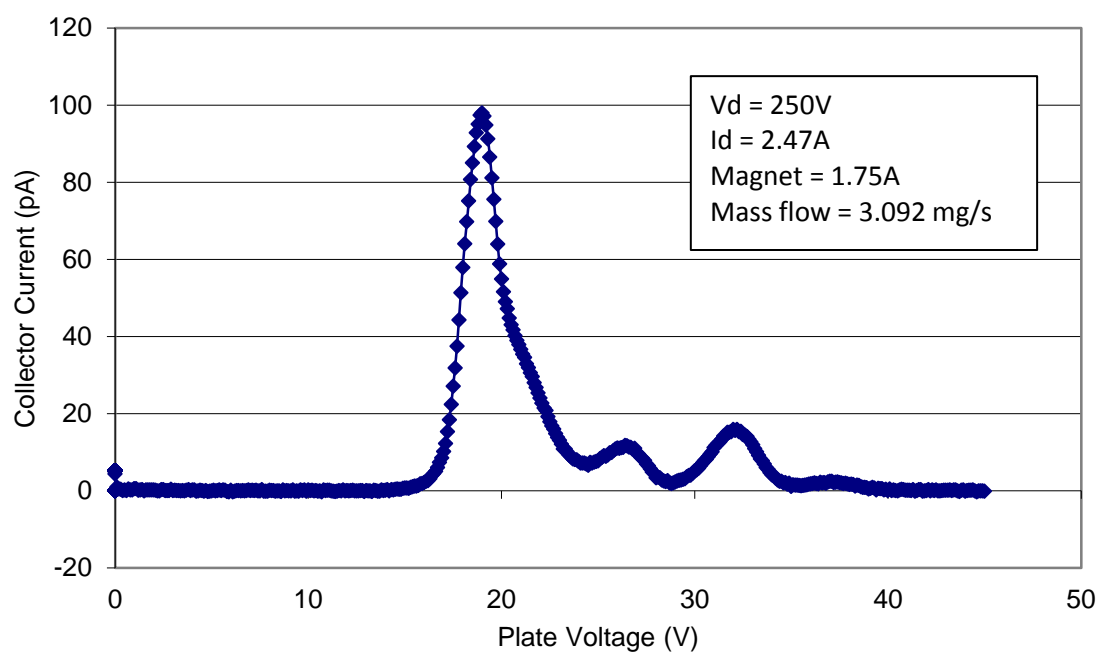


Figure 96: ExB swept for  $V_d = 250\text{V}$ ,  $I_d = 2.47\text{A}$ , mass flow = 3.092mg/sec.

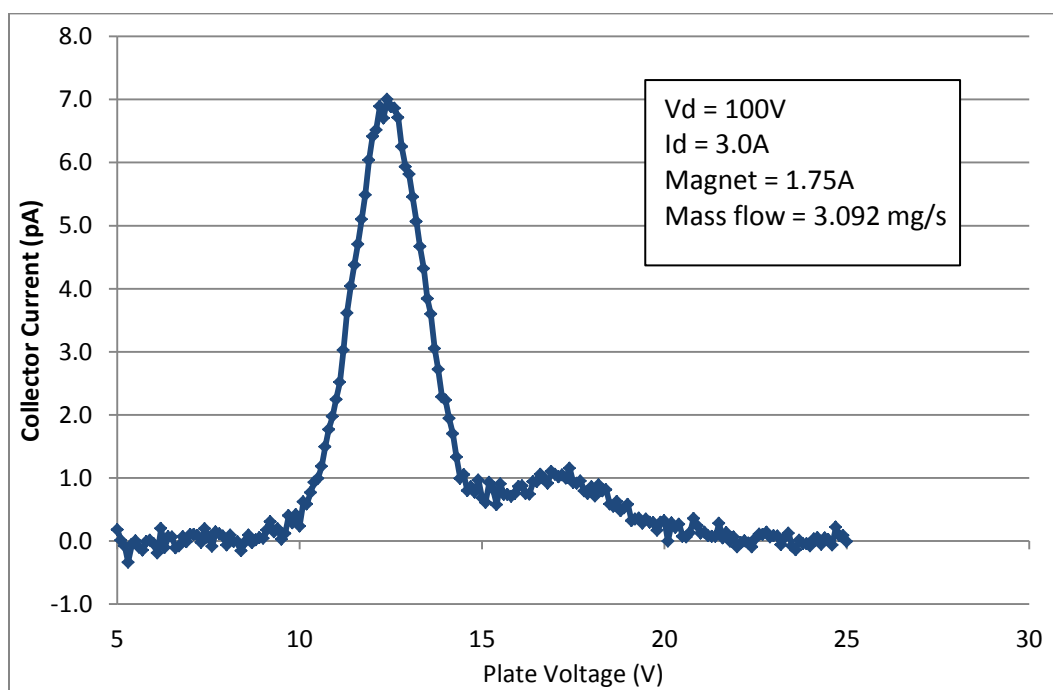


Figure 97: ExB swept for  $V_d = 100\text{V}$ ,  $I_d = 3.0\text{A}$ , mass flow = 3.092mg/sec.

The plot of species fraction versus discharge power is presented in Figure 98. It shows different xenon species fraction as a function of discharge power at five different mass flow rates. Overall, the data clearly showed that more highly charged species were produced as discharge potential increased.

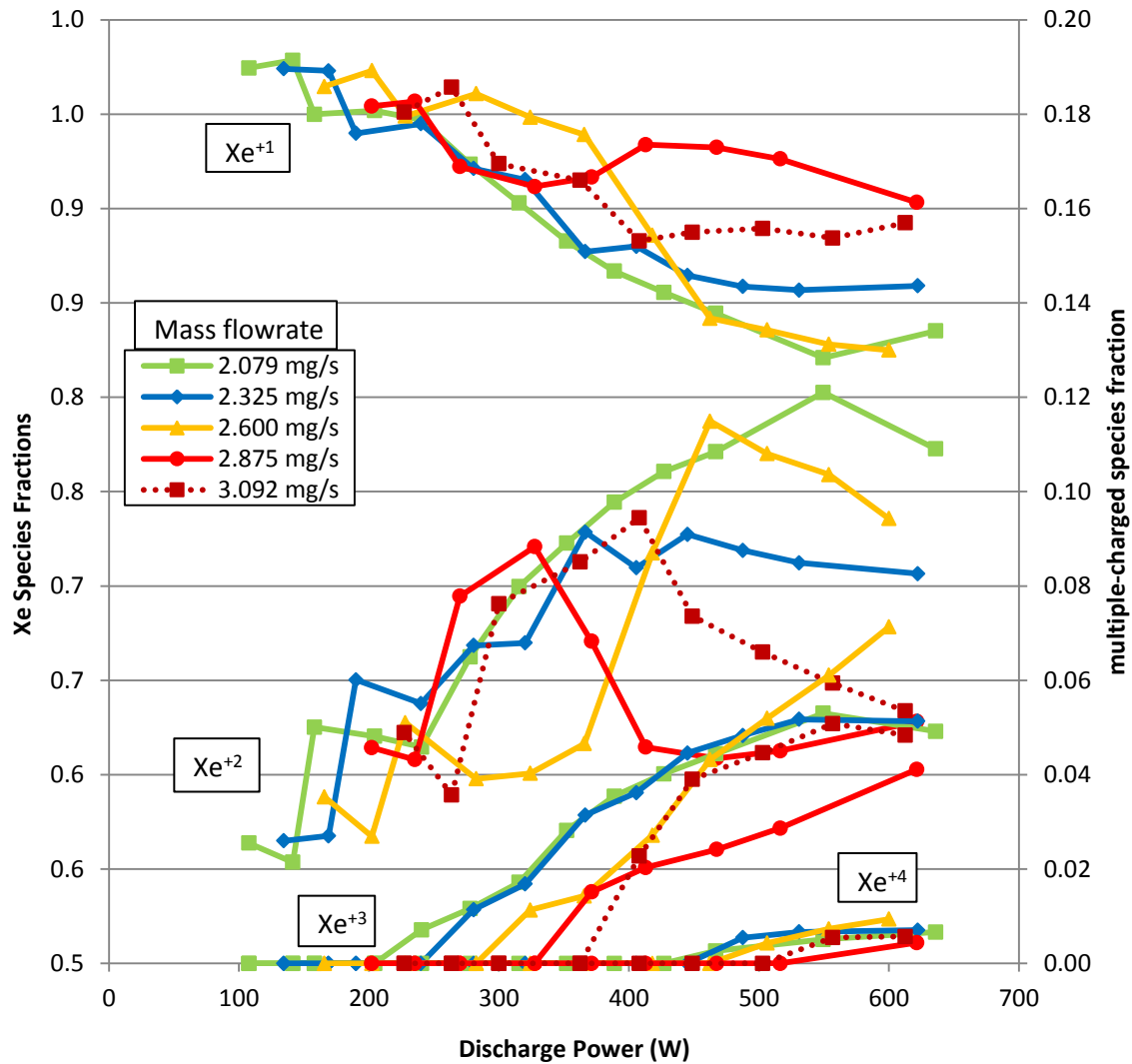


Figure 98: Xe species fractions for various operating conditions.

The effects of magnet current on ion species productions are presented in Figure 99. The figure illustrates the effects on xenon species from both magnet currents at



various discharge voltage and mass flow rate of 2.600mg/s. The overall results indicated that species production shift toward  $\text{Xe}^{+2}$  ions as the current of both magnets increased from 0.5-3.0A.

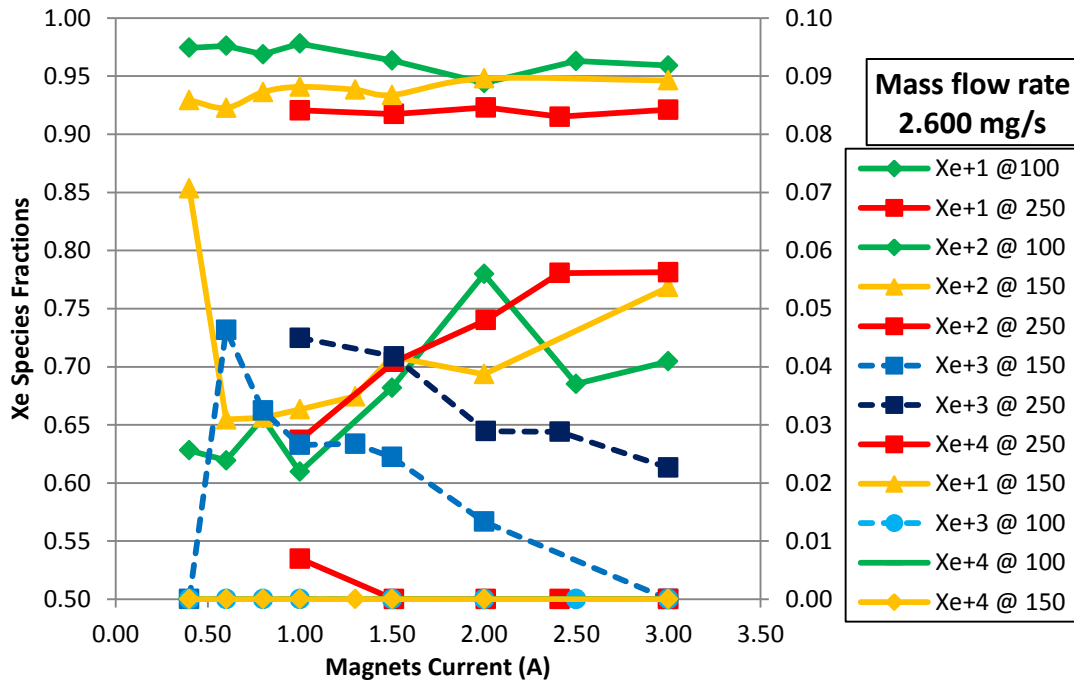


Figure 99: Both magnets current effects on Xe fraction for mass flow = 2.6mg/s.

The effects of outer magnet current on ion species productions are presented in Figure 100. The data is for condition at constant mass flow rate of 2.600mg/s while varying discharge voltages at 100V, 150V, and 250V. The overall results indicated a species production shift toward  $\text{Xe}^{+2}$  ions as outer magnet current increased from 0.5-3.0A. The results also showed that the user has the capability to regulate production of ion species with outer magnet current

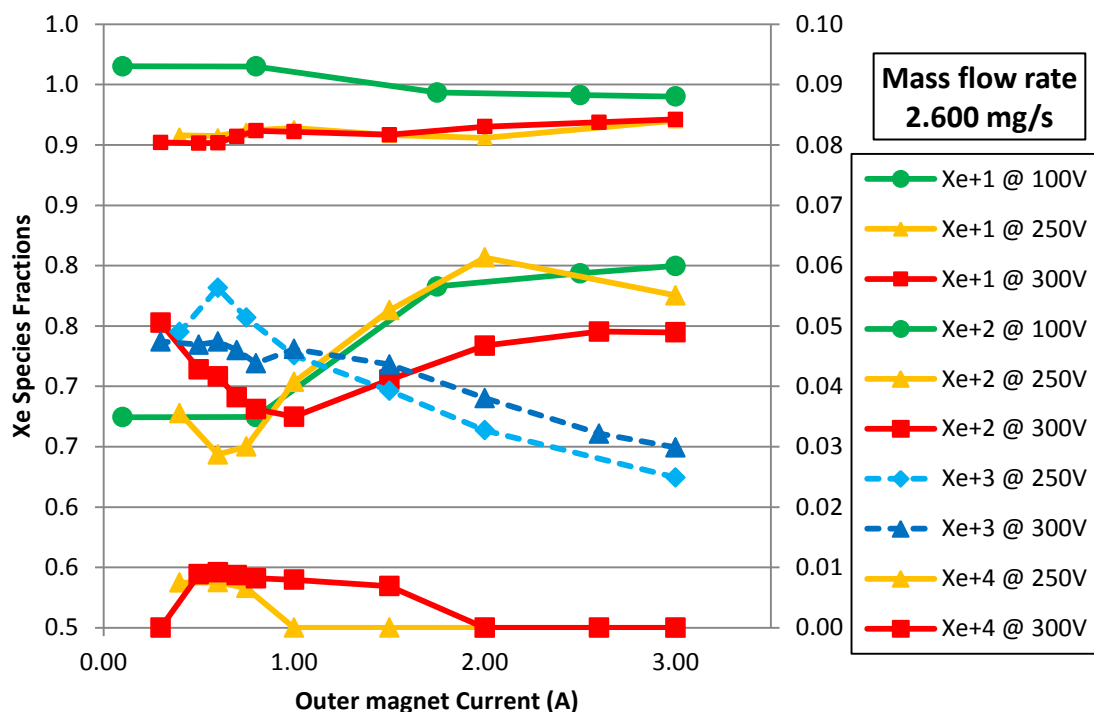


Figure 100: Outer magnets current effects on Xe fraction for mass flow = 2.6mg/s.

The effects of inner magnet current on ion species productions are presented in Figure 101. The figure illustrates the effects on xenon species from inner magnet currents at various discharge voltage and constant mass flow rate of 2.600mg/s. The plot shows that species production shift toward  $\text{Xe}^{+2}$  ions as current of the inner magnets increased from 0.5-3.0A. The number of  $\text{Xe}^{+3}$  and  $\text{Xe}^{+4}$  decreased with higher magnet current while  $\text{Xe}^{+2}$  productions increased. The  $\text{Xe}^{+1}$  species remained constant for different inner magnet currents. The inner magnet current also has the ability to regulate ion species production.

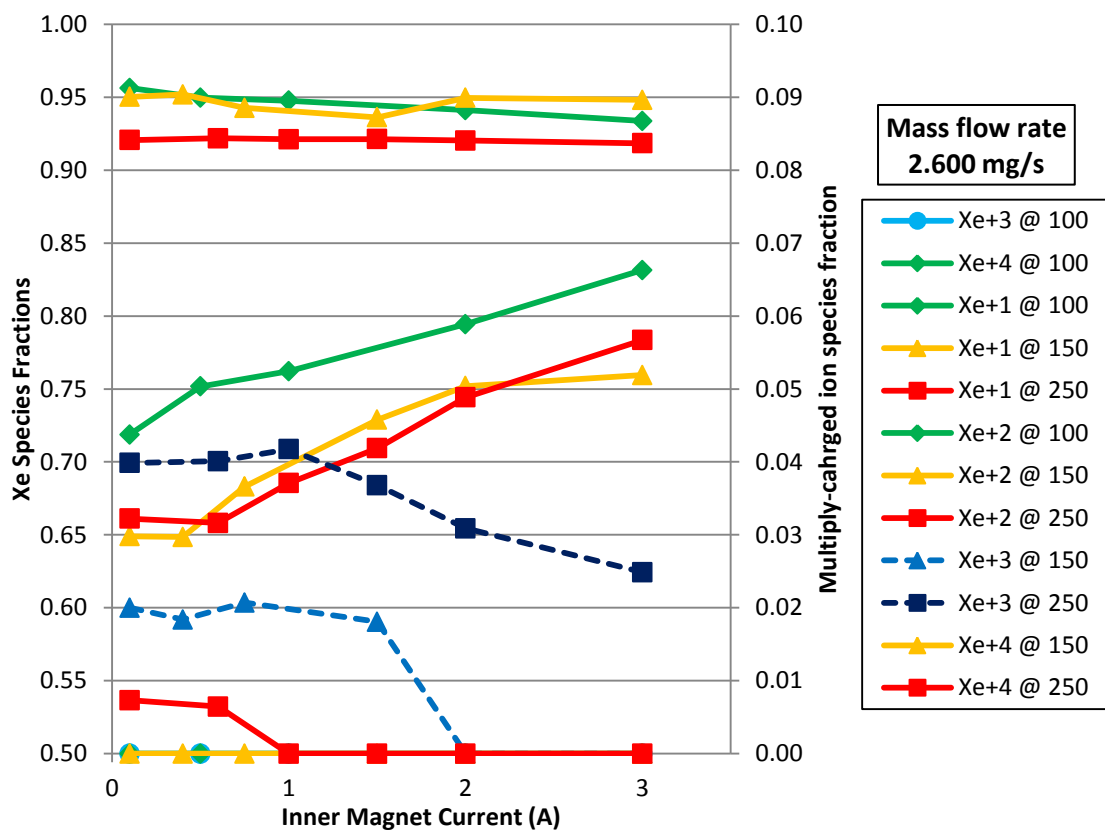


Figure 101: Inner magnets current effects on Xe fraction for mass flow = 2.6mg/s.

## Bibliography

- [1]Victor, A., Zurbuchen, T., Gallimore, A., “The Top Hat Electric Propulsion Plume Analyzer (TOPAZ): Preliminary Data on the BHT600 Cluster,” AIAA 2005-3870, *41<sup>st</sup> Joint Propulsion Conference & Exhibit*, Tucson, Arizona, July 10-13, 2005.
- [2]Ekholm, J., Hargus, W., Larson, C., “Plume Characteristics of the Busek 600 W Hall Thruster,” AIAA 2006-4659, *42<sup>nd</sup> Joint Propulsion Conference & Exhibit*, Sacramento, CA, July 9-12, 2006.
- [3]Niemela, C., Brieda, L., Nakles, M., Ekholm, J., Hargus, W., “Comparison of Hall Thruster Plume Expansion Model with Experimental Data,” AIAA 2006-4480, *42<sup>nd</sup> Joint Propulsion Conference & Exhibit*, Sacramento, CA, July 9-12, 2006.
- [4]Spicer, R., Wang, J., Brieda, L., “A Study of Particle Collisions in Electric Propulsion Plasma Plumes,” *42<sup>nd</sup> Joint Propulsion Conference & Exhibit*, Sacramento, CA, July 9-12, 2006.
- [5]Matlock, T., Hargus, W., Larson, C., “Thermographic Characterization and Comparison of 200W and 600W Hall Thrusters,” AIAA 2007-5241, *43<sup>rd</sup> Joint Propulsion Conference & Exhibit*, Cincinnati, OH, July 8-11, 2007.
- [6]Hargus, W., Larson, C., Brown, D., “Thrust Efficiency, Energy Efficiency and the Role of VDF in Hall Thruster Performance Analysis,” AIAA 2007-5270, *43<sup>rd</sup> Joint Propulsion Conference & Exhibit*, Cincinnati, OH, July 8-11, 2007.
- [7]Lobbia, R., Gallimore, A., “A Method of Measuring Transient Plume Properties,” AIAA 2008-4650, *44<sup>nd</sup> Joint Propulsion Conference & Exhibit*, Hartford, CT, July 21-23, 2008.
- [8]Hargus, W., Nakles, M., Tedrake, R., Pote, B., “Effect of Anode Current Fluctuations on Ion Energy Distributions within a 600 W Hall Effect Thruster,” AIAA 2008-4724, *44<sup>nd</sup> Joint Propulsion Conference & Exhibit*, Hartford, CT, July 21-23, 2008.
- [9]Hargus, W., Nakles, M., “Background Pressure Effects on Internal and Near-field Ion Velocity Distribution of the BHT-600 Hall Thruster,” AIAA 2008-5101, *44<sup>nd</sup> Joint Propulsion Conference & Exhibit*, Hartford, CT, July 21-23, 2008.
- [10]Hargus, W., Charles, C., “Near-Plume Laser-Induced Fluorescence Velocity Measurements of a Medium Power Hall Thruster,” *Journal of Propulsion and Power*, Vol. 26, No. 1, January-February 2010.

- [11]Cheng, S., Martinez-Sanchez, M., “Hybrid Particle-in-Cell Erosion Modeling of Two Hall Thrusters,” *Journal of Propulsion and Power*, Vol. 24, No. 5, September-October 2008.
- [12]Nakles, M., Barry, R., Larson, C., Hargus, W., “A Plume Comparison of Xenon and Krypton Propellant on a 600 W Hall Thruster,” 31<sup>st</sup> International Electric Propulsion Conference, Ann Arbor, MI, September 20-24, 2009.
- [13]Tomaszewski, J., Branam, R., Hargus, W., Matlock, T., “Characterization of a Hall Effect Thruster Using Thermal Imaging,” Air Force Institute of Technology, Dayton, OH, Master’s Thesis AFIT/GA/ENY/07- , March 2007.
- [14]Bohnert, A., "Thermal Characterization of a Hall Effect Thruster," Air Force Institute of Technology, Dayton, OH, Master's Thesis AFIT/GA/ENY/08-M01, March 2008.
- [15]Hofer, R., “Development and Characterization of High-Efficiency, High-Specific Impulse Xenon Hall Thrusters,” Ph.D. Dissertation, NASA/CR-2004-213099, June 2004.
- [16]Jordan, I., “Electric propulsion: Which One for my Spacecraft?,” Whiting School of Engineering, Dec 6, 2000.
- [17]Kim, S., Gallimore, A., “Plume Study of A 1.35 KW SPT-100 Using An ExB Probe,” AIAA-99-2423, 35<sup>th</sup> *Joint Propulsion Conference & Exhibit*, Los Angeles, CA, June 20-24, 1999.
- [18]Haag, T., “Design of a Thrust Stand for High Power Electric Propulsion Devices,” AIAA-89-2829, 25<sup>th</sup> *Joint Propulsion Conference*, Monterey, CA, July 10-12, 1989.
- [19]Azziz, Y., “Experimental and Theoretical Characterization of a Hall Thruster Plume,” Ph. D. Dissertation, Department of Aeronautics and Astronautics, Massachusetts Institute of Technology, Boston, MA, 2007.
- [20]Hofer, R., Gallimore, A., “Ion Species Fractions in the Far-Field Plume of a High-Specific Impulse Hall Thruster,” AIAA 2003-5001, 39<sup>th</sup> *Joint Propulsion Conference & Exhibit*, Huntsville, AL 20-23 July, 2003.
- [21]Hofer, R., Shastry, R., Reid, B., Gallimore, A., “Method for Analyzing ExB Probe Spectra from Hall Thruster Plumes,” AIAA 2008-4647, 44<sup>th</sup> *Joint Propulsion Conference & Exhibit*, Hartford, CT, July 21-23, 2008.

- [22]Ekholm, J., Hargus, W., "ExB Measurements of a 200 W Xenon Hall Thruster," *Journal of Propulsion and Power*, 2007.
- [23]Brown, D., Gallimore, A., "Evaluation of Plume Divergence and Facility Effects on Far-Field Faraday Probe Current Density Profiles," IEPC-2009-030, Proceedings of the 31<sup>st</sup> International Electric Propulsion Conference, Ann Arbor, MI, September 20-24, 2009.
- [24]Rovey, J., Walker, M., Gallimore, A., Peterson, P., "Magnetically Filtered Faraday Probe for Measuring the Ion Current Density Profile of a Hall Thruster," *Review of Scientific Instruments*, Vol. 77, Number 1, Jan 2006.
- [25]Kodys, A., Cassady, L., Choueiri, E., "Thermal Effects on Inverted Pendulum Thrust Stands for Steady-state High-Power Plasma thrusters," AIAA 2003-4842, 39<sup>th</sup> *Joint Propulsion Conference & Exhibit*, Huntsville, AL, 20-23 July 2003.
- [26]Kodys, A., Murray, R., Cassay, A., Choueiri, E., "An Inverted-Pendulum Thrust Stand for High-Power Electric Thrusters," AIAA 2006-4821, 42<sup>nd</sup> *Joint Propulsion Conference & Exhibit*, Sacramento, CA, July 9-12, 2006.
- [27]Longmier, B., Bering, E., Gallimore, A., Reid, B., Squire, J., Glover, T., Chang-Diaz, F., Brukardt, M., "Hall Thruster and VASIMR VX-100 Force Measurements Using A Plasma Momentum Flux Sensor," AIAA 2009-246, 47<sup>th</sup> *Joint Propulsion Conference & Exhibit*, Orlando, FL, 5-8 January 2009.
- [28]Moeller, T., Polzin, K., "Thrust stand for vertically Oriented electric propulsion performance evaluation," AIAA 2010-7017, 46<sup>th</sup> *Joint Propulsion Conference & Exhibit*, Nashville, TN, 25-28 July 2010.
- [29]Polzin, K., Markusic, T. Boris, S. Dehoyos, A., Spaun, B., "Thrust Stand for Electric Propulsion Performance Evaluation," NASA Marshall Space Flight Center, Huntsville, AL.
- [30]Xu, K., Walker, M., "High-Power, null-type, inverted pendulum thrust stand," *Review of Scientific Instruments*, Vol. 80, Number 5, May 2009.
- [31]Goebel, D., Katz, I., "*Fundamentals of Electric Propulsion: Ion and Hall Thrusters*," 1st ed. Hoboken, NJ: John Wiley & Sons, 2008.
- [32]Humble, R., Henry, G., and Larson, W., Eds., *Space Propulsion Analysis and Design*, 1st ed. New York, NY: McGraw Hill, 1995.

- [33]Busek Co. Inc. (2006), “BHT-600,” *Busek Co. Inc. - Hall Effect Thrusters*. [online database]. URL: <http://www.busek.com/halleffect.html> [cited 14 Apr 2011].
- [34]J. R. Wertz and W. J. Larson, *Space Mission Analysis and Design*, 3rd ed. New York: Space Technology Library, 2008.
- [35]Hillier, Adam, “Revolutionizing Space Propulsion Through the Characterization of Iodine as Fuel for Hall-Effect Thrusters,” Air Force Institute of Technology, Dayton, OH, Master’s Thesis AFIT/GA/ENY/11-M08 , March 2011.
- [36]de La Harpe, John-David, “Performance Characterization of a Novel Plasma Thruster to Provide a Revolutionary Operationally Responsive Space Capability with Micro and Nano Satellites,” Air Force Institute of Technology, Dayton, OH, Master’s Thesis AFIT/GA/ENY/11-M02 , March 2011.
- [37]Department of Aerospace Engineering, “PEPL Plasma Diagnostics,” PEPL: Diagnostics. [online database]. URL: <http://pepl.engin.umich.edu/diagnostics.html> [cited 14 Apr 2011].
- [38]Thuman, J, “Hall Thruster Plume Diagnostics Utilizing Microwave Interferometry,” Air Force Institute of Technology, Dayton, OH, Master’s Thesis AFIT/GA/ENY/08-S03 , September 2008.
- [39]Lee, Daniel, “Velocity Plume Profiles for Hall Thrusters Using Laser Diagnostics,” Air Force Institute of Technology, Dayton, OH, Master’s Thesis AFIT/GA/ENY/10-J01, Jan 2010.
- [40]Choueiri, E., “A Critical History of Electric Propulsion: The First Fifty Years (1906-1956),” AIAA 2004-3334, *40<sup>th</sup> Joint Propulsion Conference & Exhibit*, Ft. Lauderdale, FL, 2004.
- [41]Rotter, John, “An Analysis of Multiple Configurations of Next-Generation Cathodes in a Low Power Hall Thruster,” Air Force Institute of Technology, Dayton, OH, Master’s Thesis AFIT/GA/ENY/09-M07, March 2007.
- [42]Hruby, Vlad, “Review of Electric Propulsion Activities in the US Industry,” AIAA 2003-4441, *39<sup>th</sup> Joint Propulsion Conference & Exhibit*, Huntsville, AL, 20-23 July 2003.
- [43]Lichtin, Daniel, “An Overview of Electric Propulsion Activities in US Industry – 2005,” AIAA 2005-3532, *41<sup>st</sup> Joint Propulsion Conference & Exhibit*, Tucson, AZ, 10-13 July 2005.

- [44]Oleson, Steven, “Electric Propulsion for Low Earth Orbit Constellations”, NASA/TM-1998-208821, *1998 JANNAF Propulsion Meeting*, Cleveland, OH, 15-17 July 1998.
- [45]Farnell, Casey C., “Multi-Axis Plasma Profiling System for Characterization of Plasma Thruster Plumes,” AIAA 2006-4818, *42<sup>nd</sup> Joint Propulsion Conference & Exhibit*, Sacramento, CA, 9-12 July 2006.
- [46]Temkin, S., “Performance Characterization of A Three-Axis Hall Effect Thruster,” Air Force Institute of Technology, Dayton, OH, Master’s Thesis AFIT/GAE/ENY/10-D02.
- [47]Extorr Inc., “Instruction Manual Extorr XT Series RGE,” New Kensington, PA., Instrument Manual.
- [48]Kurt J. Lesker Company, “300 Series Gauge with Intergrated Controller & Display,” Kurt J. Lesker Company. [online database]. URL: [http://www.lesker.com/newweb/Gauges/convection\\_KJLC\\_3.cfm](http://www.lesker.com/newweb/Gauges/convection_KJLC_3.cfm) [cited 14 Aug 2011].
- [49]Buek Co. Inc., “BHT-600W hall Thruster Operating and Maintenance Manual,” Natick, MA, Instrument Manual.
- [50]Farnell and Williams, “ExB Operating Manual”, Colorado State University, Fort Collins, CO., Instrument Manual.
- [51]Air Force Research Laboratory, “Busek 200W Hall Effect Thruster Lifetest Report”, Edwards AFB, CA 93524.
- [52]Farnell and Williams, “Faraday Probe Operating Manual”, Colorado State University, Fort Collins, CO., Instrument Manual.
- [53]Thermo Scientific, “Thermo Scientific NESLAB ThermoFLex Recirculating Chillers,” Product Specifications. [online database]. URL: [http://www.thermo.com/eThermo/CMA/PDFs/Product/productPDF\\_8824.pdf](http://www.thermo.com/eThermo/CMA/PDFs/Product/productPDF_8824.pdf). [cited 21 Oct 2011].



<b>REPORT DOCUMENTATION PAGE</b>			Form Approved OMB No. 0704-0188		
<p>The public reporting burden for this collection of information is estimated to average 1 hour per response, including the time for reviewing instructions, searching existing data sources, gathering and maintaining the data needed, and completing and reviewing the collection of information. Send comments regarding this burden estimate or any other aspect of this collection of information, including suggestions for reducing this burden to Department of Defense, Washington Headquarters Services, Directorate for Information Operations and Reports (0704-0188), 1215 Jefferson Davis Highway, Suite 1204, Arlington, VA 22202-4302. Respondents should be aware that notwithstanding any other provision of law, no person shall be subject to any penalty for failing to comply with a collection of information if it does not display a currently valid OMB control number. PLEASE DO NOT RETURN YOUR FORM TO THE ABOVE ADDRESS.</p>					
1. REPORT DATE (DD-MM-YYYY) 09-03-2012		2. REPORT TYPE Master's Thesis		3. DATES COVERED (From — To) August 2010 – March 2012	
4. TITLE AND SUBTITLE Plume Characterization of Busek 600W Hall Thruster			5a. CONTRACT NUMBER		
			5b. GRANT NUMBER		
			5c. PROGRAM ELEMENT NUMBER		
6. AUTHOR(S)  Bui, Duc Minh, 2LT, USAF			5d. PROJECT NUMBER		
			5e. TASK NUMBER		
			5f. WORK UNIT NUMBER		
7. PERFORMING ORGANIZATION NAME(S) AND ADDRESS(ES) Air Force Institute of Technology Graduate School of Engineering and Management (AFIT/ENY) 2950 Hobson Way WPAFB OH 45433-7765			8. PERFORMING ORGANIZATION REPORT NUMBER AFIT/GA/ENY/12-M05		
9. SPONSORING / MONITORING AGENCY NAME(S) AND ADDRESS(ES) Air Force Research Laboratory Space and Missile Propulsion Division Att: Mr. Michael Huggins (Michael.Huggins@edwards.af.mil) 1 Ara Rd. Edwards, AFB, CA 93524			10. SPONSOR/MONITOR'S ACRONYM(S) AFRL		
			11. SPONSOR/MONITOR'S REPORT NUMBER(S)		
12. DISTRIBUTION / AVAILABILITY STATEMENT APPROVED FOR PUBLIC RELEASE; DISTRIBUTION UNLIMITED					
13. SUPPLEMENTARY NOTES This material is declared a work of the U.S. Government and is not subject to copyright protection in the United States.					
14. ABSTRACT <p>The BHT-600W thruster has a high potential to place on various commercial and military satellites as a main propulsion system for orbit maintenance and orbit maneuvering. Therefore, the thruster's performance characteristics and parameters were evaluated for various operating conditions. These parameters include thrust, power consumption, mass flow rate, and efficiencies. Various plume properties were measured and characterized for the thruster to include exhaust beam profile and ion species distribution. The faraday probe was used to examine the thruster plume current density while the ion species fractions were determined by the ExB probe. The inverted pendulum thrust stand was also utilized to determine the thrust performance of the thruster. This research determined optimal performance for this thruster was lower but closed to values stated by Busek Co. The measured values were <math>34.8 \pm 1.3</math> mN of thrust, <math>1,267 \pm 39</math>s specific impulse, and had a measured propulsive efficiency of <math>36.2 \pm 2.4</math> %. Last, beam efficiency from Faraday probe measurements yielded <math>52.1 \pm 0.27</math>%. Charge exchanges were observed to appear around <math>40^\circ</math> divergence angles. Higher charge ion species were found to dominate with increasing discharge voltage. Lastly, there were minimal effects of magnet currents on thruster's performance. The results from the research will hopefully be of use in future developments and will contribute to operational applications. This research could potentially be used to improve or confirm numerical models, help to develop future designs, and improve comparison of experimentation with on-orbit plume simulations.</p>					
15. SUBJECT TERMS thrust, specific impulse, efficiency, beam current density, species mass fraction, BHT-600W					
16. SECURITY CLASSIFICATION OF:			17. LIMITATION OF ABSTRACT  UU	18. NUMBER OF PAGES  175	19a. NAME OF RESPONSIBLE PERSON Richard E. Huffman, Jr., LtCol, USAF
a. REPORT  U	b. ABSTRACT  U	c. THIS PAGE  U			19b. TELEPHONE NUMBER (Include Area Code) (575) 678-1251 Email: richard.huffman@holloman.af.mil